Novel Design and Construction Techniques for Sustainable Structures

Lead Guest Editor: Khaled Ghaedi
Guest Editors: Meisam Gordan, Ahad Javanmardi, Mohammed Jameel, and Niaz Bahadur Khan

Novel Design and Construction Techniques for Sustainable Structures

Novel Design and Construction Techniques for Sustainable Structures

Lead Guest Editor: Khaled Ghaedi
Guest Editors: Meisam Gordan, Ahad Javanmardi, Mohammed Jameel, and Niaz Bahadur Khan

Zhaofei Chu, China
Wonseok Chung, Republic of Korea
Donato Ciampa, Italy
Gian Paolo Cimellaro, Italy
Francesco Colangelo, Italy
Romulus Costache, Romania
Liviu-Adrian Cotfas, Romania
Antonio Maria D'Altri, Italy
Bruno Dal Lago, Italy
Amos Darko, Hong Kong
Arka Jyoti Das, India
Dario De Domenico, Italy
Gianmarco De Felice, Italy
Stefano De Miranda, Italy
Maria T. De Risi, Italy
Tayfun Dede, Turkey
Sadik O. Degertekin, Turkey
Camelia Delcea, Romania
Cristoforo Demartino, China
Giuseppe Di Filippo, Italy
Luigi Di Sarno, Italy
Fabio Di Trapani, Italy
Aboelkasim Diab, Egypt
Thi My Dung Do, Vietnam
Giulio Dondi, Italy
Jiangfeng Dong, China
Chao Dou, China
Mario D'Aniello, Italy
Jingtao Du, China
Ahmed Elghazouli, United Kingdom
Francesco Fabbrocino, Italy
Flora Faleschini, Italy
Dingqiang Fan, Hong Kong
Xueping Fan, China
Qian Fang, China
Salar Farahmand-Tabar, Iran
Ilenia Farina, Italy
Roberto Fedele, Italy
Guang-Liang Feng, China
Luigi Fenu, Italy
Tiago Ferreira, Portugal
Marco Filippo Ferrotto, Italy
Antonio Formisano, Italy
Guoyang Fu, Australia
Stefano Galassi, Italy

Junfeng Gao, China
Meng Gao, China
Giovanni Garcea, Italy
Enrique García-Macías, Spain
Emilio García-Taengua, United Kingdom
DongDong Ge, USA
Khaled Ghaedi, Malaysia
Khaled Ghaedi, Malaysia
Gian Felice Giaccu, Italy
Agathoklis Giaralis, United Kingdom
Ravindran Gobinath, India
Rodrigo Gonçalves, Portugal
Peilin Gong, China
Belén González-Fonteboa, Spain
Salvatore Grasso, Italy
Fan Gu, USA
Erhan Güneyisi, Turkey
Esra Mete Güneyisi, Turkey
Pingye Guo, China
Ankit Gupta, India
Federico Gusella, Italy
Kemal Hacıefendioğlu, Turkey
Jianyong Han, China
Song Han, China
Asad Hanif, Macau
Hadi Hasanzadehshooiili, Canada
Mostafa Fahmi Hassanein, Egypt
Amir Ahmad Hedayat, Iran
Khandaker Hossain, Canada
Zahid Hossain, USA
Chao Hou, China
Biao Hu, China
Jiang Hu, China
Xiaodong Hu, China
Lei Huang, China
Cun Hui, China
Bon-Gang Hwang, Singapore
Jijo James, India
Abbas Fadhil Jasim, Iraq
Ahad Javanmardi, China
Krishnan Prabhakan Jaya, India
Dong-Sheng Jeng, Australia
Han-Yong Jeon, Republic of Korea
Pengjiao Jia, China
Shaohua Jiang, China

Chayut Ngamkhanong, Thailand
Trung Ngo, Australia
Tengfei Nian, China
Mehdi Nikoo, Canada
Youjun Ning, China
Olugbenga Timo Oladinrin, United Kingdom
Oladimeji Benedict Olalusi, South Africa
Timothy O. Olawumi, Hong Kong
Alejandro Orfila, Spain
Maurizio Orlando, Italy
Siti Aminah Osman, Malaysia
Walid Oueslati, Tunisia
SUVASH PAUL, Bangladesh
John-Paris Pantouvakis, Greece
Fabrizio Paolacci, Italy
Giuseppina Pappalardo, Italy
Fulvio Parisi, Italy
Dimitrios G. Pavlou, Norway
Daniele Pellegrini, Italy
Gatheeshgar Perampalam, United Kingdom
Daniele Perrone, Italy
Giuseppe Piccardo, Italy
Vagelis Plevris, Qatar
Andrea Pranno, Italy
Adolfo Preciado, Mexico
Chongchong Qi, China
Yu Qian, USA
Ying Qin, China
Giuseppe Quaranta, Italy
Krishanu ROY, New Zealand
Vlastimir Radonjanin, Serbia
Carlo Rainieri, Italy
Rahul V. Ralegaonkar, India
Raizal Saifulnaz Muhammad Rashid, Malaysia
Alessandro Rasulo, Italy
Chonghong Ren, China
Qing-Xin Ren, China
Dimitris Rizos, USA
Geoffrey W. Rodgers, New Zealand
Pier Paolo Rossi, Italy
Nicola Ruggieri, Italy
JUNLONG SHANG, Singapore

Nikhil Saboo, India
Anna Saetta, Italy
Juan Sagaseta, United Kingdom
Timo Saksala, Finland
Mostafa Salari, Canada
Ginevra Salerno, Italy
Evangelos J. Sapountzakis, Greece
Vassilis Sarhosis, United Kingdom
Navaratnarajah Sathiparan, Sri Lanka
Fabrizio Scozzese, Italy
Halil Sezen, USA
Payam Shafigh, Malaysia
M. Shahria Alam, Canada
Yi Shan, China
Hussein Sharaf, Iraq
Mostafa Sharifzadeh, Australia
Sanjay Kumar Shukla, Australia
Amir Si Larbi, France
Okan Sirin, Qatar
Piotr Smarzewski, Poland
Francesca Sollecito, Italy
Rui Song, China
Tian-Yi Song, Australia
Flavio Stochino, Italy
Mayank Sukhija, USA
Piti Sukontasukkul, Thailand
Jianping Sun, Singapore
Xiao Sun, China
T. Tafsirojjaman, Australia
Fujiao Tang, China
Patrick W.C. Tang, Australia
Zhi Cheng Tang, China
Weerachart Tangchirapat, Thailand
Xiaxin Tao, China
Piergiorgio Tataranni, Italy
Elisabete Teixeira, Portugal
Jorge Iván Tobón, Colombia
Jing-Zhong Tong, China
Francesco Trentadue, Italy
Antonello Troncone, Italy
Majbah Uddin, USA
Tariq Umar, United Kingdom
Muahmmad Usman, United Kingdom
Muhammad Usman, Pakistan
Mucteba Uysal, Turkey

Ilaria Venanzi, Italy
Castorina S. Vieira, Portugal
Valeria Vignali, Italy
Claudia Vitone, Italy
Liwei WEN, China
Chunfeng Wan, China
Hua-Ping Wan, China
Roman Wan-Wendner, Austria
Chaohui Wang, China
Hao Wang, USA
Shiming Wang, China
Wayne Yu Wang, United Kingdom
Wen-Da Wang, China
Xing Wang, China
Xiuling Wang, China
Zhenjun Wang, China
Xin-Jiang Wei, China
Tao Wen, China
Weiping Wen, China
Lei Weng, China
Chao Wu, United Kingdom
Jiangyu Wu, China
Wangjie Wu, China
Wenbing Wu, China
Zhixing Xiao, China
Gang Xu, China
Jian Xu, China
Panpan, China
Rongchao Xu, China
HE YONGLIANG, China
Michael Yam, Hong Kong
Hailu Yang, China
Xu-Xu Yang, China
Hui Yao, China
Xinyu Ye, China
Zhoujing Ye , China
Gürol Yildirim, Turkey
Dawei Yin, China
Doo-Yeol Yoo, Republic of Korea
Zhanping You, USA
Afshar A. Yousefi, Iran
Xinbao Yu, USA
Dongdong Yuan, China
Geun Y. Yun, Republic of Korea

Hyun-Do Yun, Republic of Korea
Cemal YİĞİT, Turkey
Paolo Zampieri, Italy
Giulio Zani, Italy
Mariano Angelo Zanini, Italy
Zhixiong Zeng, Hong Kong
Mustafa Zeybek, Turkey
Henglong Zhang, China
Jiupeng Zhang, China
Tingting Zhang, China
Zengping Zhang, China
Zetian Zhang, China
Zhigang Zhang, China
Zhipeng Zhao, Japan
Jun Zhao, China
Annan Zhou, Australia
Jia-wen Zhou, China
Hai-Tao Zhu, China
Peng Zhu, China
QuanJie Zhu, China
Wenjun Zhu, China
Marco Zucca, Italy
Haoran Zuo, Australia
Junqing Zuo, China
Robert Černý, Czech Republic
Süleyman İpek, Turkey

Contents

Research Article

Numerical Simulation Research and Application of Support Design of Broken Rock Mass in Submarine Gold Mine

Yu-yun Fan [ID],[1,2] **Ming-wei Jiang,**[1,2] **Li Cheng** [ID],[1,2] **Xi Wang,**[1,2] **Xing-quan Liu,**[1,2] **Chunlong Wang,**[1,2] **and Kexu Chen**[1,2]

[1]*Deep Mining Laboratory of Shandong Gold Group Co., Ltd., Laizhou 261442, China*
[2]*Shandong Key Laboratory of Deep-sea and Deep-earth Metallic Mineral Intelligent Mining, Laizhou 261442, China*

Correspondence should be addressed to Yu-yun Fan; 1066978589@qq.com

In order to solve the problem that the broken rock mass is easy to collapse and fall during the excavation of a submarine gold mine, two kinds of bolt-mesh-concreting combined support schemes are designed by means of field engineering geological investigation, indoor rock mechanics test, rock mass quality classification, and theoretical analysis. We use the numerical simulation for verification and carry out the field industrial test. The results show that the stability grade of broken surrounding rock is III–IV; both schemes can effectively control the deformation and failure of surrounding rock. Compared with the unsupported scheme, the maximum roof displacement in the scheme using roadway roof and sidewall support is reduced by 26.9%, the maximum thickness of the roof plastic zone is reduced by 58.2%, and the volume of the surrounding rock plastic zone is reduced by 26.32%. The bolt-mesh-shotcrete support has good control effect on the loose deformation of surrounding rock, which can effectively prevent the roof collapse and sidewall spalling of roadway. The field industrial test of support scheme meets the stability control requirements of broken rock mass in mines, and the application effect is obvious. The research results presented in this study provide valuable technical guidance and essential insights for the design of support systems in other similar mining projects, contributing to the effective control and stability of broken rock masses during excavation.

1. Introduction

Rock mass stability is the core issue of underground engineering design. The stability of underground rock after excavation plays an important role in mine safety production, especially roof caving and collapse after excavation, which has always been the most concerning problem in mine safety production. The stability of rock mass after excavation is a difficult problem in the study of mine ground pressure management. Roof caving and collapse accidents are closely related to mining environment, geological factors, mining methods, and roof support control methods [1–3]. Aiming at the stability control problem of broken rock mass, scholars at home and abroad have done much research and exploration. Sheng et al. [4] analyzed and studied the roadway with strong plastic broken rock mass and formed a coupling support method combining prestressed anchor, steel wire mesh, shotcrete, grouting, and pressure relief groove. Zhang et al. [5] analyzed the roadway

support under the condition of an empty area around the seabed roadway and proposed the integrated support technology of shotcrete-bolting and piercing. Tian [6] proposed the deep-shallow rigid-flexible coupling bolt-grouting support technology for high-stress roadways in view of the large deformation of surrounding rock and the serious failure of support structure in deep high-stress roadway; Zuo et al. [7] proposed the graded control principle and yield failure criterion of surrounding rock gradient support and realized the graded three-dimensional pressure shell control of surrounding rock based on gradient failure mechanism. Meng et al. [8] revealed the deformation and failure characteristics of deep high-stress broken soft rock roadway and put forward the step-by-step combined support technology scheme of "anchor net cable shotcrete + U steel support + grouting + floor anchor grouting." Zhang et al. [9] used the numerical simulation to study the stress and displacement variation law of roadway under different surrounding rocks, aiming to determine the

FIGURE 1: Existing supporting methods of broken rock mass.

reasonable roadway support method. Hui and Li [10] provided the calculation formula of the permanent support scope when the mine roadway passed through the loose and broken zone. At present, the research on the stability control technology of fractured rock mass in submarine gold mines is still insufficient [11–16]. However, there have been many important advances in rock mechanics and support engineering in the past 5 years, such as the techniques and strategies proposed in the study of rock stability [17–21]. In addition to static loads, dynamic factors are also important factors affecting rock stability, such as microseisms caused by fault slippage or ground vibrations caused by blasting [22–25].

This paper uses a broken rock mass in the southwest wing of a seabed metal mine as the research background. Through field engineering geological survey, laboratory rock mechanics test, rock mass quality classification, theoretical analysis, and other means and methods, the corresponding high-stress coupling support scheme is designed, the numerical simulation is used to verify, and the field industrial test is carried out. The aim is to ensure the stability of the roadway surrounding rock support and enhance the efficiency of roadway excavation. This research provides valuable technical support for the excavation and stability control of roadways in broken-rock conditions. Additionally, it aims to reduce support costs and improve the safety of mining operations.

2. Engineering Background

The structure controls the ore body of a submarine gold deposit before and during mineralization. The mineralization intensity is closely related to the fragmentation degree of altered rock and the development degree of metallogenic fracture. The high-grade part and the thickness of the ore body are mostly the areas with developed metallogenic fracture and strong rock fragmentation. The ore body is distributed in the pyrite sericitization catacaustic rock belt with strongly altered rock fragmentation and developed metallogenic fracture under the main fracture surface. Some areas are affected by seawater pressure and internal seepage of rock mass, and the rock strata movement law is complex [5], which is more likely to cause the caving and collapse of the roof fracture area. The transportation roadway outside the southwest wing vein is located in the area of the broken rock

mass. The joint fissure is developed, the rock mass strength is low, and the joint is filled with alteration. The alteration is affected by water (after water, it expands and produces slippery). The fracture expansion is low and easy to collapse. If the support is not timely or the support scheme is unreasonable, it may cause the collapse to further extend upward and gradually approach or even lead to the seabed strata, resulting in large area of seawater recharge [10]. Therefore, timely and effective support measures to control roadway surrounding rock and maintain long-term stability are the key problems to be solved urgently.

At present, in view of the broken ore body, the excavation method of the mine mainly adopts the collision wedge method and the pipe shed method. The steel arch, shotcrete, metal mesh, and other combined support methods are used (Figure 1). The support cost is relatively high, the excavation speed is slow, and the excavation speed of the mine is seriously restricted.

3. Rock Mass Quality Evaluation and Rock Mechanics Parameter Estimation of the Surrounding Rock

3.1. Indoor Rock Mechanic Test. In order to accurately obtain the basic rock mechanical parameters of the rock mass in the transportation roadway area of the southwest wing, typical rock samples were collected from the transportation roadway and the heading face of the mining connection. The roof positions of the working face of the transportation roadway in the southwest wing of -212, -307, and -373 m sections were sampled, respectively. We mainly selected intact rocks with fewer original joints and fissures. Three rock samples were taken at each level, and a total of nine rock samples were obtained.

The rock samples are processed into standard rock specimens. We carried out the uniaxial compression, Brazilian splitting, and triaxial compression tests by using ZTR-276 rock triaxial testing machine and rock mechanics universal testing machine (Figure 2). The basic rock mechanics parameters are obtained, as shown in Table 1.

3.2. Quality Evaluation of Surrounding Rock Mass. Through the field engineering geological survey, the structural plane information of roadway surrounding rock is measured, counted, and

(a)

(b)

FIGURE 2: Laboratory rock mechanics test instrument: (a) ZTR-276 rock triaxial testing machine and (b) rock mechanics universal testing machine.

TABLE 1: Rock physical and mechanical parameters of indoor rock mechanic test.

Specimen position	Density (kg/m^3)	Uniaxial compressive strength (MPa)	Tensile strength (MPa)	Elastic modulus (GPa)	Poisson's ratio	Intensive parameter	
						c/MPa	φ
−212 m level	2,718	39.18	5.3	33.85	0.235	8.48	40.4
−307 m level	2,722	45.52	4.9	38.75	0.23	15.63	41.4
−373 m level	2,748	78.15	5.9	44.90	0.22	10.62	50.8

TABLE 2: Comparison of classification results of three rock mass evaluation methods.

Position	RMR			Q		GSI
	Grade	Description	Stability	Grade	Description	GSI value
−200 m	IV	Bad	(2.5 m span) 10 hr	IV	Very bad	39 (36–42)
−240 m	IV	Bad	(2.5 m span) 10 hr	IV	Very bad	39 (36–42)
−280 m	IV	Bad	(2.5 m span) 10 hr	IV	Very bad	44 (45–53)
−320 m	IV	Bad	(2.5 m span) 10 hr	IV	Very bad	47 (45–53)
−360 m	III	Not very bad	(5 m span) 7 days	III	Bad	56 (50–70)
−400 m	III	Not very bad	(5 m span) 7 days	III	Bad	56 (50–70)
−440 m	III	Not very bad	(5 m span) 7 days	III	Bad	63 (50–70)

analyzed by using the line measurement method and statistical window method, and the distribution characteristics of joints and fissures in different levels of the surrounding rock are mastered. According to the survey results, we use the Rock Mass Rating (RMR), Q-system (Q), and Geological Strength Index (GSI) classification methods to classify the stability of the roadway broken surrounding rock at −200 to −440 m in the southwest wing. The results are shown in Table 2. At southwest wing roadway surrounding rock quality grade III–IV, rock stability is very poor; the joint fissures of surrounding rock are very developed, and its stability is mainly controlled by joint fissures.

3.3. Estimation of Mechanical Parameters of Rock Mass. According to the indoor rock mechanics test and rock mass quality evaluation results, the reduction method based on rock mass quality evaluation and the systematic Hoek–Brown criterion estimation method are used to estimate the rock mass mechanical parameters. The average value of the

calculated values of the two methods is taken as the final rock mass parameters.

When using the reduction method based on rock mass quality evaluation to estimate rock mass mechanical parameters, it is necessary to first collect mechanical test data related to rock mass samples, reduce the data, calculate the minimum principal stress, use a rock classification system to estimate rock mass strength parameters, and finally conduct sensitivity analysis to understand the reliability of the estimation results. The Hoek–Brown criterion estimation method requires first determining the rock mass properties and then using the empirical formula of the Hoek–Brown criterion to calculate the rock mass parameters based on the characteristics of the rock sample.

Due to the limited field sampling, the rock sample parameters are used to represent the rock parameters of the nearby level: the rock samples of −212 m level represent the rock properties of −200 and −240 m middle sections;

TABLE 3: Estimation results of physical and mechanical parameters of fractured rock mass in the southwest wing.

Position	Density (t/m^3)	Uniaxial compressive strength (MPa)	Tensile stress (MPa)	Elastic modulus (GPa)	Poisson's ratio	Intensive parameter	
						c/MPa	φ/(°)
−200 m	2.718	9.58	0.08	5.5	0.235	2.90	35.7
−240 m		8.87	0.07	5.3		2.83	35.1
−280 m	2.722	8.68	0.18	4.4	0.230	3.45	36.3
−320 m		8.55	0.27	4.5		3.49	36.6
−360 m		16.24	1.99	10.4		6.95	39.3
−400 m	2.748	17.74	2.11	11.8	0.220	7.06	39.8
−440 m		18.86	5.54	13.4		7.40	40.6

rock samples at the −307 m level represent rock properties at −280 and −320 m intervals; and rock samples of −373 m level represent rock properties of −360, −400, and −440 m middle sections. The estimation results of rock mechanics parameters are shown in Table 3.

4. Support Scheme Design and Numerical Simulation Analysis

4.1. Support Scheme Design. Based on the field engineering geological investigation, support method investigation, and rock mass quality evaluation results and according to the relevant theoretical calculation, design specification, and engineering analogy method, the bolt-mesh-shotcrete combined support is selected, and two support schemes are designed to ensure the stability and safety of the roadway.

Scheme A: Bolt-mesh-shotcrete combined support, roadway roof and sidewall are using Φ 20 × 2,200 mm resin bolt support, the row spacing is 1,000 × 1,000 mm, metal mesh specification is Φ 4 @ 50 × 50 mm, concrete spray layer thickness is 50 mm, and a total of nine bolts per row.

Scheme B: Bolting and shotcrete support, only supporting roadway roof, roadway two sides do not support; the parameters of bolt, double ribs, and shotcrete are the same as that of support scheme A, with five bolts per row.

4.2. Numerical Model and Boundary Conditions. We use FLAC3D to simulate the support scheme. FLAC3D is a numerical simulation method based on the finite difference method used to solve mechanical problems in geotechnical and geological engineering. Based on the principle of combining particle fluid mechanics with the finite element method, the problem area is discretized and meshed. FLAC3D can simulate the deformation and fracture behavior of rock and soil, and obtain relevant parameters such as stress and strain at each node for analyzing the stability of the structure.

Because two adjacent roadways are close to each other in the buried depth (the thickness of isolated rock mass is about 10 m), considering the influence of adjacent roadway excavation on the stability of surrounding rock, two segment transport roadways in the middle (40 m) are selected as the simulation objects. The calculation area of the model is 30 × 10 × 40 m (length × width × height), and the excavation section of the roadway is 3.6 × 3.3 m. There are 106,785 nodes

and 100,320 units. The model adopts the ideal elastic–plastic rock mass, and the plain concrete support with an appropriate increase in mechanical parameters represents the metal mesh shotcrete support. In the numerical calculation, shell element is used to simulate shotcrete and pile element is used to simulate bolt support. The vertical displacement constraint is applied at the bottom of the model, and the horizontal displacement constraint is applied at the vertical boundary before and after the model. Figure 3 shows the overall and support model for numerical calculations.

We select the −360 m level with the worst surrounding rock condition in the southwest wing of the mine for the support scheme simulation. The simulation schemes are no support, scheme A and scheme B, respectively. The value of ground stress is referred to the measured ground stress value of the mine, as shown in Table 4. The numerical simulation parameters refer to the estimated values of rock mechanics parameters in Table 3, as shown in Table 5.

4.3. Numerical Simulation Results and Analysis. Figures 4 and 5 show that the surrounding rock of the roadway is mainly in compressive stress state, and there is a small tensile stress in some rock walls. The stress concentration of surrounding rock is mainly at the two corners of arch shoulder and floor, and the stress concentration in the vertical direction is much more obvious than that in the horizontal order. Compared with before support, the maximum value of surrounding rock compressive stress changes little after support, but the stress concentration position moves to the free face of roadway, and the stress value at the roof increases, indicating that bolt-mesh-shotcrete support effectively prevents the deformation and loosening of surrounding rock, resulting in the increase of shallow compressive stress of surrounding rock.

We can see from Figures 6–8 that the convergence deformation of surrounding rock after support is also reduced compared with that without support, and the range of the plastic zone is also degenerated, especially the thickness of the roadway roof plastic zone is significantly reduced. The deformation displacement of the roof is reduced from 12.73 to 9.31 mm, and the convergence of the sidewall is reduced from 13.13 to 11.28 mm (see Table 6). It shows that the bolt-mesh-shotcrete support has a good control effect on the loose deformation of the surrounding rock, which can effectively
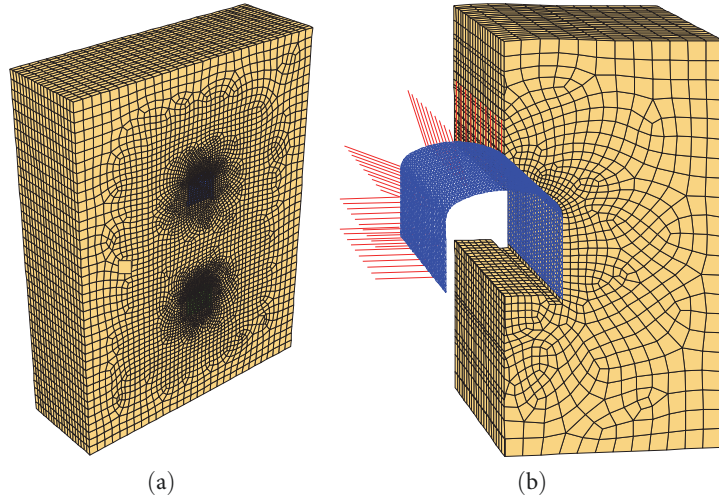
FIGURE 3: Numerical models: (a) overall model and (b) support model.

TABLE 4: The value of −360 m level ground stress.

Position	Maximum horizontal principal stress σ hmax (MPa)	Vertical stresses σz (MPa)	Minimum horizontal principal stress σ hmin (MPa)
−360 m level	19.514	11.42	6.646

TABLE 5: Value of main parameters in numerical simulation.

Material categories	Density (t/m³)	Elastic modulus (GPa)	Poisson's ratio	Tensile stress (MPa)	Cohesion (MPa)	Internal friction angle (°)
−360 m rock	2.748	10.4	0.220	1.99	6.95	39.3
Bolt	7.85	200	0.28	390		
Metal mesh-sprayed concrete	2.50	40	0.25	2.70		
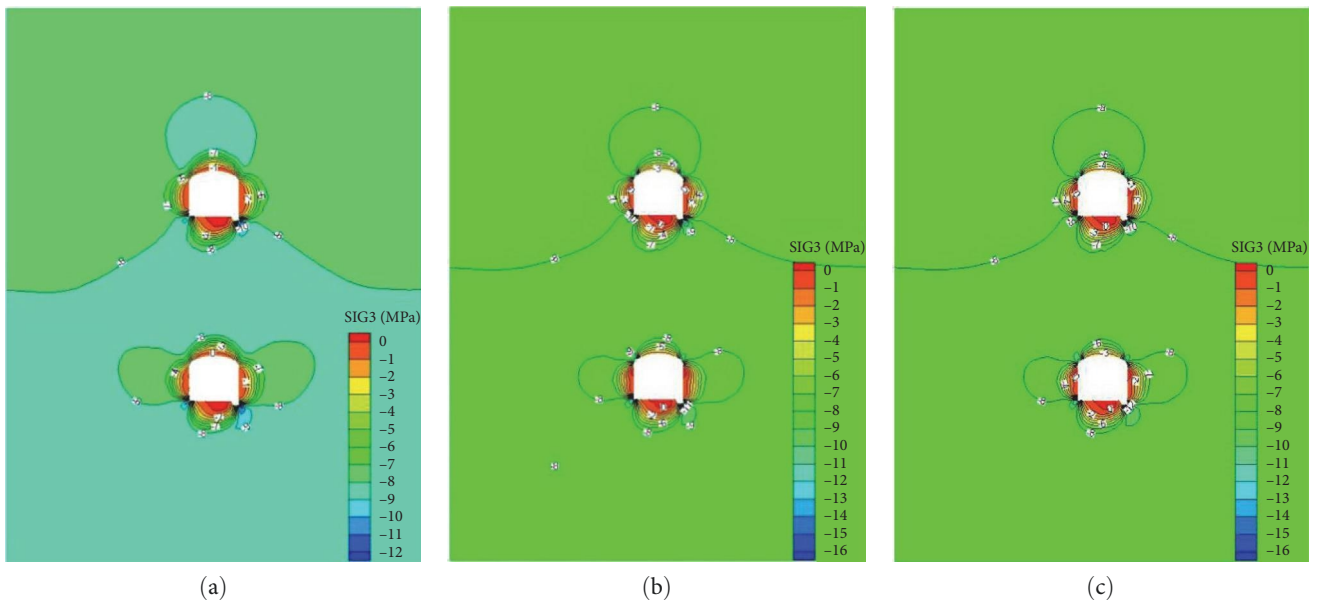
FIGURE 4: The maximum principal stress nephogram of surrounding rock under different support conditions at −360 m level: (a) unsupported, (b) scheme A (nine bolts per row), and (c) scheme B (five bolts per row).
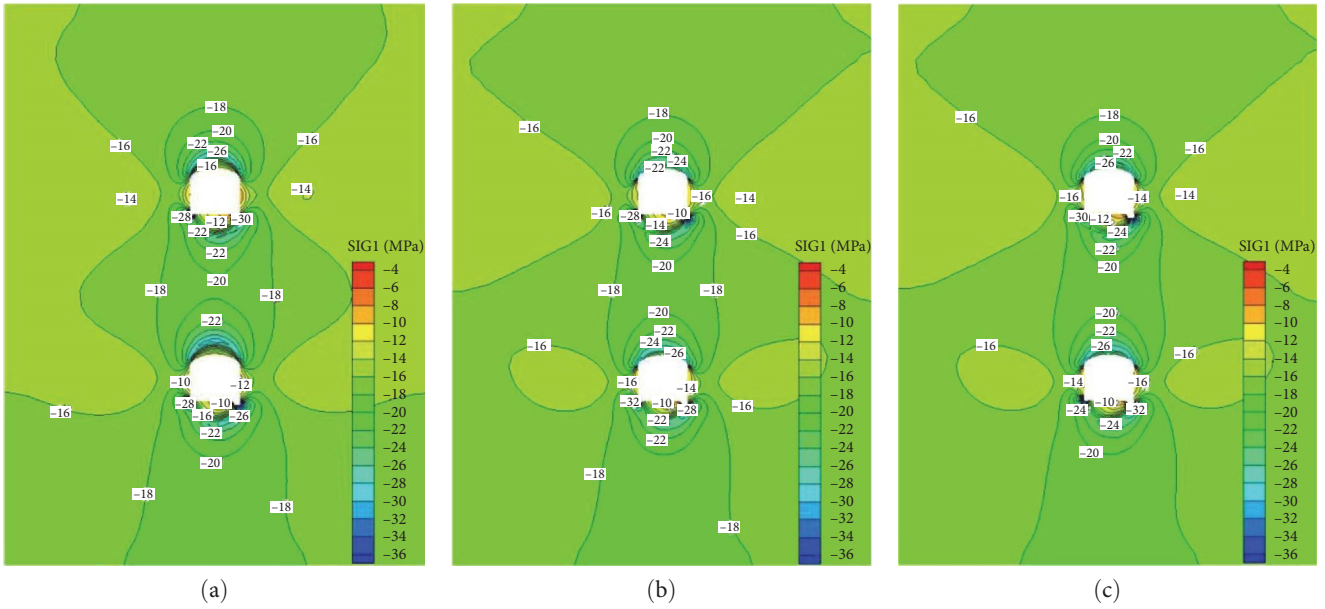
FIGURE 5: The minimum principal stress nephogram of surrounding rock under different support conditions at −360 m level: (a) unsupported, (b) scheme A (nine bolts per row), and (c) scheme B (five bolts per row).
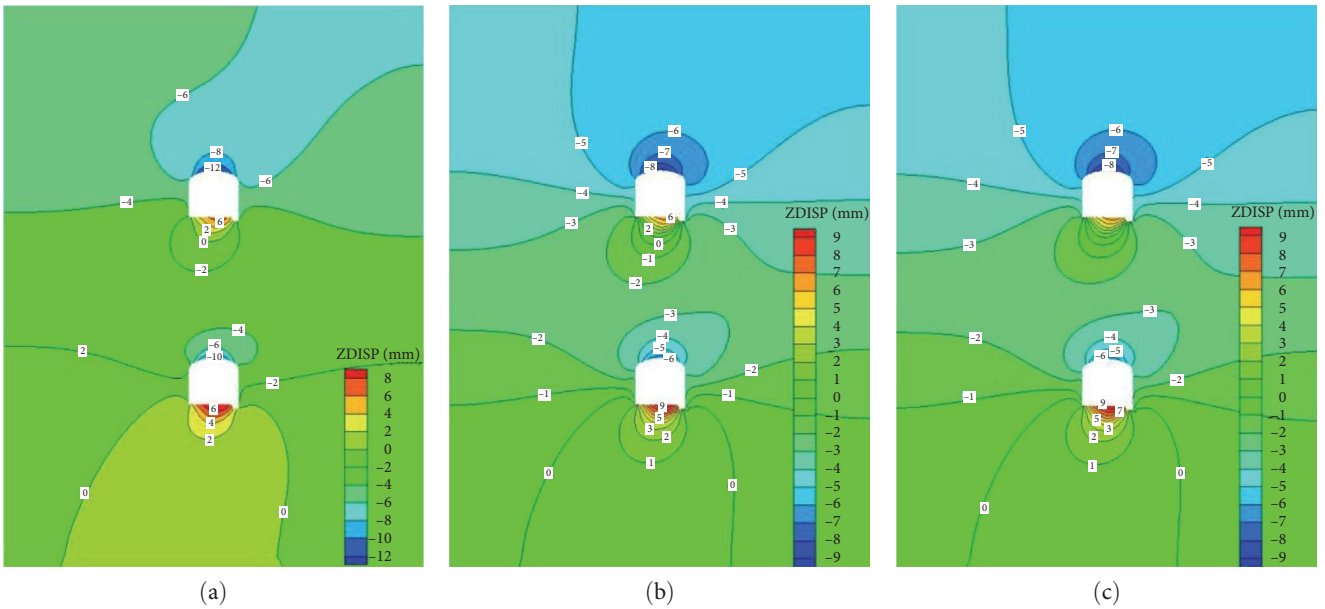
FIGURE 6: Vertical displacement of surrounding rock under different support conditions at −360 m level: (a) unsupported, (b) scheme A (nine bolts per row), and (c) scheme B (five bolts per row).

prevent the roof collapse and sidewall spalling of the roadway. Scheme B only supports the roof of the roadway, and the deformation control of the two sides of the roadway is not as obvious as scheme A. The convergence of the sidewall is reduced from 13.13 to 11.34 mm. The maximum lateral displacement of the two support schemes decreases by 14.1% (scheme A) and 13.6% (scheme B), respectively. There is no significant difference between the two schemes, and the support cost of scheme B is lower than that of scheme A. Therefore, when the surrounding rock of roadway only needs roof

support or two sides of rock mass conditions are good, support scheme B should be preferred.

We can see from the above table that bolt-mesh-shotcrete support effectively controls the loose deformation of roadway surrounding rock and strengthens the overall strength of rock mass. With the increase of support strength, the principal stress of rock mass increases gradually, and the convergence displacement of surrounding rock decreases gradually, especially the maximum displacement of roof decreases by 26.9% (scheme A). When the roadway is not
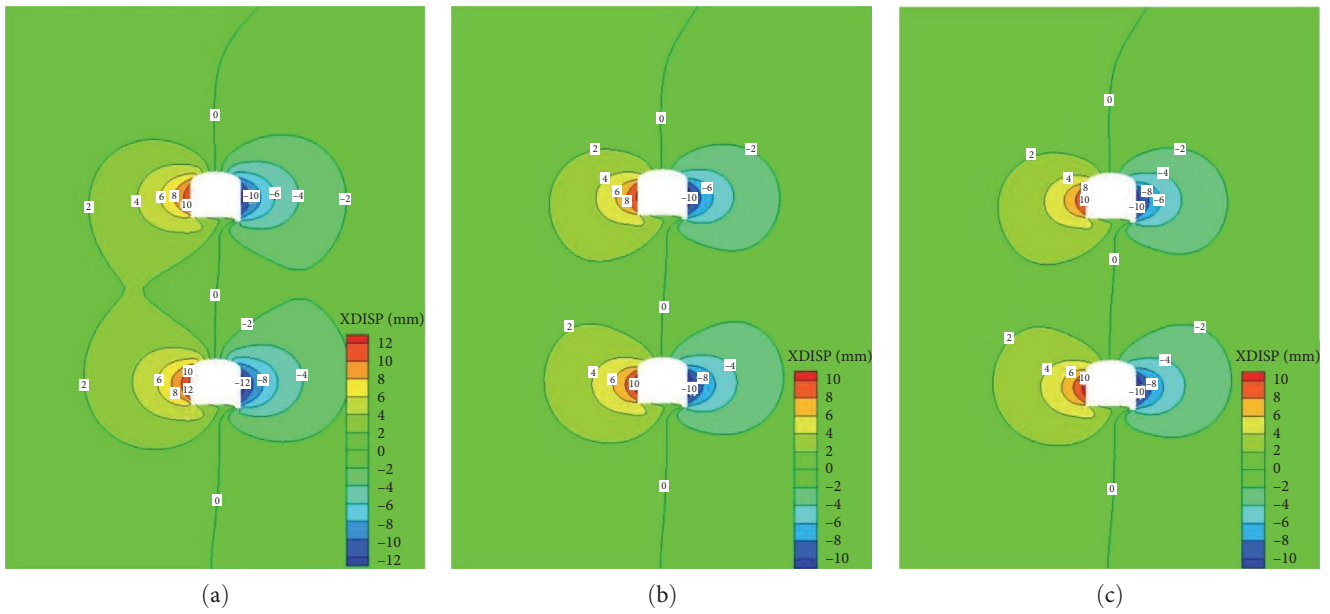
FIGURE 7: Horizontal displacement of surrounding rock under different support conditions of −360 m level: (a) unsupported, (b) scheme A (nine bolts per row), and (c) scheme B (five bolts per row).
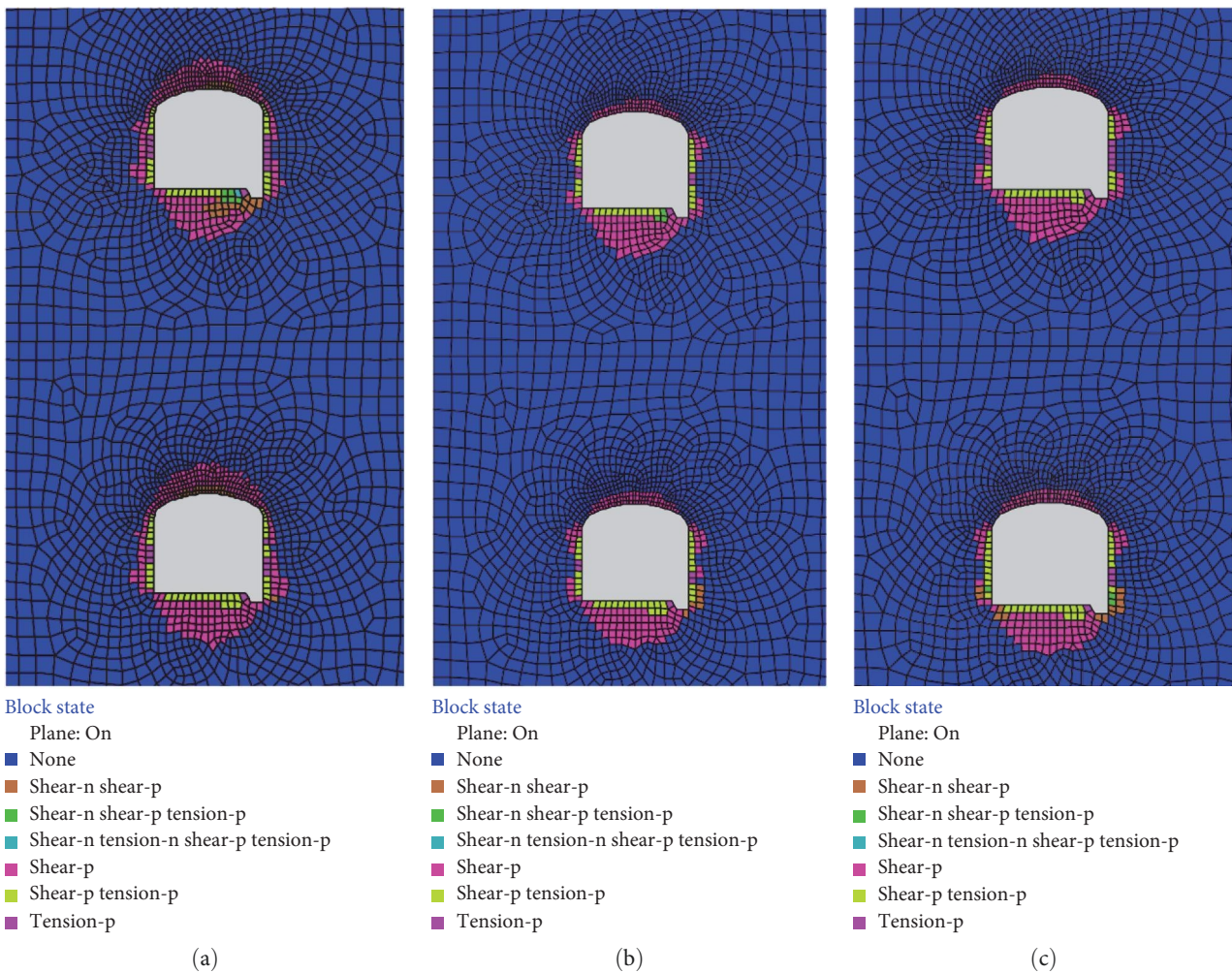
FIGURE 8: Cloud image of the plastic zone of surrounding rock under different supporting conditions at −360 m level: (a) unsupported, (b) scheme A (nine bolts per row), and (c) scheme B (five bolts per row).

TABLE 6: Comparison table of simulation results of surrounding rock under different supporting conditions.

Position	Support scheme	Minimum principal stress (MPa)	Maximum principal stress (MPa)	Maximum roof displacement (mm)	Maximum lateral wall displacement (mm)	Maximum thickness of roof plastic zone (m)	Plastic zone volume of the surrounding rock (m³)
	Unsupported	−33.89	0.48	12.73	13.13	1.03	253.30
−360 m	Scheme A	−33.50	0.89	9.31	11.28	0.43	186.63
	Scheme B	−33.48	0.94	9.37	11.34	0.50	191.81
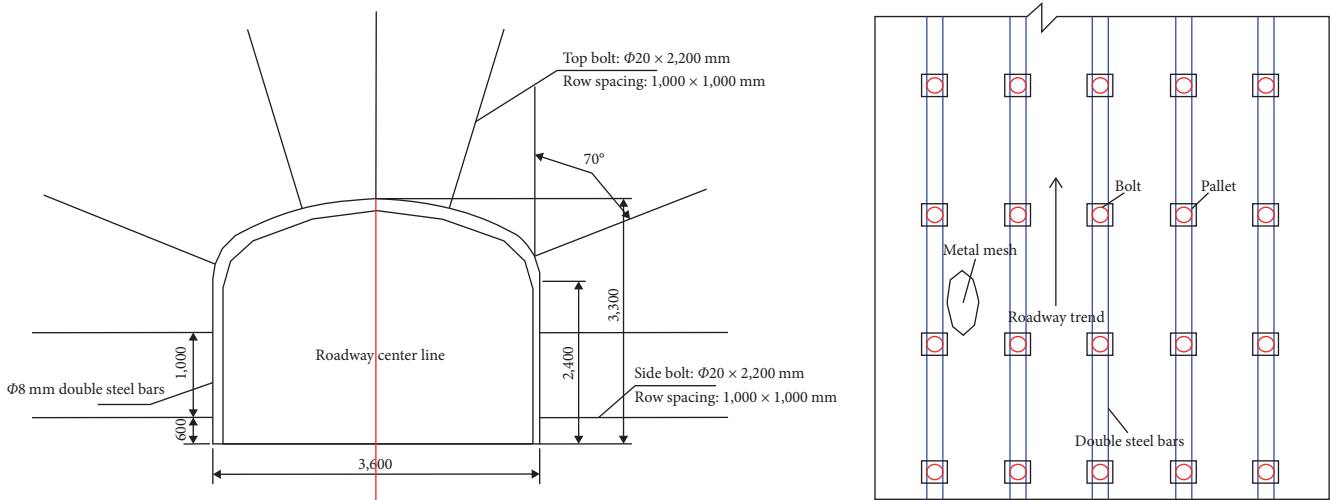
FIGURE 9: −212 m horizontal test roadway anchor net spray support design.

supported, the maximum thickness of the roof plastic zone is 1.03 < 2.20 m and the bolt length meets the safety standard. After support, the maximum thickness of plastic zone of roof is reduced by 58.2%, and the volume of plastic zone of surrounding rock is reduced by 26.32% (scheme A), and the reinforcement effect is remarkable.

5. Site Industrial Test

5.1. Design of Test Area and Support Parameters. According to the field engineering geological investigation and statistical analysis of the broken area, combined with the rock mass quality evaluation at the test site and its nearby area, the combined support method of bolt + metal mesh + shotcrete was determined to strengthen the surrounding rock of roadway at the test site at the level of −212 m. Parameters of bolt-mesh-shotcrete combined support: Φ 20 × 2,200 mm resin bolt is selected for roadway roof and sidewall, and the distance between them is 1,000 × 1,000 mm. After installing the bolt, the metal mesh is mounted along the arch ring, and the double bars are installed along the direction of the roadway. Finally, the 50 mm thick concrete closed support structure and surrounding rock are sprayed (as shown in Figure 9).

5.2. Test Result Analysis. In order to highlight the effectiveness and economy of bolt-mesh-shotcrete combined support, the field test effect at −212 m level was compared with that of U-shaped steel arch support at −228 m level.

As shown in Figures 10 and 11, it can be seen that compared with U-shaped steel arch support, bolt-mesh-shotcrete combined support can not only ensure the lasting stability of broken surrounding rock of roadway, but also has better support effect and can better meet the special requirements of roadway excavation and maintenance in broken rock mass.

Compared with the construction cost (Table 7) of the two supporting methods, anchor mesh shotcrete support also shows great economic advantages.

6. Conclusions

(1) The rock mass stability grade of the broken surrounding rock in the southwest wing has been determined as III–IV using various rock mass quality classification methods (RMR, Q, and GSI). The evaluation of rock mass mechanical parameters using the reduction method of rock mass quality evaluation and the systematic Hoek–Brown criterion estimation method provides essential data for subsequent numerical simulation analysis of support schemes.

(2) Two bolt-mesh-shotcrete combined support schemes, A and B, were designed based on support methods investigation and rock mass quality evaluation. Numerical simulations indicate that this support system effectively controls deformation and enhances overall rock mass strength. As support strength increases, principal stress

FIGURE 10: −212 m horizontal test roadway anchor net spray support effect.

FIGURE 11: −228 m horizontal U-shaped steel arch support effect.

TABLE 7: Comparison table under different supporting conditions.

Supporting position	Support way	U-shaped steel (bolt) row number	Support length (m)	Total support costs (yuan) (including labor costs)	Support unit price (yuan/m) (including labor costs)	Construction personnel
−212 m level	Bolt-mesh-spurting supporting	9	7	5,640.5	805.79	Drilling and bolt installation 2; net 3
−228 m level	U-shaped steel support	8	8.6	15,338.2	1,783.5	10

gradually rises, and convergence displacement decreases. Scheme B is recommended for grade III rock mass when roof support is necessary, while scheme A is favored for grade IV rock mass if the sidewall condition is better but the roof is unstable. The numerical simulations demonstrate the reliability and effectiveness of the anchor mesh shotcrete support scheme.

(3) Field industrial tests confirm that the designed bolting-mesh-spraying support scheme effectively stabilizes fractured rock mass, give full play to self-stability of surrounding rock, and exhibits remarkable support performance. Compared to adjacent horizontal roadway support methods, anchor net shotcrete support demonstrates advantages such as lower cost, simplicity, rapid construction, and improved economics. This scheme can serve as technical guidance for similar mining areas.

Data Availability

Data supporting this research article are available from the corresponding author on reasonable request.

Conflicts of Interest

The authors declare that they have no conflicts of interest.

Acknowledgments

References

[1] X. X. Chen and J. P. Wu, "Study on the mechanism and control technology of large deformation of roadway surounding rock in the fault fracture zone," *Journal of Mining & Safety Engineering*, vol. 35, no. 5, pp. 885–892, 2018.

[2] Z. Jin-feng and Z. Peng-hao, "Analytical model of fully grouted bolts in pull-out tests and in situ rock masses," *International Journal of Rock Mechanics and Mining Sciences*, vol. 113, pp. 278–294, 2019.

[3] Q. Wang, B. Jiang, R. Pan et al., "Failure mechanism of surrounding rock with high stress and confined concrete support system," *International Journal of Rock Mechanics and Mining Sciences*, vol. 102, pp. 89–100, 2018.

[4] J. Sheng, Q. Li, H. Zhang, D. Liu, and G. Zhao, "Study and application of coupling support technology for the roadway with broken and strong-plasticity rock mass," *Mining Research and Development*, vol. 40, no. 8, pp. 91–96, 2020.

[5] C. Zhang, W. Song, J. Fu, Y. Li, and K. Zhang, "Technology for roadway management of fractured rock masses in a submarine gold mine," *Journal of Mining and Strata Control Engineering*, vol. 2, no. 3, Article ID 033039, 2020.

[6] W. Tian, "Research on deep - shallow rigid - flexible coupling anchor - grouting support technology for deep high stress roadway," *Coal Technology*, vol. 41, no. 3, pp. 18–21, 2022.

[7] J. Zuo, Z. Hong, M. Yu, H. Liu, and Z. Wang, "Gradient support model and classification control of broken surrounding rock," *Journal of China University of Mining and Technology*, vol. 51, no. 2, pp. 221–231, 2022.

[8] Q. Meng, L. Han, J. Zhang, S. Wen, F. Zhang, and H. Li, "Research and application of supporting technology in deep hing stress fractured soft-rock roadway," *Joumal of Central South University (Nature Science Edition)*, vol. 47, no. 11, pp. 3861–3872, 2016.

[9] F. Zhang, H. Zhang, Z. Xia, and S. Wang, "Research on surrounding rock support and control technology for submarine deep well tunnel," *Modern Mining*, vol. 39, no. 4, pp. 171–174, 2023.

[10] A. Hui and M. Li, "Engineering geological environment reconstruction and tunnel construction technology in caving rock mass," *Well Construction Technology*, vol. 42, no. 1, pp. 20–24, 2021.

[11] H. Tian, W. Chen, X. Tan, H. Wang, and T. Tian, "Study on reasonable supporting scheme of high ground stress soft rock tunnel," *Rock Mechanics and Engineering*, vol. 30, no. 11, pp. 2285–2292, 2011.

[12] W. Qi, Q. Zhu, X. Zhao, and W. Li, "Numerical simulation study on stability control of fractured rock mass in southwest wing of Xinli mining area of Sanshandao Gold Mine," *Nonferrous Metals (mining part)*, vol. 71, no. 4, pp. 88–94, 2019.

[13] J. Dong, X. Feng, X. Zhang, and Z. Zhang, "Stability evaluation and parameter optimization of fractured rock mass in underground stope," *Journal of Northeastern University (Natural Science Edition)*, vol. 34, no. 9, pp. 1322–1326, 2013.

[14] R. Pan, "Research on bolting and grouting mechanism and control technology of broken surrounding rock in deep roadway," *Journal of Rock Mechanics and Engineering*, vol. 40, no. 4, Article ID 864, 2021.

[15] H. Luo, R. Wu, Q. Wang, and P. Zhang, "Numerical simulation of stress evolution and surrounding rock control technology in deep broken roadway," *Mining Research and Development*, vol. 41, no. 2, pp. 39–44, 2021.

[16] D. Wu, Y. Li, Y. Qian, C. Fan, and E. Dong, "Study on surrounding rock control technology of deep broken rock roadway," *Metal Mine*, vol. 08, pp. 1–7, 2020.

[17] S. Liu, X. Li, D. Wang, and D. Zhang, "Investigations on the mechanism of the microstructural evolution of different coal ranks under liquid nitrogen cold soaking," *Energy Sources, Part A: Recovery, Utilization, and Environmental Effects*, pp. 1–17, 2020.

[18] X. Zhou, S. Wang, X. Li et al., "Research on theory and technology of floor heave control in semicoal rock roadway: taking Longhu coal mine in Qitaihe mining area as an example," *Lithosphere*, vol. 2022, no. Special 11, Article ID 3810988, 2022.

[19] S. Wang, X. Li, and Q. Qin, "Study on surrounding rock control and support stability of ultra-large height mining face," *Energies*, vol. 15, no. 18, Article ID 6811, 2022.

[20] X. Li, S. Chen, S. Wang, M. Zhao, and H. Liu, "Study on in situ stress distribution law of the deep mine: taking Linyi mining area as an example," *Advances in Materials Science and Engineering*, vol. 2021, p. 11, Article ID 5594181, 2021.

[21] H. Liu, B. Zhang, X. Li et al., "Research on roof damage mechanism and control technology of gob-side entry retaining under close distance gob," *Engineering Failure Analysis*, vol. 138, Article ID 106331, 2022.

[22] J. Ma, L. Dong, G. Zhao, and X. Li, "Discrimination of seismic sources in an underground mine using full waveform inversion," *International Journal of Rock Mechanics and Mining Sciences*, vol. 106, pp. 213–222, 2018.

[23] J. Ma, L. Dong, G. Zhao, and X. Li, "Ground motions induced by mining seismic events with different focal mechanisms," *International Journal of Rock Mechanics and Mining Sciences*, vol. 116, pp. 99–110, 2019.

[24] J. Ma, L. Dong, G. Zhao, and X. Li, "Qualitative method and case study for ground vibration of tunnels induced by fault-slip in underground mine," *Rock Mechanics and Rock Engineering*, vol. 52, pp. 1887–1901, 2019.

[25] J. Ma, L. Dong, G. Zhao, and X. Li, "Focal mechanism of mining-induced seismicity in fault zones: a case study of Yongshaba mine in China," *Rock Mechanics and Rock Engineering*, vol. 52, pp. 3341–3352, 2019.

Research Article

Effect of Wrapping on Post-Tensioned Beams Strengthened with Natural Sisal and Jute FRP Using Finite Element Analysis

D. P. Archana [ID],[1] H. N. Jagannatha Reddy,[1] R. Prabhakar,[2] M. U. Aswath,[1] and Basavaraju Paruti [ID][3]

[1]*Department of Civil Engineering, Bangalore Institute of Technology, Bengaluru 560 004, Karnataka, India*
[2]*Structural Engineering, VTU, Belagavi 590 018, Karnataka, India*
[3]*Department of Hydraulics and Water Resource Engineering, HHIOT Campus, Ambo University, Ambo, Ethiopia*

Correspondence should be addressed to D. P. Archana; archana3190@gmail.com and Basavaraju Paruti; basavaraj.paruti@ambou.edu.et

Existing buildings are retrofitted to formulate them to be more resistant to seismic activity, earth motion, and other natural disasters. Many available reinforced concrete buildings across the globe are in desperate need of rehabilitation, repair, or replacement owing to degradation caused by a variety of reasons such as corrosion, lack of detailing, and failure of beam-column bonding, among others. In the construction sector, fibre reinforced polymer (FRP) composites have been recognized as a potential option for repairing and increasing the strength of existing structures. In this study, comparisons are done in terms of load bearing capability of the beams for configurations between FE model predictions and field data (experimental). To assess the FRP retrofit, structural responses for strengthened and control post tensioned concrete (PTC) beams are compared, with strengthening using various wrapping methods. The load bearing capacities of the beams retrofitted with sisal and jute fibre employing strip and full wrapping procedures around all four sides is increased by 35.55 percent and 42.85 percent for sisal FRP and 7.14 percent and 12.01 percent for jute FRP, respectively, as compared to the control specimen. The FRP retrofit model is expected to result in a considerable increase in structural performance.

1. Introduction and Background

Some structures have degraded as a result of a variety of issues ranging from corrosion to fatigue of reinforced concrete elements and are commonly found to be unable to support existing or new load levels put on the structure. Due to increased loading, a change in use, corrosion, and other factors, many structurally inadequate buildings need reinforcing/strengthening [1, 2]. A novel technique of retrofit has been researched and deployed to boost the capacity of reinforced concrete structural parts in recent years [3]. Among the list, one method is externally bonded fibre reinforced polymer (FRP) which may significantly boost a structural member's static load capacity and its performance [4–6]. Aramid, carbon, and glass FRPs were more common. Presently, researchers are working to create more ecologically friendly FRP materials to replace synthetic FRP materials as a result of

current laws, increased public awareness of the need for environmental protection, and other factors [7, 8]. These fibres are the key reinforcing components in polymer matrices and transmit stress between them.

In recent years, the application of natural FRP reinforcement in the strengthening of flexure structures has grown in popularity. Awoyera et al. [9] used bamboo fibre laminate to undertake structural retrofitting of deteriorated reinforced concrete beams. Beams were initially subjected to corrosion studies, and then corroded beams were externally retrofitted using bamboo FRP. The ultimate load bearing capacity of the corroded beam was raised by 21.1 percent when bamboo laminate of single layer was used in the tensile zone, compared to the corroded beam without the retrofit. Raju and Mathew [10] and Sen and Jagannatha Reddy [11] compared behavior of natural and artificial FRP retrofitted beams via their maximum load bearing capacity. Zhang and

Teng [12] studied the RC beams strengthened with FRP for flexural strength with end cover separation.

Moreover, experimental study and finite element analysis (FEA) were performed in a few earlier works to examine the technology and relevance of using FRP composite to wrap concrete structures [13–15]. To simulate and analyze the outcomes of the experiments, FEA is used. Concrete beams which were retrofitted with carbon FRP sheets were analyzed by FEA and compared with experimental results [16–18], load deflection response, and failure modes were analyzed. Zhou et al. [19] demonstrated FE modeling of retrofitted beams employing carbon FRP laminates and a carbon flex. The peak load deflections of carbon flex retrofitted beams were found to be 67.8 percent and 73.1 percent greater than those of CFRP retrofitted beams, according to the study's findings. Damage mechanisms and loads bearing capabilities, strain/stress distributions, were quite similar to the experimental outcomes. Bouziadi et al. [20] studied creep response of carbon and glass FRP laminates externally reinforced concrete beams using nonlinear numerical analysis. The creep strain is greatly reduced when CFRP thickness is increased and orientation is altered. Also, the load improvement ratio mainly depends on the number of FRP layers used to retrofit the structures [21].

Haddad and Obaidat [22] verified the test data for shear deficient and heat damaged beams which were retrofitted with carbon FRP strips using near surface mounting technique using the FE model. Sen and Reddy [23] considered natural coir fibre composite to retrofit RCC beams and were simulated for ultimate load carrying capacity using FE analysis. Obaidat et al. [24] used the ABAQUS tool to verify FE analysis of carbon fibre reinforced plastic plate retrofitted beams with various lengths of FRP, with the experimental findings.

As on date, as per the literature data, a significant amount of experimental research works has been conducted in order to evaluate the behavior of structural elements reinforced with FRP. FE analyses on structures retrofitted with FRP plates have been carried out by the investigators. However, most of these studies are referred to RC beams. In this paper, the use of a 3D nonlinear FE method by the program ANSYS has been adapted to model the structural behavior of PTC beams unstrengthened and strengthened with S-FRP and J-FRP with different wrapping techniques. The current work focuses on wraping sisal and jute fibres on the surface of the beam material in two separate modes, strip wrapping and full length wrapping. Later, the parameters of the beam, such as deflection, were studied using ANSYS (commercially available finite element technique simulation software) with appropriate assumptions. The results were also compared to the experimental data. This study clarifies the behaviour of a beam in different wrapping modes. It is possible to investigate the effect of wrapping on a load-bearing capacity of beam.

2. Program of Study

2.1. Geometry of the Beam. The beams were 3400 mm long, 230 mm broad and 300 mm deep. Longitudinal steel bars: 2 nos. of diameter 10 mm each at the top and 2 nos. of diameter 12 mm each at bottom, and the sisal and jute FRP were used, having 3.62 mm thick approximately (supplied by Extra Weave Private Ltd., Cherthala, Kerala). The mix fraction for M-40 concrete was evaluated using the mix design described in IS: 10262-2009. River sand that was readily accessible in the area and the OPC 53 grade that complied with IS: 12269-1987 and IS: 8112-1989 were utilized as fine aggregate. In compliance with IS: 383-1970, a coarse aggregate measuring 12 mm was employed. In accordance with IS: 9103-1999 and IS: 456-2000, CON-PLAST SP430, supplied by Fosroc Pvt. Ltd., was utilized as the super plasticizer. According to IS: 10262-2009 specifications and a design strength of $40 \, \text{N/mm}^2$, calculated amounts of water, cement, coarse aggregate, and fine aggregate were combined in a ratio of $0.4 : 1 : 2.13 : 1.27$ to prepare a concrete. At various time intervals, the average compression strength was tested and found to be $22.7 \, \text{N/mm}^2$ for a 7-day cure, $38.95 \, \text{N/mm}^2$ for a 14-day cure, and $43.34 \, \text{N/mm}^2$ for a 28-day cure. Fe-500 HYSD bars having a tensile strength of $500 \, \text{N/mm}^2$ were also employed as reinforcement, was used according to IS: 1786-2008 standards. The flexural reinforcements were intended to withstand the overall loads and prevent flexural failure. Figure 1 shows the geometrical features of the beams.

2.2. Strengthening Scheme. Scheme "A" represents no strengthening. Under wrapping, two different wrapping schemes (a) full wrapping (b) strip wrapping with SFRP and JFRP were performed in the experimental program. Strengthening scheme- B1 is one layer jute fibre full wrapping with U shape, strengthening scheme- C1 is one layer jute strip wrapping with U shape and strengthening schemes- B2 and C2 are same of schemes B1 and C1, respectively, but with sisal fibre with U shape. Fibre laminate thickness is 3.62 mm approximately. The strengthening details are shown in Figures 2–4.

The experimental work of all these beams was conducted at the Structural Laboratory of the Department of Civil Engineering, Bangalore Institute of Technology, Bengaluru, details are shown in Figures 5 and 6. ASTM C 293 (center-point loading) was followed and the loading applied was at a rate of 5 kN/min

3. Numerical Analysis

Using the FE program ANSYS 18.1, 3D FE models of beams were analyzed. The fracture and failure analysis of all the FRP strengthened PSC beams of different wrappings were compared with controlled beams. Beams were modeled as similar to existing ones that were tested (as shown in Figure 1). To describe the behavior of concrete, steel reinforcement, and epoxy resin JFRP and SFRP laminates, suitable material models were used in the study. Concrete, reinforcement, jute/sisal FRP, and loading/boundary conditions are all factors to include in a standard FE model. Each of these components must be accurately represented in order to reflect the distinct qualities that each of them has. Modeling of concrete is done using a 3D brick, also known as
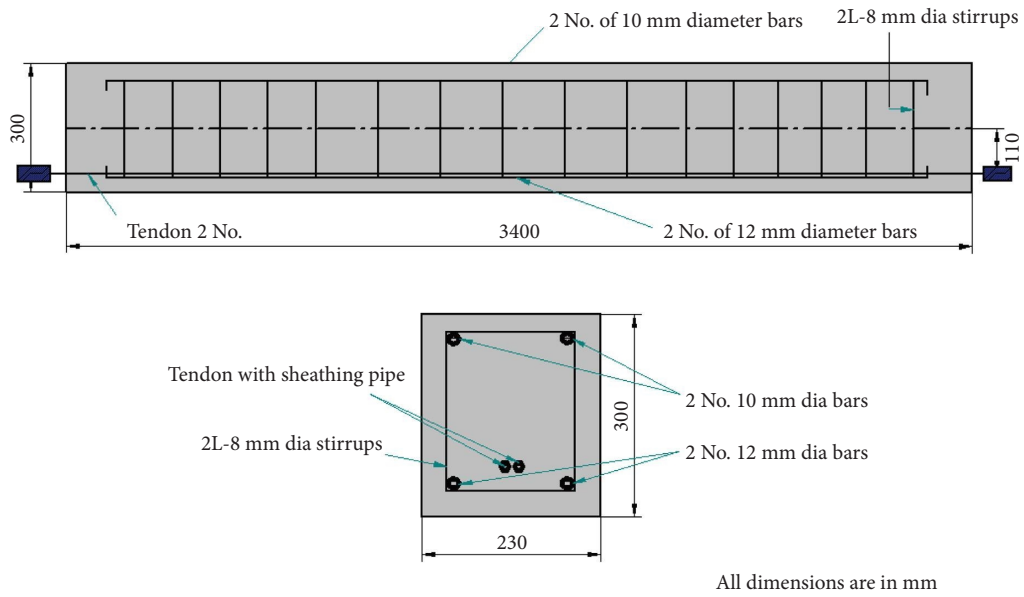
FIGURE 1: Geometrical details of beams.
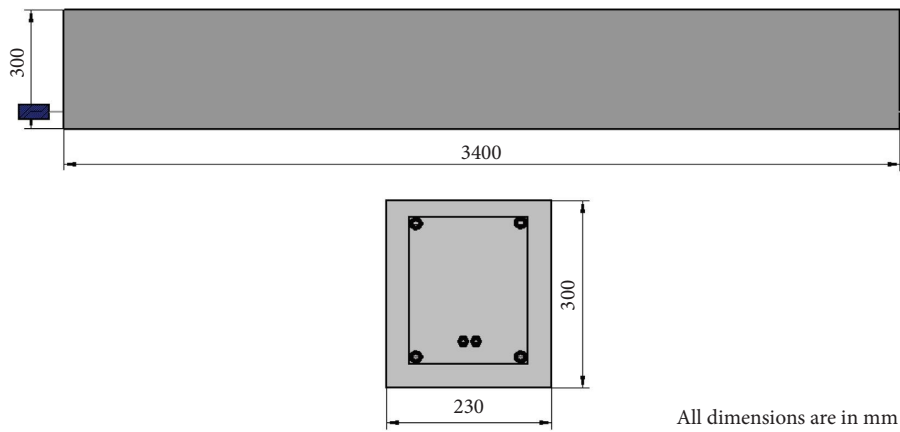
FIGURE 2: Control beams—no strengthening.
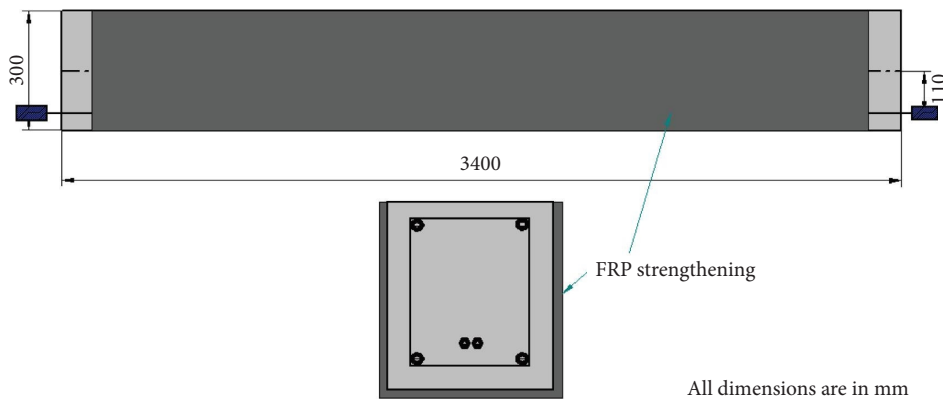
FIGURE 3: Strengthening scheme-1 full wrapping.

a solid element-designated as SOLID65 in ANSYS. This solid cubic element is having eight nodes, each having three DOF and translations in x, y, and z directions. This element type uses the mathematical material model of William and Warnk [25] and can represent cracking, crushing, plastic deformation, and creep [26]. In addition, the element may
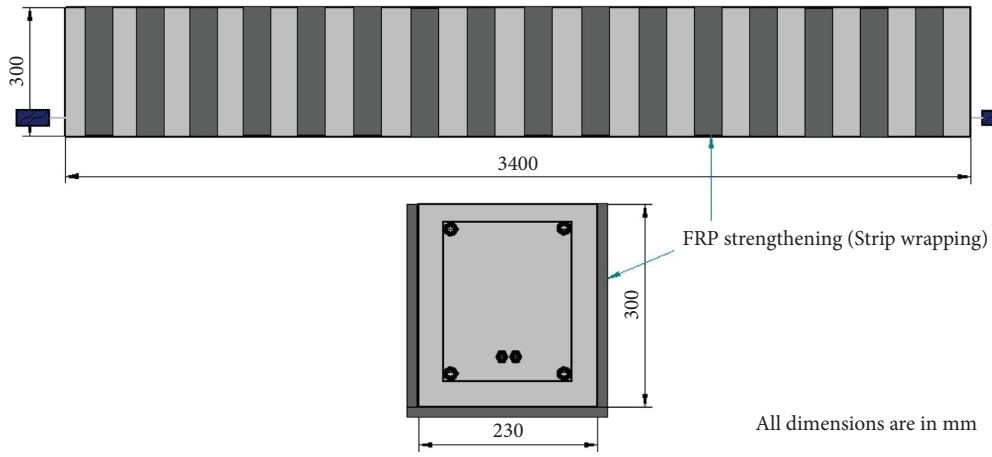
FIGURE 4: Strengthening scheme-2 strip wrapping.

(a)

(b)

(c)

(d)

(e)

(f)

(g)

(h)

FIGURE 5: Continued.

(i)

(j)

Figure 5: Experimental procedure followed (a) reinforcement, (b) sheathing pipe positioning, (c) reinforcement for installation, (d) positioned in shuttering, (e) concrete filling and compaction, (f) curing, (g) post tensioning, (h) filler application, (i) resin preparation, and (j) retrofitting with FRP.

(a)

(b)

Figure 6: Continued.
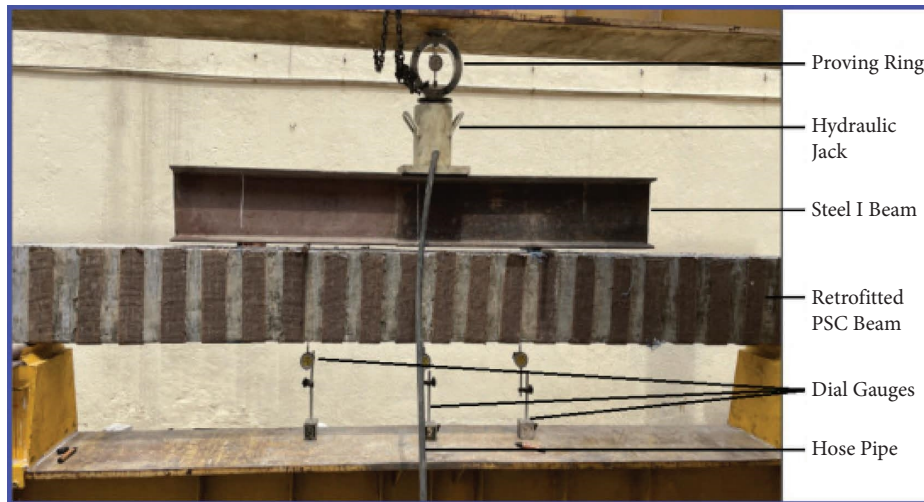
(c)

Figure 6: Laboratory setup (courtesy: Structural Laboratory, Department of Civil Engineering, Bangalore Institute of Technology, Bengaluru, India) (a) control beam, (b) full wrapping configuration, and (c) strip wrapping configuration.

simulate plastic deformation, cracking in three orthogonal dimensions, and crushing in three orthogonal directions. Steel reinforcement is represented in ANSYS using the spar/link element, which is designated as LINK8. Two nodes with three degrees of freedom translations in the x, y, and z axes make up this uniaxial bar-like element. Plasticity, creep, swelling, stress stiffening, and significant deflection are all examples of nonlinear phenomena that such reinforcing materials might simulate. A single layer Solid 45 element was utilized to signify FRP composites in the retrofitted beam and have been correlated to the FE model as shown in Figure 6. In general, solid brick elements (represented as SOLID45 or SOLID185 in ANSYS) may be utilized for 3D modeling of FRP sheets, bonding agents, and loading/end supports. A number of load increments (or) load steps were used to split the total load applied. Within tolerance limitations, at the end of each load increase, Newton–Raphson equilibrium iterations provide convergence. The solid 45 element nodes were linked to solid 65 element nodes at the interface to imitate flawless bonding of FRP sheets with concrete, as a result, inter connectivity was established.

3.1. Finite Element Model. The strengthening details shown in Figures 2–4, the meshed control and PSC beam models with the coupled FRP, are shown in Figure 7, as done in the ANSYS software platform.

3.2. Input Data, Loading, and Boundary Conditions. The material input data was derived from trial results of experiments, values supplied by the FRP laminate manufacturer, and data from the literature. Concrete compressive strength = 40 MPa, concrete elastic modulus = 31622.8 N/mm², and Poisson's ratio = 0.2 were used as material parameters for the concrete model. The yield strength of the reinforcing steel is 500 MPa, and the Poisson's ratio is 0.3,

according to the material characteristics. The mean elastic modulus and tensile strength of sisal fibres were about 19 GPa and 400 MPa, respectively, with a Poisson's ratio of 0.3 [27]. Young's modulus and tensile strength of jute fibres were about 20 GPa and 393 MPa, respectively, with a Poisson's ratio of 0.38 [28]. Simply supported, cantilever, or continuous conditions may be used to group the beams. As a result, to effectively describe the actual setup, the produced FE model must include realistic boundary conditions. Beam was modeled in symmetry. This may be accomplished by restraining the beam with rollers along the symmetry axis. The load combinations and supports were specified to be spread across an area relating to the metal plates and rollers employed in the testing, minimizing excessive stress concentrations. Surface pressures at the upper surface of the beams were used to determine the load combinations. Restraints were imposed to all nodes positioned anywhere along axis of the support rollers in order to accurately recreate the displacements and rotations for the supports, i.e., UY and UZ degree of freedom restrictions were imposed to all nodes orientated on the axis of the support rollers.

4. Results and Discussion

The FE and experimental data must be compared to determine the validity and predictability of the FE model. Throughout the loading application, the mid span deflection predicted from the FE analysis and observed in experimentation is compared to see whether predictions match experiment observations. The predicted and experimental outcomes are in close match. Loads were applied progressively with minimal load increases in concrete cracking, steel yielding, and the final phase in which a significant number of cracks occur. All beams are subjected to nonlinear static analysis. Figures 8(a)–8(d) depict the failure crack formation and load deflection details for the controlled
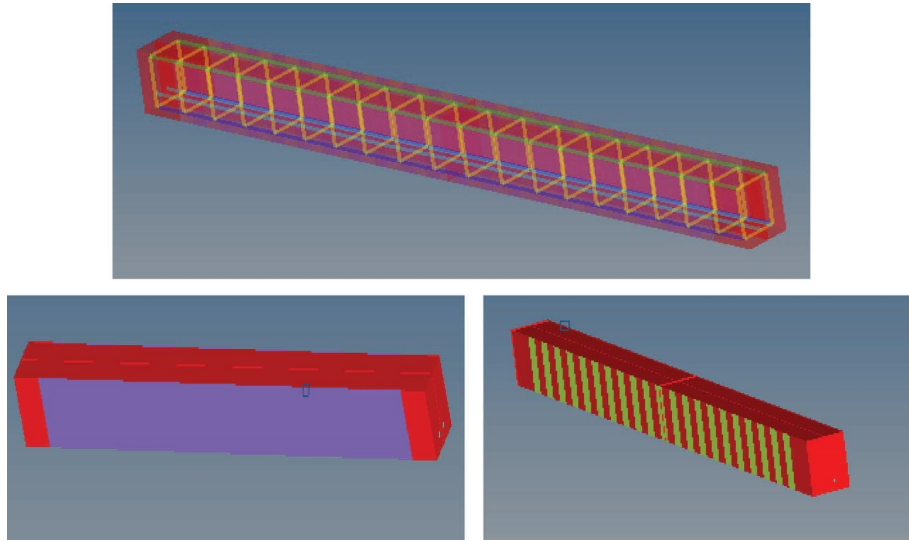
FIGURE 7: Meshed model of control and PTC beams with the coupled FRP.

(a)

(b)

(c)

(d)
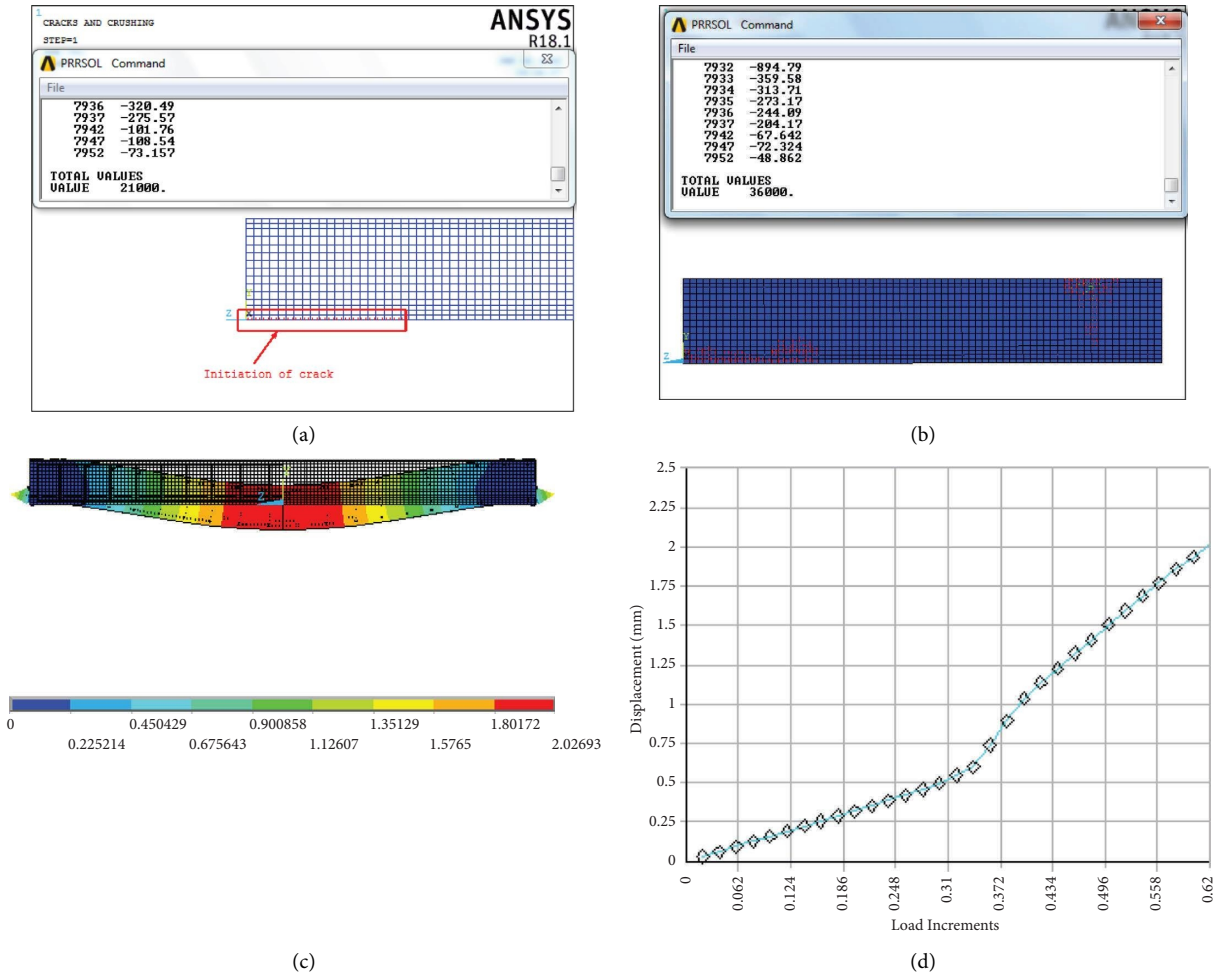
FIGURE 8: Predicted results from ANSYS for control beams. (a) Initial cracking behaviour, (b) intermediate cracking behaviour, (c) deflection contour of CB (FE), and (d) load deflection curve.

(a)

(b)

(c)

(d)
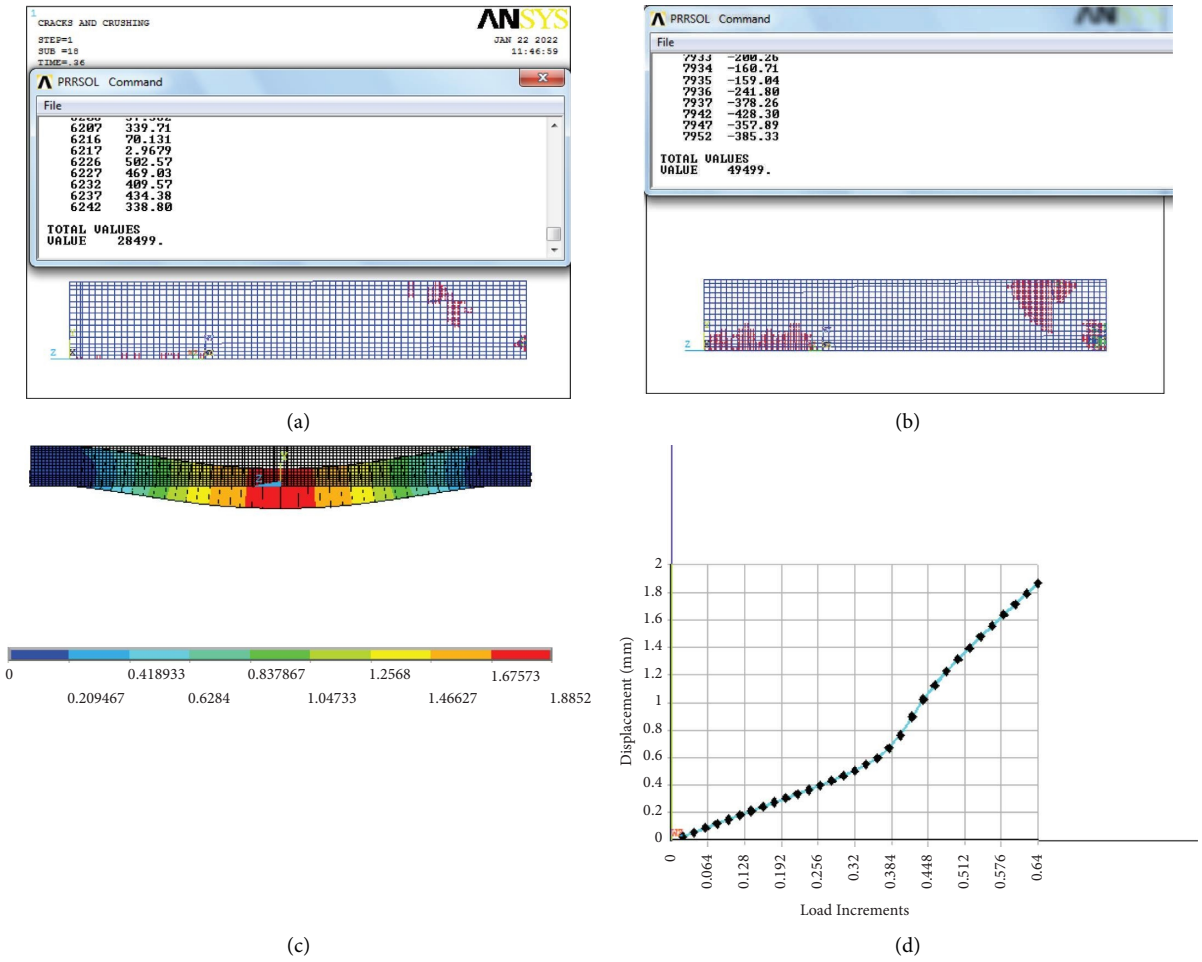
FIGURE 9: Predicted results from ANSYS for SFRP reinforced beams (strip wrapping). (a) Initial cracking behaviour, (b) intermediate cracking behaviour, (c) deflection contour, and (d) load deflection curve.

(a)

(b)
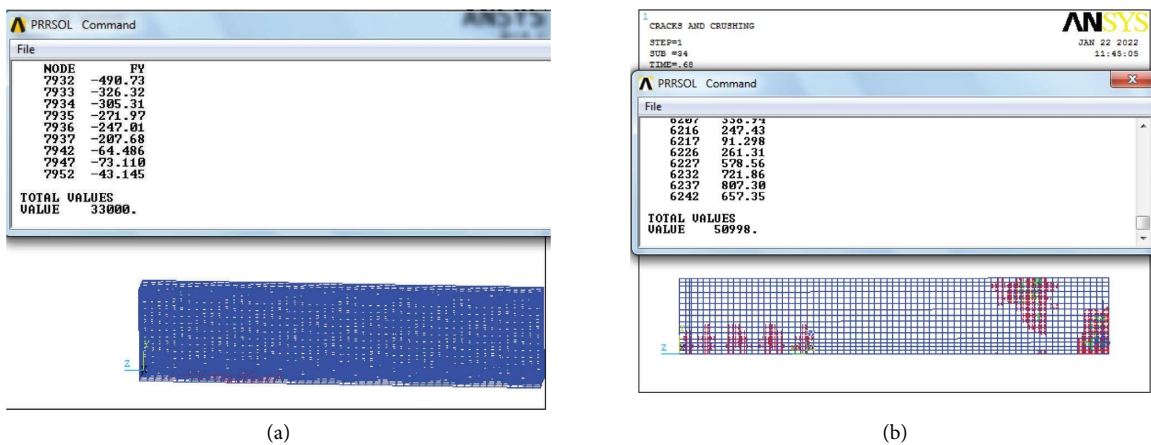
FIGURE 10: Continued.
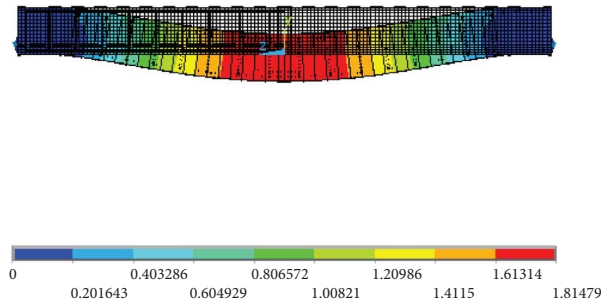
(c)
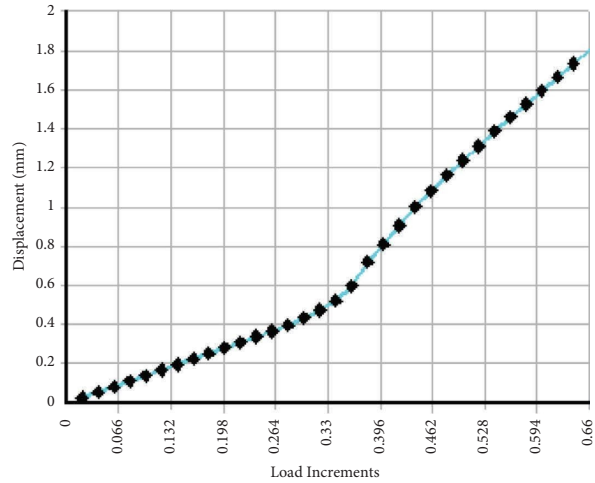
(d)

FIGURE 10: Predicted results from ANSYS for SFRP reinforced beams (full wrapping). (a) Initial cracking behaviour, (b) intermediate cracking behaviour, (c) deflection contour, and (d) load deflection curve.
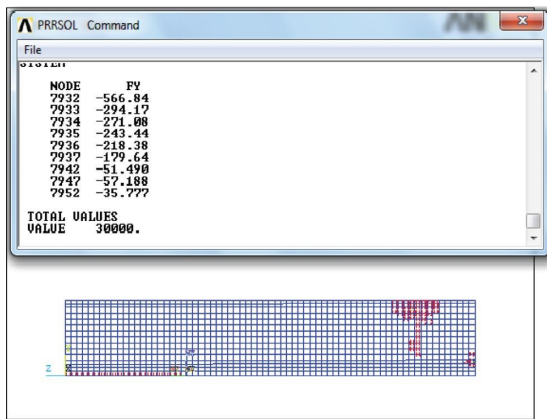
(a)
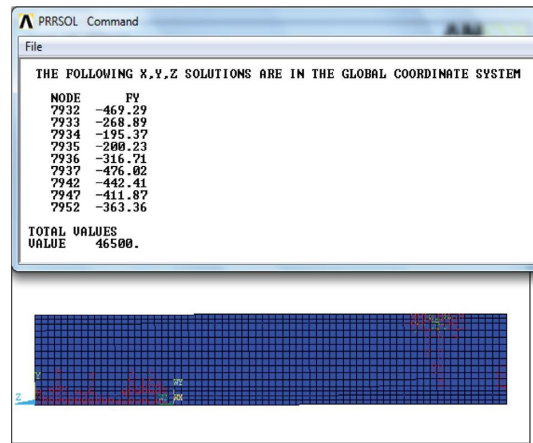
(b)
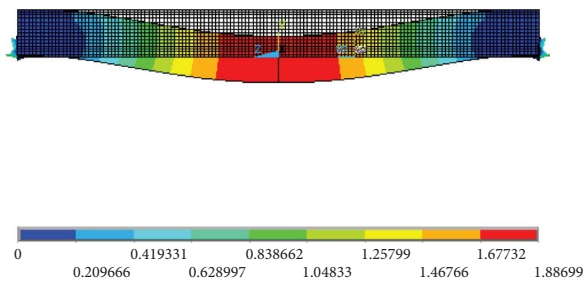
(c)
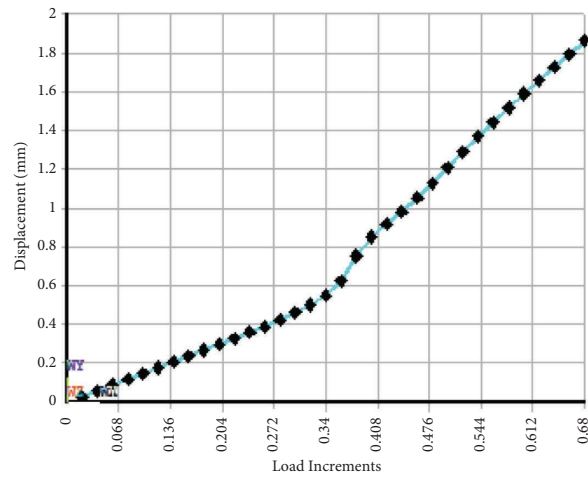
(d)

FIGURE 11: Predicted results from ANSYS for JFRP reinforced beams (strip wrapping). (a) Initial cracking behaviour, (b) intermediate cracking behaviour (c) deflection contour, and (d) load deflection curve.

(a)

(b)

(c)

(d)
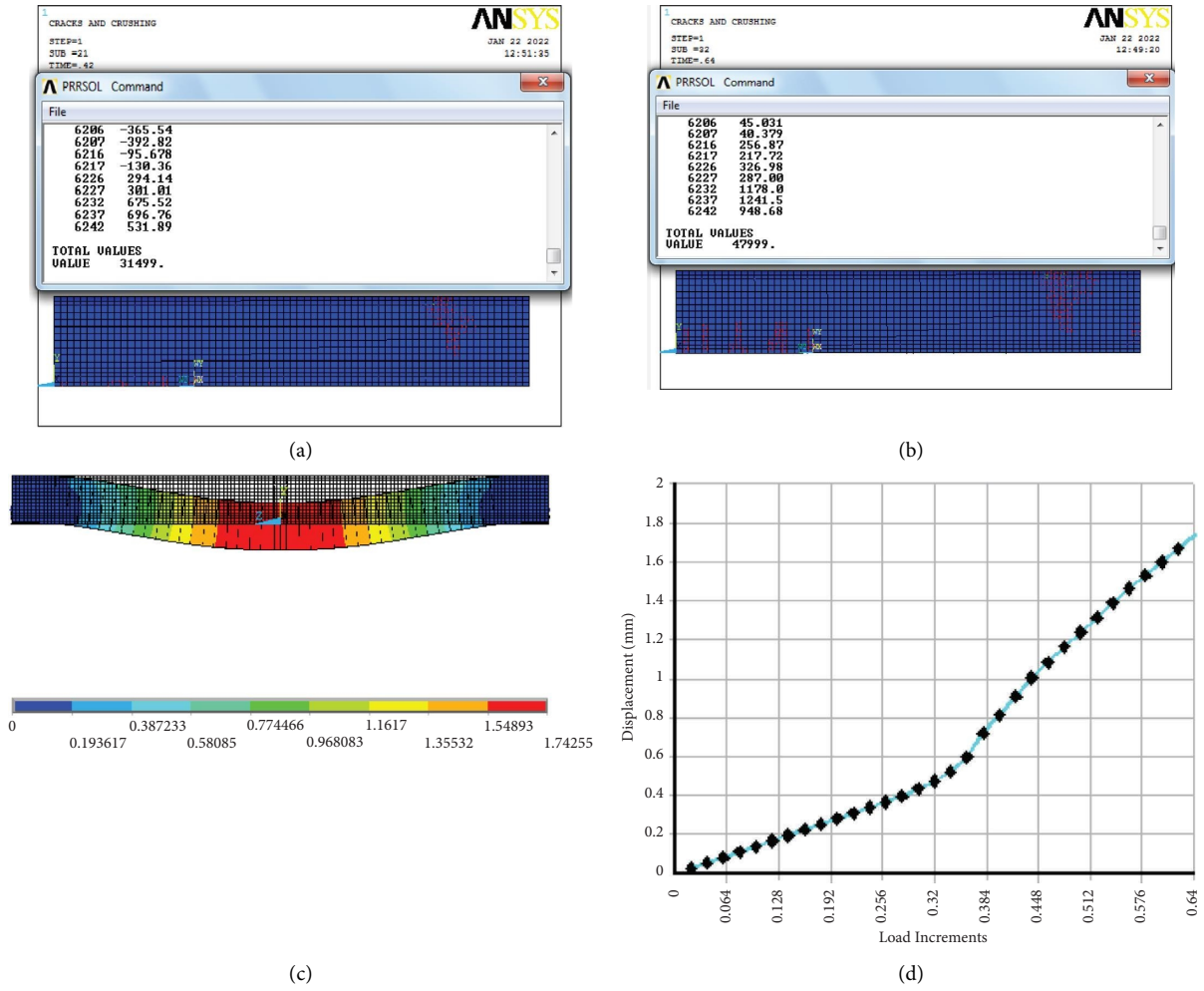
Figure 12: Predicted results from ANSYS for JFRP reinforced beams (full wrapping). (a) Initial cracking behaviour, (b) intermediate cracking behaviour, (c) deflection contour, and (d) load deflection curve.

Table 1: Comparative analysis between experimental and analysis results.

Sl. no.	Details	$(P_u)_{Exp}$ (N)	$(P_u)_{FE}$ (N)	% error
(1)	*Control beam*			
	Initial crack load	97500	84000	16
	Final crack load	154000	144000	7
(2)	*Sisal strip wrapping*			
	Initial crack load	130000	113996	14
	Final crack load	208750	197996	5.5
(3)	*Sisal full wrapping*			
	Initial crack load	114000	132000	14
	Final crack load	220000	203992	8
(4)	*Jute strip wrapping*			
	Initial crack load	113000	120000	6
	Final crack load	165000	186000	11
(5)	*Jute full wrapping*			
	Initial crack load	125000	125996	1
	Final crack load	172500	191996	10

beam (without any FRP retrofitting), which reveals cracks in the flexure zone. The failure crack pattern for the sisal FRP (strip wrapped), Figures 9(a)–9(d) sisal FRP (strip wrapped)

retrofitted PSC beam is clearly visible, with fracture spreading from the right support through the applied load and concrete disruption in the zone. The crack pattern
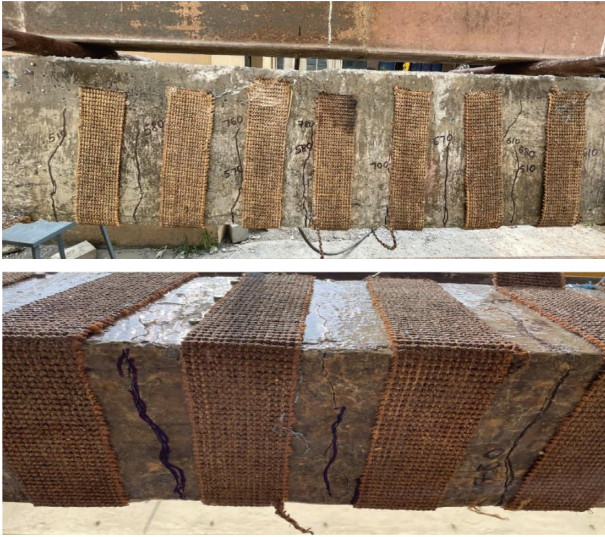
FIGURE 13: Crack propagation pattern of the experimental beams.

depicting the behavior of the sisal FRP retrofitting beam is quite close to the fracture pattern indicated by the experiments. Figures 10(a)–10(d) show the failure crack pattern for the sisal FRP (full wrapped) and jute FRP (full wrapped) retrofitted PSC beams. It shows the cracks as well as the concrete disruption in the flexure zone. The behavior of the controlled and retrofitted beams as illustrated by the crack outline is extremely close to the crack outline as demonstrated by the experiments in [29]. The failure crack pattern for the jute FRP (strip wrapped), Figures 11(a)–11(d) jute FRP (strip wrapped) retrofitted PSC beam, the crack pattern depicting the behavior of the jute FRP retrofitting beam is quite close to the fracture pattern indicated by the experiments. The failure crack pattern for the jute FRP (full wrapped), Figures 12(a)–12(d) jute FRP (full wrapped) retrofitted PSC beam, the crack pattern depicting the behavior of the jute FRP retrofitting beam is quite close to the fracture pattern. In terms of the quality point of view, the predicted results provided by the damaged model match the observed behavior extremely well. Table 1 represents the comparative structure of experimental and analysis results obtained from ANSYS. Figure 13 demonstrates the crack propagation in the beams during experimentation.

5. Conclusion

In the study, 18 specimens were fabricated, strengthened using SFRP and JFRP with different wrapping configuration, and successfully tested under a 4-point bending test. In general, the results indicate that all externally strengthening beams have significantly improved the load-carrying capacity and performance in comparison with control beams. To simulate the response in flexure of control and strengthened PTC beams using SFRPs and JFRPs, a 3D nonlinear FE model was developed. The suggested model was tested against the experimental data; the following conclusions may be taken based on the findings of the current study:

(1) When compared to control specimens, the load bearing capability of PTC beam models may be improved by retrofitting sisal and jute fibres

(2) Overall, the computational and experimental findings were in excellent agreement when comparing ultimate load bearing capacity and mid-span deflection at failure

(3) As compared to the control specimen, the load bearing capability of the beam modified with sisal fibre using strip and complete wrapping processes around in all four sides is increased by 35.55 percent and 42.85 percent, respectively

(4) In comparison to the control specimen, the load bearing capability of the beam retrofitted with jute fibre using strip and complete wrapping processes around all four sides is increased by 7.14 percent and 12.01 percent, respectively.

The study may be further extended for measuring efficacy of strengthening of beam (under both flexural and shear) can be measured by using other available bio composites in various degrees of wrapping configurations (60° and 45°).

Data Availability

The data used to support the findings of this study are included within the article.

Conflicts of Interest

The authors declare that there are no conflicts of interest regarding the publication of this article.

References

[1] M. K. Askar, A. F. Hassan, and Y. S. Al-Kamaki, "Flexural and shear strengthening of reinforced concrete beams using FRP composites: a state of the art," *Case Studies in Construction Materials*, vol. 17, Article ID e01189, 2022.

[2] A. Zheng, Z. Liu, F. Li, and S. Li, "Experimental investigation of corrosion-damaged RC beams strengthened in flexure with FRP grid-reinforced ECC matrix composites," *Engineering Structures*, vol. 244, Article ID 112779, 2021.

[3] W. Aules, Y. M. Saeed, and F. N. Rad, "A novel anchorage system for strengthening slender RC columns with externally bonded CFRP composite sheets," *Construction and Building Materials*, vol. 245, Article ID 118423, 2020.

[4] R. Z. Al-Rousan and A. Alkhawaldeh, "Numerical simulation of the influence of bond strength degradation on the behavior of reinforced concrete beam-column joints externally strengthened with FRP sheets," *Case Studies in Construction Materials*, vol. 15, Article ID e00567, 2021.

[5] M. Panahi, S. A. Zareei, and A. Izadi, "Flexural strengthening of reinforced concrete beams through externally bonded FRP sheets and near surface mounted FRP bars," *Case Studies in Construction Materials*, vol. 15, Article ID e00601, 2021.

[6] R. Kotynia, E. Oller, A. Mari, and M. Kaszubska, "Efficiency of shear strengthening of RC beams with externally bonded FRP

materials-State-of-the-art in the experimental tests," *Composite Structures*, vol. 267, Article ID 113891, 2021.

[7] G. Luo, X. Li, Y. Zhou, L. Sui, and C. Chen, "Replacing steel stirrups with natural fiber reinforced polymer stirrups in reinforced concrete Beam: structural and environmental performance," *Construction and Building Materials*, vol. 275, Article ID 122172, 2021.

[8] C. O. Nwankwo, J. Mahachi, D. O. Olukanni, and I. Musonda, "Natural fibres and biopolymers in FRP composites for strengthening concrete structures: a mixed review," *Construction and Building Materials*, vol. 363, Article ID 129661, 2023.

[9] P. O. Awoyera, T. A. Nworgu, B. Shanmugam et al., "Structural, retrofitting of corroded reinforced concrete beams using bamboo fiber laminate," *Materials*, vol. 14, no. 21, p. 6711, 2021.

[10] A. Raju and L. A. Mathew, "Retrofitting of RC beams using FRP," *International Journal of Engineering Research and Technology*, vol. 2, no. 1, pp. 1–6, 2013.

[11] T. Sen and H. Jagannatha Reddy, "Efficacy of bio derived jute FRP composite based technique for shear strength retrofitting of reinforced concrete beams and its comparative analysis with carbon and glass FRP shear retrofitting schemes," *Sustainable Cities and Society*, vol. 13, pp. 105–124, 2014.

[12] S. Zhang and J. G. Teng, "Finite element analysis of end cover separation in RC beams strengthened in flexure with FRP," *Engineering Structures*, vol. 75, pp. 550–560, 2014.

[13] K. A. Deen Bsisu, H. H. Hussein, and S. M. Sargand, "The use of Hashin damage criteria, CFRP–concrete interface and concrete damage plasticity models in 3D Finite element modeling of retrofitted reinforced concrete beams with CFRP sheets," *Arabian Journal for Science and Engineering*, vol. 42, no. 3, pp. 1–14, 2016.

[14] S. Barour, A. Zergua, F. Bouziadi, and W. Abed Jasim, "Finite element analysis of CFRP externally strengthened reinforced concrete beams subjected to three point bending," *World Journal of Engineering*, vol. 17, pp. 183–202, 2020.

[15] T. Sen Umesh Mishra and B. S. Shubhalakshmi, "Nonlinear finite element analysis of retrofitting of RCC beam column joint using CFRP," *International Journal of Engineering and Technology*, vol. 2, no. 5, pp. 459–467, 2010.

[16] J. Deng and M. M. K. Lee, "Effect of plate end and adhesive spew geometries on stresses in retrofitted beams bonded with a CFRP plate," *Composites Part B: Engineering*, vol. 39, no. 4, pp. 731–739, 2008.

[17] R. A. Hawileh, M. Z. Naser, and J. A. Abdalla, "Finite element simulation of reinforced concrete beams externally strengthened with short-length CFRP plates," *Composites Part B: Engineering*, vol. 45, no. 1, pp. 1722–1730, 2013.

[18] M. Barbato, "Efficient finite element modelling of reinforced concrete beams retrofitted with fibre reinforced polymers," *Computers & Structures*, vol. 87, no. 3-4, pp. 167–176, 2009.

[19] H. Zhou, T. L. Attard, Y. Wang, J A. Wang, and F. Ren, "Rehabilitation of notch damaged steel beams using a carbon fiber reinforced hybrid polymeric-matrix composite," *Composite Structures*, vol. 106, pp. 690–702, 2013.

[20] F. Bouziadi, B. Boulekbache, A. Haddi, M. Hamrat, and C. Djelal, "Finite element modeling of creep behavior of FRP externally strengthened reinforced concrete beams," *Engineering Structures*, vol. 204, Article ID 109908, 2020.

[21] A. W. Al Zand, W. H. W. Badaruzzaman, A. A. Mutalib, and A. H. Qahtan, "Finite element analysis of square CFST beam strengthened by CFRP composite material," *Thin-Walled Structures*, vol. 96, pp. 348–358, 2015.

[22] R. H. Haddad and Y. T. Obaidat, "A nonlinear finite element model for shear deficient heat-damaged concrete beams repaired using NSM CFRP strips," *Construction and Building Materials*, vol. 170, pp. 314–325, 2018.

[23] T. Sen and H. N. J. Reddy, "Finite element simulation of Retrofitting of RCC beam using coir fibre composite (Natural Fibre)," *International Journal of Innovation, Management and Technology*, vol. 2, no. 2, pp. 175–179, 2011.

[24] Y. T. Obaidat, S. Heyden, and O. Dahlblom, "The effect of CFRP and CFRP/concrete interface models when modelling retrofitted RC beams with FEM," *Composite Structures*, vol. 92, no. 6, pp. 1391–1398, 2010.

[25] K. Willam and E. Warnk, "Constitutive model for the triaxial behavior of concrete," *Proceedings of International Association of Bridge Structural Engineers*, vol. 19, no. 1–30, 1975.

[26] M. Z. Naser, R. A. Hawileh, and J. Abdalla, "Modeling strategies of Finite element simulation of reinforced concrete beams strengthened with FRP: a Review," *Journal of Composites Science*, vol. 5, no. 1, p. 19, 2021.

[27] F. D. A. Silva, R. D. T. Filho, J. D. A. M. Filho, and E. D. M. R. Fairbairn, "Physical and mechanical properties of durable sisal fiber–cement composites," *Construction and Building Materials*, vol. 24, no. 5, pp. 777–785, 2010.

[28] A. Sengupta and S. Kumar, *Study of a Model Slope Reinforced with Jute, Recent Advances in Modeling lL and Slides and Debris F Flows*, Springer Series in Geomechanics and Geo-engineering, Berlin, Germany, 2015.

[29] D. P. Archana, H. N. Jagannatha Reddy, N. Jeevan, R. Prabhakara, M. U. Aswath, and B. Paruti, "Natural jute fibre-reinforced polymer composite system for post tensioned beam strengthening in flexure," *Advances in Materials Science and Engineering*, vol. 2021, Article ID 2905150, 14 pages, 2021.

Research Article

Generative Design of Housing Spatial Layout Based on Rectangular Spaces

Javid Ahmadi,[1] **Seyyed Mehdi Maddahi** ⬤,[2] **and Reza Mirzaei**[1]

[1]*Department of Architecture, Birjand Branch, Islamic Azad University, Birjand, Iran*
[2]*Department of Architecture, Iran University of Science and Technology, Tehran, Iran*

Correspondence should be addressed to Seyyed Mehdi Maddahi; sm.madahi@gmail.com

The generative spatial layout design process can generate and optimize a wide range of design responses by complying with all desired requirements and criteria and evaluating them based on one or more specific functions. Considering the complexities and diversity of spatial layout responses, it is important to know the various mechanisms of the product design process related to them. Based on this, the aim of this research is to provide a mechanism for designing a generative spatial layout (GSL) based on a housing design problem. The method of this research with a quantitative approach is the simulation and placement of spaces through coding in Grasshopper and Python software under the Grasshopper platform. The main variables of the research are the dimensions of the spaces of the residential unit, the proximity matrix, and the spatial relationships of the residential unit. With the restrictions made, 440 spatial layout responses were produced in four general shapes, including an incomplete square, a rectangle with a one-to-two ratio, an incomplete rectangle with an incomplete one-to-two ratio, and L-shape. The geometrical data of production plans have been subjected to correlation and linear regression tests in the SPSS software. Two models have been developed based on the perimeter of the plan and the area of its peripheral rectangle. Based on the obtained results, GSL design will be able to provide more favorable solutions. The results indicate that, by providing the design constraints in all the results, the area-oriented approach to the productive design of housing configurations can serve as an assistant mechanism for the designer in providing a variety of floor plans in terms of area for the designer.

1. Introduction

As one of the main indicators of social stability, housing is one of the main factors of interest in sustainable development [1]. The final report of the Brandt Commission presents housing as one of the key needs of developing countries [2]. Therefore, the housing design process is one of the most important aspects of architecture. Designing the configuration of housing space is one of the tasks of housing design, which is very important in the early stages, including "conceptual design" [3] and "design development." In this research, housing spatial layout is defined as the allocation of different housing spaces, and it is decided based on the placement of internal partitions as well as external walls.

Comparing a large set of configuration alternatives is necessary to identify the optimal design solution. But due to the variety of relationships and spatial arrangement, the housing design process has many complications. The computational design process offers an opportunity to automate the generation of design alternatives based on parametric and algorithmic rules. Generative spatial layout (GSL) design is to use a computational process to generate a large set of alternative configurations in a reasonable time frame. In fact, in this structure, the main goal is to help building design professionals explore a larger set of solutions, which a traditional trial and error process can never achieve [4]. Based on this, this research intends to provide a mechanism for the design of generative spatial layout (GSL), by defining a housing design problem, to conduct a comprehensive search in all types of housing spatial layouts. Spatial layout design in this research is defined as finding a set of answers, including the location of spaces and

the possible dimensions of each, which meet all design requirements and maximize design quality in terms of design priorities. Spatial layout is related to all physical design problems. Therefore, it is an important area of research [5]. The application of precise mathematical optimization methods to improve architectural layouts has been studied for several decades [6]. In the last few decades, researchers have developed different approaches to create interior building layouts in styles similar to existing well-known or historical design paradigms. This field provides solutions for automating the layout design process.

Reported efforts to automate the layout design process began in the 1970s [7]. Researchers have used several problem representations and solution search techniques to describe and solve problems. Sydora and Stroulia developed a BIM-based rule grammar and described interior design rules in a machine-readable format, by which the automatic generation of interior design models can be realized [8]. Wang et al. implemented a generative algorithm called City Engine and created the texture of blocks as close as possible to real blocks in urban design [9]. A generative grammar was developed in analyzing the spatial shape of case examples of blocks in the city of Nanjing [9]. Architectural arrangement is one of the most important subjects of generative spatial layout (GSL) design. Because in addition to common engineering goals such as cost and performance, architectural design is especially concerned with the aesthetic qualities and usability of an arrangement, which are usually more difficult to formally describe [10]. Also, the components of a building layout (rooms or walls) often do not have predefined dimensions, so each component of the layout can be resized.

This research represents a unique innovation when compared to other related studies in relation to the configuration production process, introduction, analysis of the produced configurations, and the introduction of an analytical parameter to obtain more favorable results. This research focuses on developing a point-finding method based on an area-based approach in the configuration production process. To facilitate future development, we have also analyzed the responses obtained through linear regression based on two dependent variables: the planning environment and the perimeter rectangle. To improve responses and reach more practical configurations, the perimeter rectangle is introduced and analyzed.

2. Generative Spatial Layout Design Approaches

In general, several methods for designing generative spatial layout (GSL) have been of interest among researchers. One of the ways to assign space and define spatial layout is to define the available space as a set of squares in a grid and use an algorithm to assign a number of squares based on a set of restrictions to a specific room or activity [11, 12]. This method is known as grid-base layout in researches. For the grid-based method, dividing a given design into unit spaces can turn this design into a set of grid cells. Since each cell has a fixed position and size, this design involves a two-dimensional matrix, which has ordered points [13]. This

problem is inherently discrete and multistate. It cannot be solved due to the complexity of the composition and the problems of the right-sized layout. Several heuristic strategies are developed to find solutions without exhaustively searching the design space. The second method is the zone-based layout, which was proposed in the 1990s by Montreuil [14]. In this method, the range of spaces can be changed based on the end boundaries. This method basically requires a coordinate system to represent the space with corner points. In the area-based design, boundary lines are defined as a measure of central points [13]. Both methods have been studied and used in recent configuration studies with different coding methods [5, 15, 16] (see Table 1).

Another way to represent the design space of a building plan is to decompose the problem into two parts: topology and geometry. Topology refers to the logical relationships between design components. Geometry refers to the position and size of each component in the design. Topology decisions define constraints for the geometric design space [5]. For example, a topological decision that room one is adjacent to the north wall of room two constrains the geometric coordinates of room one relative to room two. In the meantime, combined methods are obtained from the above methods. Based on this, four general methods can be explained. Therefore, the research conducted in the field of generative spatial layout design has been divided according to the four proposed methods, and the design variables of each research have been obtained. Also, the general form of configuration in each research is explained. The results can be seen in Table 2. As it is clear in the table, the network-based approach has received more attention than other methods. After that, the area-based method is the most frequent. Also, various variables have been investigated in researches. The dimensions and location of spaces, as the most important variables in spatial arrangement, have the highest frequency in the investigated researches. In general, the characteristics of the window have been given a lot of attention in researches. But this variable has been considered as a control variable in most of the researches, or it has been placed only in relation to the external space. Other variables, such as orientation, boundary dimensions, and shading, are targeted depending on the research objectives (Table 2).

Based on the investigations, this article introduces an approach to automatically generate plans based on rectangular spaces with the ability to improve and further customize. It automatically reproduces various plans and implements transformation rules to manipulate the spatial relationships between rooms and create modified plans according to specific requirements. This research approach introduces constraints such as the adjacency matrix, the width-to-length ratio, and the bounding rectangle bounding the overall plan to support flexibility for different design requirements. In this research, a graphical user interface is provided for users to perform the automatic production process. An experiment has been conducted to verify the feasibility of this research approach and the time spent in producing floor plans. This shows that the method of this research is able to create a set of customized plans in a reasonable time.

TABLE 1: Comparison of different approaches to design GSL.

Approach	General method	Strengths	Limitations
Axis area	Using changeable end boundaries to define the scope of each space	Coding is easy Dimensions are not limited	An absence of a fixed outer boundary A lack of diversity in the design of interior spaces
Network oriented	In a grid, assign a set of cells to each space	Different types of spaces are available An outer border that can be fixed	Spaces and cells should be measured according to their dimensions Complex designs require heavy coding
Topological	A space is defined by its topology and geometry	Spaces that should be prioritized Fixing the outer border may be possible	Access to a variety of shapes of spaces is not optimal Some designs have a high level of coding complexity
Hybrid	Combinations of the three methods described above	Using the potential and avoiding the limitations of different methods	The complexity of hybrid coding The absence of a written path

TABLE 2: Researches in the field of configuration and topics related to it (source: author).

Author	Form	Production method	Design variables
Keshavarzi and Rahmani-Asl, 2021 [17]	One-story multiform	Axis area	Space location, adjacency matrix, and Furniture location
Nauata et al., 2021 [18]	One-story multiform	Hybrid	Space location, adjacency matrix, door location, space dimension, and door dimension
Veloso et al., 2018 [19]	One-story polygon form	Axis area	Space location, adjacency matrix, door location, and space dimension
Boonstra et al., 2018 [20]	Multistorey rectangle	Hybrid	The dimensions of the spaces and the location of the spaces
Schwartz et al., 2017 [21]	Multistorey rectangle	Axis area	The dimensions of the spaces, the location of the spaces, and the window-to-wall ratio
Dino and Üçoluk, 2017 [22]	Multistorey rectangle	Network oriented	Space dimension index, position matrix, space position, window-to-wall ratio, and height-to-area ratio
Sleiman et al., 2017 [23]	Multistorey rectangle	Axis area	Location of space, dimensions of space, and location of crates
Dino and Üçoluk, 2017 [22]	Multistorey rectangle	Network oriented	Space dimension index, position matrix, space position, window-to-wall ratio, and height-to-area ratio
Yi, 2016 [13]	One-story rectangle	Network oriented	Boundary dimensions, space location, space dimensions, and window-to-wall ratio
Su and Yan, 2015 [24]	One-story rectangle	Network oriented	The location of the rooms
Rodrigues et al., 2013 [16]	Multistorey rectangle	Axis area	The dimensions of the spaces, the location of the spaces, the position of the window and the door, the spatial relationship, the floors, and the location. Space, border dimensions, orientation, window orientation, and shading dimensions
Bausys and Pankrasovaite, 2005 [25]	One-story rectangle	Axis area	Boundary dimensions, space position, space dimensions, window position, and window dimensions
Caldas, 2008 [26]	Multistorey rectangle	—	Space dimensions, space height, roof slope, roof orientation, and window dimensions
Michalek et al., 2002 [5]	One-story rectangle	Topologic	Space position, space dimensions, window position, window dimensions, and spatial relationship

3. Methodology

The method of this research is a quantitative approach, simulation, and placement of spaces, and the use of the target space is residential. Finally, evaluation of research findings through organized statistical methods has been considered. The research simulation tool is Grasshopper software and Python programming language in the Grasshopper platform. Based on the main elements of housing design, design parameters should be summarized and defined.

Through the analysis of the overall residential design process, basic design parameters, such as internal circulation space, room function, orientation, room size, functional relationships, building envelope, and layout of a typical floor plan, can be determined. These parameters can be divided into two types. The first type refers to parameters related to sizes, areas, and coefficients, which can be described numerically, and includes the unit area, the room area, room depth, the room depth to width ratio (DWR), floor height, the door size, the window to wall ratio (WWR), and the window width to height ratio (WHR). The parameters of the second type include elements that cannot be described numerically, such as orientation, spatial arrangement, shape of circulation space, and relationships between rooms, which should be converted into parameters that can be recognized by the algorithm. Therefore, two types of design parameters include quantitative parameters that can be described numerically and qualitative parameters that cannot be represented by numbers. In this research, the most important limiting variables of the algorithm include the total area of the residential unit, the variety of interior spaces, the minimum and maximum areas of each interior space based upon its function, the general shape of the plan of the interior spaces, and the proximity of different functions to one another. Depending on the limiting variables, the algorithm produces a different set of residential plans.

The area of the desired residential unit is 90 square meters. In the assumption of the research, all the spaces of the residential unit are defined as rectangular and in the longitudinal and transverse axis of the residential unit. There are six spaces in the residential unit including kitchen, living, W.C, bathroom, and two bedrooms next to an entrance. Also, in order to define the minimum dimensions of the spaces, first through the criteria of the Road, Housing and Urban Development Research Center [24], minimum dimensional standards have been obtained, and then through the Delphi method and by an open questionnaire and interview, its validity has been confirmed by experts. In order to reach the possible area of the available spaces in the algorithm, we act according to the following formula. Assuming the existence of n spaces ($a, b, c, ..., n$), the maximum and minimum possible area of space (a) in the desired total area (S_{all}) is based on the minimum standard area obtained for each space.

$$\text{Max}\left(\text{Est. S}_{\text{Space}(a)}\right) = S_{\text{all}} - \sum_{i=1}^{n-1} \text{Min}\left(\text{Sta. S}_{\text{Space}(i)}\right). \quad (1)$$

In this formula, the maximum estimated area of each space (Sta. $S_{\text{Space}(a)}$) in the total area (S_{all}) is obtained based on the sum of the minimum standard area of other spaces (Sta. $S_{\text{Space}(i)}$). The estimated area of each space is the area of the space without considering the communication paths and the walls of the space. After obtaining the maximum possible area of each space, the area range of each space has been obtained. Based on this and based on the minimum standard length and width of residential spaces, all the length and width states of each space can be obtained. For this purpose, a set of code has been written in Python. By having the length and width of each of the spaces in each of the states, the range and shape of the space can be drawn. Also, in order to determine and define adjacent spaces in the plan, the proximity matrix of spaces has been determined, and then through the Delphi method with open questionnaires and interviews, its validity has been confirmed by experts in the field of housing. The adjacency matrix defines the spaces that are directly connected to each other.

Based on the proximity matrix and in the form of code written in Python, the drawn spaces are placed together. Finally, the plan obtained from the arranged spaces is enclosed in a rectangle, and the empty spaces between the plan and the rectangle are reduced as much as possible so that the plan is close to the perfect rectangle. Also, the small empty spaces between the six spaces are added to the adjacent space that shares the most perimeter with it. Next, the linear results are entered into the modeling algorithm. The walls have thickness, and the doors and windows are defined according to the standards. Windows are located exactly in the middle of all external walls of the rooms, except for the zero-zero sides of the standard plan. Finally, after producing the final plans, the data of all the plans including the length, width, and area of each space, the perimeter of the final plan, and the area of the rectangle surrounded by the final plan have been collected. These data have been analyzed by descriptive statistics and analytical tests including correlation and regression. It is expected that the results of these tests can ultimately improve the processes of automatic production of spatial layout.

3.1. Findings of Automatic Design of Spatial Layout of Housing and Final Answers. As mentioned, this research aims to design a spatial layout generator through Grasshopper and Python software, and the housing spaces include the kitchen, living room, two bedrooms, W. C, bathroom, and entrance with a general rectangular shape with standard dimensions located next to each other. For this purpose, first, the minimum standard dimensions of each housing space have been obtained based on the criteria of the Road, Housing and Urban Development Research Center [24], and it has been approved by experts in the field of housing, which is as follows (Table 3).

TABLE 3: Standard dimensions of residential spaces based on the criteria of the Road, Housing and Urban Development Research Center [24].

	Entrance	Kitchen	Living room	Parents' bedroom	Child's bedroom	W. C and bathroom
Minimum length and width	1.4	2.4	3.3	2.4	2.4	1.1
Minimum standard area	2.5	5.8	15	12	7.2	1.25

Based on the dimensions obtained through the standards, the minimum possible area of residential spaces based on the total area of 90 square meters is obtained according to the following formula:

$$\text{Max}\left(\text{Est. } S_{\text{Space}(a)}\right) = 90m^2 - \sum_{i=1}^{5} \text{Min}\left(\text{Sta. } S_{\text{Space}(i)}\right). \quad (2)$$

In this formula, the maximum estimated area of each space (Sta. $S_{\text{Space}(a)}$) is obtained at 90 square meters based on the sum of the minimum standard area of other spaces (Sta. $S_{\text{Space}(a)}$). Based on the findings, by following the standards here, the living can vary from 15 square meters to 50 meters and the parents' bedroom from 12 to 25 square meters. Also, a single bedroom from 2.7 square meters to 17 meters is possible (Table 4).

After obtaining the maximum possible area of each space, the area range of each residential space has been obtained. The sum of these obtained areas plus the area of the building walls and possible communication spaces may be less or more than 90 square meters. For this reason, there is a need to reduce the range of changes in the area of all spaces. For this purpose, first, the domain of each area is converted into a smaller domain according to the following formula. The following formula defines the final minimum and maximum area:

$$\text{Max}\left(\text{Poss. } S_{\text{Space}(a)}\right) = \text{Max}\left(\text{Est. } S_{\text{Space}(a)}\right) - \left[\left(\text{Max}\left(\text{Est. } S_{\text{Space}(a)}\right) - \text{Min}\left(\text{Sta. } S_{\text{Space}(a)}\right)\right) \times 0.25\right],$$

$$\text{Min}\left(\text{Poss. } S_{\text{Space}(a)}\right) = \text{Min}\left(\text{Est. } S_{\text{Space}(a)}\right) + \left[\left(\text{Max}\left(\text{Est. } S_{\text{Space}(a)}\right) - \text{Min}\left(\text{Sta. } S_{\text{Space}(a)}\right)\right) \times 0.25\right].$$

$$(3)$$

In this formula, the maximum possible area of each space (Sta. $S_{\text{Space}(a)}$) is 90 square meters based on the minimum maximum estimated area of that space (Sta. $S_{\text{Space}(a)}$) and the minimum standard area of that space (Sta. $S_{\text{Space}(a)}$) will be obtained. Based on this and based on the minimum standard length and width of residential spaces, all the length and width states of each space can be obtained. The findings are as follows (Table 5):

Considering that the variety of answers obtained is very high, the range of changes is divided into two parts to make its calculation easier. By obtaining the different states of length and width of different residential spaces, the different states of all residential spaces are drawn on the zero-zero coordinate axis. In the next step, it is necessary that all the spaces formed for each layout are placed together based on the criteria desired by the designer. This concept should be converted into parameters that can be recognized by the algorithm. Therefore, in order to determine and define the spaces adjacent to each other in the plan, the proximity matrix of the spaces has been determined, and then through the Delphi method and by an open questionnaire and interview, its validity has been confirmed by experts. The final results of this matrix, which is mentioned as follows, show what spaces need to be together and in direct communication according to experts in the field of housing (Table 6).

The process of placing spaces together continues until all spaces are placed together. After placing all the spaces next to each other, the overall shape needs to be close to a rectangle. For this purpose, at the end of the placement process, the set of spaces are enclosed in the smallest possible rectangle. Between the rectangle and the set of spaces, there remains a range of empty spaces. According to a set of Python code, the spaces between are reduced. In each spatial placement, a set of empty spaces remains empty between the residential spaces as well. For these spaces, a range is considered, and if their area is less than a certain value, it will be added to the space that has the most in common with it. And if it was more than the specified value, it should be deleted (see Table 7).

Based on this, with the addition of empty spaces in between, some spaces have become larger than the maximum possible area and have increased to about the maximum estimated area. Finally, a set of results of 440 plans has been obtained, and the variation of the area of the obtained spaces is mentioned in the table. Some examples of the final configuration results are provided in line (Figure 1).

As a result of the algorithm process, two outputs are generated: a visual layout of residential spaces and linear segmentation and geometric evaluation data for each answer. The output of this algorithm can be used in a variety of optimization cycles based on different performance objectives. In addition, the output of the algorithm can be easily transformed into the final form of architecture by placing it in a modeling process.

3.2. Statistical Findings and Data Analysis. As mentioned, the produced plans have been subject to statistical tests for evaluation. For this purpose, the data of 440 obtained plans, including the length, width, and area of each space; the

TABLE 4: Standard and estimated dimensions of residential spaces (source: author).

	Entrance	Kitchen	Living room	Parents' bedroom	Child's bedroom	W. C and bathroom
Minimum standard area	2.5	5.8	15	12	7.2	1.45
Maximum estimated area	3.5	25	50	25	17	4

TABLE 5: Standard and possible dimensions of residential spaces (source: author).

	Entrance	Kitchen	Living room	Parents' bedroom	Child's bedroom	W. C and bathroom
Minimum possible area	2.75	23.57	24.12	14.7	8.11	1.75
Maximum possible area	3.25	7.67	48.9	24.03	16.67	3.91
The shortest possible side length	1.5	2.55	3.94	2.98	2.72	1.18
The longest possible side length	1.9	4.92	6.99	5.2	4.2	2.04

TABLE 6: The proximity matrix of spaces (source: author).

	Entrance	Kitchen	Living room	Parents' bedroom	Child's bedroom	W. C and bathroom
Entrance	1	—	1	—	—	—
Kitchen	—	1	1	—	—	—
Living	1	1	1	1	1	1
Parents' bedroom	—	—	1	1	—	1
Child's bedroom	—	—	1	—	1	1
W. C and bathroom	—	—	1	1	1	1

TABLE 7: The scope of the final area of produced residential spaces (source: author).

	Entrance	Kitchen	Living room	Parents' bedroom	Child's bedroom	W. C and bathroom
Minimum resulting area	2.28	6.8	22.18	11.36	7.93	1.69
Maximum resulting area	3.5	22.35	25	17	17	4
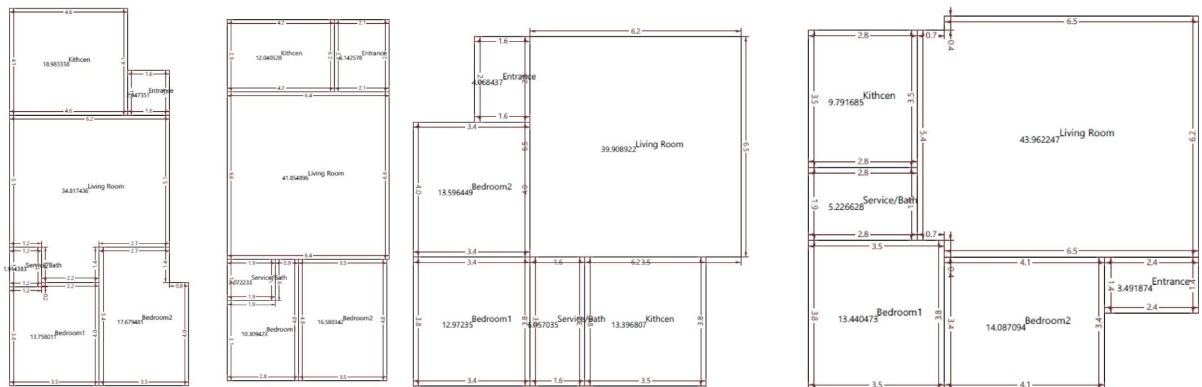
FIGURE 1: The example of the final answers of the linear configuration of the algorithm (source: the author).

perimeter of the final plan; and the length, width, and area of the rectangle surrounded by the final plan, have been collected. These data were entered into SPSS software and subjected to correlation and regression tests.

First, the correlation between the area of all internal spaces and the four perimeteral variables of the final plan and the length, width, and area of the rectangle surrounded by the final plan has been performed. In this test, the significance coefficient of most of the correlations is less than 0.05. Only in four tests, a significance coefficient higher than 0.05 has been reported. According to Amrhein's opinion [25], the value of the significance coefficient does not necessarily indicate whether the data is meaningful or not, and it is only a report that can help this.

In this test, the highest correlation is between the width and length of the peripheral rectangle. Also, after that, the relationship between the area of the peripheral rectangle and fthe perimeter of the final plan has the highest correlation.

Among residential spaces, the perimeter of the final plan has the highest correlation with the reception area and the lowest correlation with the area of the child's bedroom. The correlation of the plan perimeter with the reception area, the service and bathroom area, and the entrance area is negative and positive with other variables (Table 8).

Also, the highest correlation of the width of the peripheral rectangle is with the W. C and bathroom area, and the lowest correlation is with the reception area. The correlation between the width of the peripheral rectangle and the area of the parents' bedroom, the area of the kitchen, the entrance area, and the length of the peripheral rectangle is negative. In other cases, the correlation is positive. Regarding the length of the peripheral rectangle, the highest correlation is related to the area of W. C and bathroom and the lowest correlation is related to the area of the child's bedroom. Regarding this variable, the area of the child's bedroom, the area of W. C and bathroom, the living area, the area of the entrance, and the width of the peripheral rectangle have a negative correlation with the length of the peripheral rectangle. Also, regarding the correlation of the area of the peripheral rectangle with the area of residential spaces, the highest correlation is related to the area of the child's bedroom and the lowest is related to the area of W. C and bathroom (Table 9).

In the following, the correlation test between the length and width of all internal spaces and the four perimeter variables of the final plan and the length, width, and area of the rectangle surrounded by the final plan has been performed. In this test, the significance coefficient of most of the correlations is less than 0.05, and only in six tests, the significance coefficient is higher than 0.05, which according to Amrhein et al. 2019, shows that it does not matter whether the data are meaningful or not. Regarding the correlation test of the entire plan perimeter with the width and length of residential interior spaces, the width of living has the highest correlation. This is a negative correlation, which indicates an inverse relationship. The lowest correlation in this section is related to the width of the toilet and bathroom. This correlation is also negative. Also, among the correlations of the width of the rectangle surrounded by residential spaces, the highest correlation is related to the child's bedroom and the lowest correlation is related to the parents' bedroom (see Table 10).

In the following, the linear regression test has been performed targeting the perimeter of the plan and the area of the rectangle surrounded by the plan as the dependent variable. First, linear regression has been tested in relation to the areas of internal spaces and the area of the peripheral rectangle (see Table 11).

In the ANOVA test, the significance of the regression test is confirmed regarding the area of the interior spaces and the area of the peripheral rectangle. Based on the results of the test, the areas of the interior spaces predict only 34% of the changes in the area of the peripheral rectangle (Table 12).

The significance coefficient of the three variables of child's bedroom area, parent's bedroom area, and the entrance area is less than 0.05 and is reported to be significant. Other variables were not reported as significant. In the

regression test, based on the standardized coefficients, the largest contribution is related to the area of the child's bedroom. After that, the entrance area is the most influential variable in the relationship, which has a negative effect. The living area variable is also reported as a variable excluded from the test. The area variable has been tested individually, which predicts only 16% of the changes in the area of the peripheral rectangle. The living area with a standardized coefficient of −0.406 has a significant effect on the area of the peripheral rectangle (see Table 13).

In the following, linear regression has been tested in relation to the areas of internal spaces and the perimeter of the overall plan. Based on the ANOVA test, the significance of the linear regression is confirmed (see Table 14).

Based on the test results, the areas of the interior spaces predict 25% of the perimeter changes of the final plan. In this test, the living area is reported as a variable excluded from the test (Table 14).

The significance coefficient of all independent variables is less than 0.05, and it is reported as significant. The highest standard coefficient of the regression test is related to the area of the kitchen. The lowest amount is related to the area of WC and bathroom (Table 15). The living area variable has been tested separately. The regression coefficient of the reception area is reported as 0.441 (see Table 16).

In the following, linear regression has been tested in the relationship between the length and width of the interior spaces and the area of the peripheral rectangle. Based on the ANOVA test, the significance of the linear regression is confirmed (Table 17).

Based on the test results, the length and width of the interior spaces predicts 54% of the changes in the area of the peripheral rectangle. This shows that the width and length of residential spaces make a better prediction of the area of the peripheral rectangle than the area of residential spaces. The significance coefficient of all independent variables, except the width of the living room, the width and length of the kitchen, and the fixed value, is less than 0.05 and is reported to be significant (Table 18).

The highest standard coefficient of the regression test is related to the width of the parents' bedroom. The lowest amount is related to the living width (Table 19).

In the following, linear regression has been tested in relation to the length and width of the interior spaces and the perimeter of the overall plan. Based on the ANOVA test, the significance of the linear regression is confirmed (Table 20).

Based on the test results, the length and width of the interior spaces predicts 35% of the overall plan perimeter changes. This shows that the width and length of residential spaces make a better prediction of the perimeter of the final plan than the area of residential spaces. The coefficient of significance of width and length of reception, length of W. C and the bathroom, and length of entrance is less than 0.05, and it is reported as significant (Table 21).

The highest standard coefficient of the regression test is related to the living width. The lowest amount is related to the width of WC and the bathroom. Based on the regression tests, the linear models of the perimeter of the final plan and the area of the perimeter rectangle based on

TABLE 8: Correlation between the area of all interior spaces and four variables of the final plan (source: author).

		The area of the child's bedroom	The area of the parents' bedroom	W. C area and bathroom	Living area	Kitchen area	Entrance area	The entire perimeter of the plan	Width of the peripheral rectangle	Length of the peripheral rectangle	Area of the peripheral rectangle
Perimeter of whole plan	Pearson correlation	0.262**	0.344**	−0.168**	−0.441**	0.395**	−0.280**	1	0.004	0.433**	0.597**
	Sig. (2-tailed)	0.000	0.000	0.000	0.000	0.000	0.000		0.932	0.000	0.000
	N	440	440	440	440	440	440	440	440	440	440
Width peripheral rectangle	Pearson correlation	0.287**	−0.175**	0.328**	0.097*	−0.173**	−0.176**	0.004	1	−0.795**	0.556**
	Sig. (2-tailed)	0.000	0.000	0.000	0.041	0.000	0.000	0.932		0.000	0.000
	N	440	440	440	440	440	440	440	440	440	440
Length peripheral rectangle	Pearson correlation	−0.041	0.429**	−0.440**	−0.383**	0.395**	−0.125**	0.433**	−0.795**	1	0.058
	Sig. (2-tailed)	0.387	0.000	0.000	0.000	0.000	0.009	0.000	0.000		0.228
	N	440	440	440	440	440	440	440	440	440	440
Area peripheral rectangle	Pearson correlation	0.455**	0.354**	−0.064	−0.406**	0.248**	−0.413**	0.597**	0.556**	0.058	1
	Sig. (2-tailed)	0.000	0.000	0.181	0.000	0.000	0.000	0.000	0.000	0.228	
	N	440	440	440	440	440	440	440	440	440	440

**correlation is significant at the 0.01 level (2-tailed). *correlation is significant at the 0.05 level (2-tailed).

TABLE 9: Correlation between length and width of all interior spaces and four final plan variables (source: author).

		The width of the child's bedroom	The length of the child's bedroom	The width of the parents' bedroom	The length of the parents' bedroom	W. C and bathroom width	Length of W. C and bathroom	Living width	Living length	The width of the kitchen	The length of the kitchen	The width of the entrance	The length of the entrance
Perimeter of the whole plan	Pearson correlation	0.214**	0.291**	0.337**	0.255**	−0.057	−0.196**	−0.520**	−0.132**	0.372**	0.358**	−0.242**	−0.278**
	Sig. (2-tailed)	0.000	0.000	0.000	0.000	0.231	0.000	0.000	0.005	0.000	0.000	0.000	0.000
	N	440	440	440	440	440	440	440	440	440	440	440	440
Width peripheral rectangle	Pearson correlation	0.350**	−0.145**	−0.087	−0.348**	0.289**	0.282**	0.109*	−0.077	−0.092	−0.131**	−0.148**	−0.145**
	Sig. (2-tailed)	0.000	0.002	0.067	0.000	0.000	0.000	0.022	0.105	0.053	0.006	0.002	0.002
	N	440	440	440	440	440	440	440	440	440	440	440	440
Length peripheral rectangle	Pearson correlation	−0.120*	0.344**	0.349**	0.503**	−0.284**	−0.437**	−0.448**	0.023	0.310**	0.365**	−0.101*	−0.153**
	Sig. (2-tailed)	0.012	0.000	0.000	0.000	0.000	0.000	0.000	0.629	0.000	0.000	0.033	0.001
	N	440	440	440	440	440	440	440	440	440	440	440	440
Area peripheral rectangle	Pearson correlation	0.447**	0.267**	0.397**	0.148**	0.090	−0.138**	−0.465**	−0.146**	0.264**	0.275**	−0.343**	−0.407**
	Sig. (2-tailed)	0.000	0.000	0.000	0.002	0.060	0.004	0.000	0.002	0.000	0.000	0.000	0.000
	N	440	440	440	440	440	440	440	440	440	440	440	440

**correlation is significant at the 0.01 level (2-tailed). *correlation is significant at the 0.05 level (2-tailed).

TABLE 10: Regression of the relationship between the areas of internal spaces and the area of the peripheral rectangle (source: the author).

Model	R	R square	Adjusted R square	Std. error of the estimate
1	0.588[a]	0.345	0.338	9.10820

a. Predictors: (constant), entrance area, WC and bathroom area, parent's bedroom area, kitchen area, and child's bedroom area.

TABLE 11: The ANOVA test regarding the area of internal spaces and the area of the peripheral rectangle (source: author).

Model		Sum of squares	df	Mean square	F	Sig.
	Regression	18981.548	5	3796.310	45.761	0.000[b]
1	Residual	36004.354	434	82.959		
	Total	54985.902	439			

a. Dependent variable: area of the peripheral rectangle. b. Predictors: (constant), entrance area, WC and bathroom area, parent's bedroom area, kitchen area, and child's bedroom area.

TABLE 12: Regression results of the relationship between the areas of internal spaces and the area of the peripheral rectangle (source: author).

Model		Unstandardized coefficients		Standardized coefficients	t	Sig.
		B	Std. error	Beta		
	(Constant)	96.647	4.240		22.796	0.000
	The area of the child's bedroom	1.652	0.239	0.341	6.902	0.000
1	The area of the parents' bedroom	0.312	0.147	0.107	2.127	0.034
	WC and bathroom area	−0.674	0.508	−0.052	−1.326	0.185
	Kitchen area	0.145	0.112	0.059	1.295	0.196
	Entrance area	−3.130	0.428	−0.324	−7.307	0.000

a. Dependent variable: area of the peripheral rectangle.

TABLE 13: Regression of the relationship between the areas of internal spaces and the perimeter of the overall plan (source: author).

Model	R	R square	Adjusted R square	Std. error of the estimate
2	0.509[a]	0.259	0.250	3.55739

a. Predictors: (constant), entrance area, W. C and bathroom area, parent's bedroom area, kitchen area, and child's bedroom area.

TABLE 14: The ANOVA test regarding the area of internal spaces and the environment of the general plan (source: author).

Model		Sum of squares	df	Mean square	F	Sig.
	Regression	1917.787	5	383.557	30.309	0.000[b]
2	Residual	5492.274	434	12.655		
	Total	7410.061	439			

a. Dependent variable: perimeter of whole plan. b. Predictors: (constant), entrance area, W. C and bathroom area, parent's bedroom area, kitchen area, and child's bedroom area.

TABLE 15: Regression of the relationship between the areas of internal spaces and the perimeter of the general plan (source: the author).

Model		Unstandardized coefficients		Standardized coefficients	t	Sig.
		B	Std. error	Beta		
	(Constant)	37.687	1.656		22.760	0.000
	The area of the child's bedroom	0.238	0.093	0.134	2.550	0.011
2	The area of the parents' bedroom	0.187	0.057	0.175	3.265	0.001
	Area of W. C and bathroom	−0.550	0.199	−0.116	−2.771	0.006
	Kitchen area	0.249	0.044	0.278	5.708	0.000
	Entrance area	−0.427	0.167	−0.120	−2.554	0.011

a. Dependent variable: perimeter of whole plan.

TABLE 16: Regression of the relationship between the length and width of the interior spaces and the area of the peripheral rectangle (source: the author).

Model	R	R square	Adjusted R square	Std. error of the estimate
3	0.744[a]	0.553	0.540	7.58759

a. Predictors: (constant), entrance length, WC and bathroom width, parents' bedroom width, child's bedroom width, kitchen width, service and bathroom length, entrance width, parents' bedroom length, living room length, child's bedroom length, kitchen length, and living room width.

TABLE 17: The ANOVA test on the relationship between the length and width of the interior spaces and the perimeter of the overall plan (source: author).

	Model	Sum of squares	df	Mean square	F	Sig.
	Regression	30402.880	12	2533.573	44.007	0.000[b]
3	Residual	24583.022	427	57.571		
	Total	54985.902	439			

a. Dependent variable: area of the peripheral rectangle. b. Predictors: (constant), entrance length, WC and bathroom width, parents' bedroom width, child's bedroom width, kitchen width, service and bathroom length, entrance width, parents' bedroom length, living room length, child's bedroom length, kitchen length, and living room width.

TABLE 18: Regression of the relationship between the length and width of the interior spaces and the area of the peripheral rectangle on the overall plan (source: author).

	Model	Unstandardized coefficients		Standardized coefficients	t	Sig.
		B	Beta	Beta		
	(Constant)	8.431	40.155		0.210	0.834
	The width of the child's bedroom	12.310	1.643	0.385	7.490	0.000
	The length of the child's bedroom	4.224	1.726	0.177	2.448	0.015
	The width of the parents' bedroom	11.377	1.587	0.535	7.168	0.000
	The length of the parents' bedroom	−8.445	1.019	−0.411	−8.289	0.000
	W. C and bathroom width	5.971	1.906	0.119	3.132	0.002
3	Length of WC and bathroom	−3.712	1.189	−0.132	−3.123	0.002
	Living width	0.029	1.549	0.002	0.019	0.985
	Living length	6.544	1.379	0.352	4.745	0.000
	The width of the kitchen	2.736	1.736	0.172	1.576	0.116
	The length of the kitchen	1.529	1.452	0.075	1.052	0.293
	The entrance width	−4.907	1.905	−0.112	−2.575	0.010
	The length of the entrance	−7.252	1.379	−0.248	−5.259	0.000

a. Dependent variable: area of the peripheral rectangle.

TABLE 19: Regression of the relationship between the length and width of the interior spaces and the perimeter of the general plan (source: the author).

Model	R	R square	Adjusted R square	Std. error of the estimate
4	0.603[a]	0.364	0.346	3.32239

a. Predictors: (constant), length of entrance, width of service and bathroom, width of parents' bedroom, width of child's bedroom, width of kitchen, length of service and bathroom, width of entrance, length of parents' bedroom, length of living room, length of child's bedroom, length of kitchen, and width of living.

the length and width of the internal spaces are generally more appropriate than the area of the internal spaces. This leads to the following model for predicting the area of the perimeter rectangle of the final plan. This model can predict with 95% confidence about 54% of environmental areas:

TABLE 20: The ANOVA test on the relationship between the length and width of the interior spaces and the perimeter of the general plan (source: the author).

	Model	Sum of squares	df	Mean square	F	Sig.
	Regression	2696.710	12	224.726	20.359	0.000[b]
4	Residual	4713.351	427	11.038		
	Total	7410.061	439			

a. Dependent variable: perimeter of the whole plan. b. Predictors: (constant), length of entrance, width of service and bathroom, width of parents' bedroom, width of child's bedroom, width of kitchen, length of WC and bathroom, width of entrance, length of parents' bedroom, length of living room, length of child's bedroom, length of kitchen, and width of living room.

TABLE 21: Regression of the relationship between the length and width of the interior spaces and the perimeter of the general plan (source: the author).

	Model	Unstandardized coefficients		Standardized coefficients	t	Sig.
		B	Beta	Beta		
	(Constant)	41.469	17.583		2.358	0.019
	The width of the child's bedroom	0.956	0.720	0.081	1.328	0.185
	The length of the child's bedroom	0.753	0.756	0.086	0.997	0.320
	The width of the parents' bedroom	0.898	0.695	0.115	1.292	0.197
	The length of the parents' bedroom	−0.817	0.446	−0.108	−1.831	0.068
	W. C and bathroom width	0.015	0.835	0.001	0.019	0.985
4	Length of W. C and bathroom	−1.321	0.520	−0.128	−2.538	0.012
	Living width	−2.003	0.678	−0.411	−2.953	0.003
	Living length	1.836	0.604	0.269	3.040	0.003
	The width of the kitchen	1.063	0.760	0.182	1.398	0.163
	The length of the kitchen	−0.147	0.636	−0.020	−0.232	0.817
	Entrance width	−1.243	0.834	−0.077	−1.489	0.137
	Entrance length	−1.071	0.604	−0.100	−1.774	0.077

a. Dependent variable: perimeter of the whole plan.

$$
\begin{aligned}
A_{PR} = {} & 8.431 + (12.310 \times W_{SRR}) + (4.224 \times L_{SRR}) \\
& + (11.377 \times W_{MRR}) + (-8.445 \times L_{MRR}) \\
& + (5.971 \times W_{W\&B}) + (-3.712 \times L_{W\&B}) \\
& + (0.029 \times W_{LR}) + (6.544 \times L_{LR}) + (2.736 \times W_{KR}) \\
& + (1.529 \times L_{KR}) + (-4.907 \times W_{ES}) + (-7.252 \times L_{ES}).
\end{aligned}
\tag{4}
$$

$$
\begin{aligned}
P_{FP} = {} & 41.469 + (0.956 \times W_{SRR}) + (0.753 \times L_{SRR}) \\
& + (0.898 \times W_{MRR}) + (-0.817 \times L_{MRR}) \\
& + (0.015 \times W_{W\&B}) + (-1.321 \times L_{W\&B}) \\
& + (-2.003 \times W_{LR}) + (1.836 \times L_{LR}) + (1.063 \times W_{KR}) \\
& + (-0.147 \times L_{KR}) + (-1.243 \times W_{ES}) + (-1.071 \times L_{ES}).
\end{aligned}
\tag{5}
$$

In addition, the prediction model for the final plan is presented as follows; it can predict with 95% confidence about 35% of the responses to the plan environment:

In these two models,

The length of the reception room	L_{LR}	The width of the second bedroom	W_{SRR}	
The width of the kitchen	W_{KR}	The length of the second bedroom	L_{SRR}	
The length of the kitchen	L_{KR}	The width of the master bedroom	W_{MRR}	
The width of the entrance space	W_{ES}	The length of the master bedroom	L_{MRR}	$\cdot$ (6)
The length of the entrance space	L_{ES}	The width of the toilet and bathroom	$W_{W\&B}$	
The area of the peripheral rectangle	A_{PR}	The length of the toilet and bathroom	$L_{W\&B}$	
The environment of the final plan	P_{FP}	The width of the reception room	W_{LR}	

According to the amount of *R*-Score (*R*-Square), obtained in two models, other parameters, such as the contiguous spaces, play a colorful role in defining the perimeter of a plan and the area of its surrounding rectangle. One of the limitations of this research is that these variables cannot be converted into numerical form for inclusion in the model.

4. Discussion

This paper presents a creative area-oriented approach to generative housing layout design that automatically generates plans for a single unit. Compared to similar studies [18–20], the existing algorithm includes a comprehensive range of design variables for the configuration of residential spaces. Since the simulation of the energy performance of the building was not considered, unlike some researches [16, 22], the three-dimensional variables of the form were not taken into account in the algorithm and the two-dimensional responses sufficed. In comparison to similar studies using an area-oriented approach [17, 19, 21], the final answers of the algorithm possess the necessary performance standards and a desirable variety. The final results of the configuration are all with an area of 90 square meters, and all of them have all the desired residential spaces in compliance with the rules and standards compiled in the algorithm. Based on the findings of the study and the opinions of other researchers [13, 18, 22], the generative design mechanism of housing configuration can be used as a designer's assistant in providing a variety of layouts in accordance with design standards and based on the area. Additionally, the outputs of the algorithm, compared to research with the energy performance optimization approach [16, 22], indicate that the algorithm can be integrated into the functional computing design cycle.

In the research, 440 production configuration samples were examined using the productive design method to determine four general configuration forms, including incomplete squares, rectangles with one-to-two ratios, incomplete rectangles with one-to-two ratios, and incomplete L-shapes. It shows a more practical layout compared to other studies [17, 22] due to the limitation of the plan to two x and y axes and an area of 90 square meters. Additionally, the general structure of the answers indicates that private and public spaces are well separated. The entrance space is always located at the corner of the plan. Due to the proximity relations formulated in the proximity matrix, this issue arises. It is possible to increase the variety of responses by changing the proximity structure of the input space. There is an optimal fit between the spaces of the residential unit and the reception area in all cases, which occupies approximately half of the area of the unit (Figure 2).

In the meantime, the lack of an intermediate space between private and public spaces is clearly felt. This intermediate space can solve the problem of privacy well by defining its direct relationship with two bedrooms and the living room. It also improves the spatial circulation of the residential unit.

Different parts of the algorithm have been found to have limitations. Among them, we can highlight the difficulty of creating indoor spaces other than rectangles in a controlled manner, as shown in other studies using area-based approaches [5, 16, 21]. The spaces are defined by two numbers: the dimensions of the space and the coordinates of one of its vertices. Occasionally, owing to the empty spaces in between, it may be possible to form a space in a form other than a rectangle; however, these responses are based on specific circumstances and are not preplanned. The algorithm also has the limitation of not being able to define the configuration based on a specific outer boundary, which has also been observed in other studies [17, 23]. By using this algorithm, the spaces are placed in proximity to one another by observing the proximity conditions one after another, with only the two x and y axes limiting their proximity. As a matter of fact, the configuration is composed of two limited plans and two unlimited sides. Compared to previous studies [5, 17, 21], this research has performed tests on the final geometric data of the spatial configuration.

Correlation results show that the width and length of the peripheral rectangle are connected. This issue shows that the proportions of the plan in the above four cases have been preserved in all plans. Also, the correlation results show that the area of the peripheral rectangle and the perimeter of the final plan are directly related. This shows that the general form of the plan was almost constant. The correlation results also show that the living area has the greatest effect on the perimeter of the final plan, and this effect is reversed. This issue may be due to the effect of the large dimensions of the living room and its placement in the space, which needs further investigation. Based on the results of the linear regression test, it can be understood that the width and length of the interior spaces are better variables for predicting the perimeter of the plan and the area of the peripheral rectangle. In the case of future researches, it is suggested to identify all the relationships and explain the nonlinear relationship of the variables by using curve regression.

One of the limitations of this research is that it is impossible to control the overall shape of the production configuration; however, in an innovative method, the perimeter rectangle was used and the ratio of the length to the width of the rectangle was tried to be reduced as much as possible. The present study has also introduced two relationships from two linear regression models in the area-oriented approach of automatic configuration generation, which can be conditionally placed in the path of the generating algorithm and control the plan form. To achieve a rectangular configuration, it is essential to establish the following relationship based on the two parameters of the environment and the area, along with the dimensions of the interior spaces:

$$\text{Area of Peripheral Rectangle} \cong \sum \text{Area of Interior Spaces.} \tag{7}$$

In accordance with the linear regression model obtained, the following model can be defined as the configuration of a residential unit of approximately 90 square meters. In this model, if α tends to zero, the configuration obtained is rectangular:
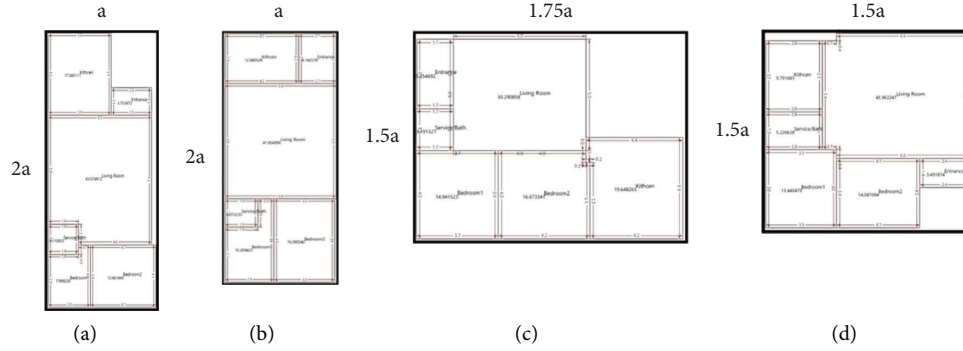
FIGURE 2: Variation of the final responses of the algorithm (source: author). (a) An incomplete rectangle. (b) A rectangle. (c) Incomplete L-shape. (d) An incomplete square.

$$
\begin{aligned}
\text{Area} + \alpha = {} & 8.431 + (12.310 \times W_{\text{SRR}}) + (4.224 \times L_{\text{SRR}}) \\
& + (11.377 \times W_{\text{MRR}}) + (-8.445 \times L_{\text{MRR}}) \\
& + (5.971 \times W_{W\&B}) + (-3.712 \times L_{W\&B}) \\
& + (0.029 \times W_{\text{LR}}) + (6.544 \times L_{\text{LR}}) \\
& + (2.736 \times W_{\text{KR}}) + (1.529 \times L_{\text{KR}}) \\
& + (-4.907 \times W_{\text{ES}}) + (-7.252 \times L_{\text{ES}}).
\end{aligned}
\tag{8}
$$

Also, if the two axes x and y are defined for each production configuration, it can be acknowledged that one of the following relations must be established to reach the shape of the rectangular configuration:

$$
4 \times \text{Area} \cong \sum x \text{ sides} \times \sum y \text{ sides}. \tag{9}
$$

This formula alone can be defined as a condition in the algorithm. It is also possible to reach the following formula by expanding this formula:

$$
\sum x \text{ sides} + \frac{4 \times \text{Area}}{\sum x \text{ sides}} \cong \text{Primeterof Generated Layout}. \tag{10}
$$

Based on the linear regression model obtained, the following model can be defined as the configuration of an approximately 90 square meter residential unit. In this model, if β tends toward zero, the configuration obtained is rectangular:

$$
\begin{aligned}
\sum & x \text{ sides} + \frac{4 \times \text{Area}}{\sum x \text{ sides}} - 41.469 + \beta \cong (0.956 \times W_{\text{SRR}}) \\
& + (0.753 \times L_{\text{SRR}}) + (0.898 \times W_{\text{MRR}}) + (-0.817 \times L_{\text{MRR}}) \\
& + (0.015 \times W_{W\&B}) + (-1.321 \times L_{W\&B}) + (-2.003 \times W_{\text{LR}}) \\
& + (1.836 \times L_{\text{LR}}) + (1.063 \times W_{\text{KR}}) + (-0.147 \times L_{\text{KR}}) \\
& + (-1.243 \times W_{\text{ES}}) + (-1.071 \times L_{\text{ES}}).
\end{aligned}
\tag{11}
$$

Area-oriented approaches to generative configuration design can take into account the above conditions. Considering that a similar model was not seen on the production results of the configuration in the investigated researches, it is suggested that in similar researches, the results obtained from the generative algorithm should be evaluated and modeled in order to be able to compare the results obtained. In future studies, it is also recommended to use the abovementioned conditions.

5. Conclusion

Presented in this research is an interactive generative spatial layout (GSL) design process that provides optimized spatial design solutions based on geometric, topological, and functional objectives and constraints as inputs. The shape of the final plans is also evaluated based on the two variables of the plan environment and its central rectangle. As a result of providing geometrical, topological, and functional constraints in all responses, the final results demonstrate clearly that the creative area-oriented approach to the productive design of housing configurations can serve as an assistant mechanism in providing a variety of layouts for the designer. By incorporating this algorithm into the optimization cycle for each functional goal, optimal design responses can be determined. With the existing algorithm, designers can directly obtain and use a set of optimal responses along with a set of geometric and functional evaluations by determining the design objective and constraints.

The development of this algorithm can be divided into several phases in the future. One of the most important aspects of the development is the possibility of planning the spatial configuration based on determining the outer boundaries of the residential units. To reach optimal answers through single-objective or multiobjective optimization algorithms, the second part of the development of this algorithm is to place it in an optimization cycle that combines functional goals such as thermal performance, lighting requirements, and ventilation performance. Another objective of developing this algorithm is to place the residential units generated by the algorithm in apartments and on a larger scale in residential blocks such that their geometric variables are parametrically defined. Based on the results of this

process, the functional goals of the residential unit can be reviewed by taking into account the neighborhood's characteristics. Additionally, one of the other development processes of the current algorithm is the use of creative design limitations obtained through regression tests, which may lead to more practical results.

Data Availability

The data supporting the findings of the current study are available from the corresponding author upon request.

Conflicts of Interest

The authors declare that they do not have any conflicts of interest.

References

[1] United Nation Environment Programme (UNEP), *Is the Future Yours? Research Project on Youth and Sustainable Consumption*, United Nation Environment Programme (UNEP), Nairobi, Kenya, 2001.

[2] T. I. Hewitt, "Fields for the future," in *Forum for Applied Research and Public Policy*, vol. 13, no. 2, p 83, University of Tennessee, Energy, Environment and Resources Center, Knoxville, Tennessee, 1998.

[3] American Institute of Architects - East Tennessee, "Design to Construction," 2020, https://www.aiaetn.org/find-an-architect/design-to-construction/.

[4] E. Rodrigues, D. Sousa-Rodrigues, M. Teixeira de Sampayo, A. R. Gaspar, Á. Gomes, and C. Henggeler Antunes, "Clustering of architectural floor plans: A comparison of shape representations," *Automation in Construction*, vol. 80, pp. 48–65, 2017.

[5] J. Michalek, R. Choudhary, and P. Papalambros, "Architectural layout design optimization," *Engineering Optimization*, vol. 34, no. 5, pp. 461–484, 2002.

[6] M. Zawidzki and J. Szklarski, "Multi-objective optimization of the floor plan of a single story family house considering position and orientation," *Advances in Engineering Software*, vol. 141, Article ID 102766, 2020.

[7] P. H. Levin, "Use of graphs to decide the optimum layout of buildings," *Architect*, vol. 14, pp. 809–815, 1964.

[8] C. Sydora and E. Stroulia, "Rule-based compliance checking and generative design for building interiors using BIM," *Automation in Construction*, vol. 120, Article ID 103368, 2020.

[9] L. Wang, P. Janssen, and G. Ji, "SSIEA: a hybrid evolutionary algorithm for supporting conceptual architectural design," *Artificial Intelligence for Engineering Design, Analysis and Manufacturing*, vol. 34, no. 4, pp. 458–476, 2020.

[10] L. Yan-kai, "The application of artificial intelligence technology in architectural design—taking Xiaoku xkool as an example," *intelligence Build Smart City*, vol. 1, pp. 43–45, 2019, in Chinese.

[11] R. S. Liggett and W. J. Mitchell, "Optimal space planning in practice," *Computer-Aided Design*, vol. 13, no. 5, pp. 277–288, 1981.

[12] R. Sharpe, B. S. Marksjo, J. R. Mitchell, and J. R. Crawford, "An interactive model for the layout of buildings," *Applied Mathematical Modelling*, vol. 9, no. 3, pp. 207–214, 1985.

[13] H. Yi, "User-driven automation for optimal thermal-zone layout during space programming phases," *Architectural Science Review*, vol. 59, no. 4, pp. 279–306, 2016.

[14] B. Montreuil, "Requirements for representation of domain knowledge in intelligent environments for layout design," *Computer-Aided Design*, vol. 22, no. 2, pp. 97–108, 1990.

[15] B. Medjdoub and B. Yannou, "Separating topology and geometry in space planning," *Computer-Aided Design*, vol. 32, no. 1, pp. 39–61, 2000.

[16] E. Rodrigues, A. R. Gaspar, and Á. Gomes, "An evolutionary strategy enhanced with a local search technique for the space allocation problem in architecture, Part 1: methodology," *Computer-Aided Design*, vol. 45, no. 5, pp. 887–897, 2013.

[17] M. Keshavarzi and M. Rahmani-Asl, "Genfloor: interactive generative space layout system via encoded tree graphs," *Frontiers of Architectural Research*, vol. 10, no. 4, pp. 771–786, 2021.

[18] N. Nauata, S. Hosseini, K. H. Chang, H. Chu, C. Y. Cheng, and Y. Furukawa, "House-gan++: generative adversarial layout refinement network towards intelligent computational agent for professional architects," in *Proceedings of the IEEE/CVF Conference on Computer Vision and Pattern Recognition*, pp. 13632–13641, Nashville, TN, USA, June 2021.

[19] P. Veloso, G. Celani, and R. Scheeren, "From the generation of layouts to the production of construction documents: an application in the customization of apartment plans," *Automation in Construction*, vol. 96, pp. 224–235, 2018.

[20] S. Boonstra, K. van der Blom, H. Hofmeyer, M. T. Emmerich, J. van Schijndel, and P. de Wilde, "Toolbox for super-structured and super-structure free multi-disciplinary building spatial design optimisation," *Advanced Engineering Informatics*, vol. 36, pp. 86–100, 2018.

[21] L. Schwartz, M. Wei, W. Morrow et al., *Electricity End Uses, Energy Efficiency, and Distributed Energy Resources Baseline*, Lawrence Berkeley National Laboratory, Berkeley, CA, USA, 2017, https://escholarship.org/uc/item/0n32c92z.

[22] I. G. Dino and G. Üçoluk, "Multiobjective design optimization of building space layout, energy, and daylighting performance," *Journal of Computing in Civil Engineering*, vol. 31, no. 5, Article ID 04017025, 2017.

[23] H. A. Sleiman, S. Hempel, R. Traversari, and S. Bruinenberg, "An assisted workflow for the early design of nearly zero emission healthcare buildings," *Energies*, vol. 10, no. 7, p. 993, 2017.

[24] Z. Su and W. Yan, "A fast genetic algorithm for solving architectural design optimization problems," *Ai Edam*, vol. 29, no. 4, pp. 457–469, 2015.

[25] R. Baušys and I. Pankrašovaite, "Optimization of architectural layout by the improved genetic algorithm," *Journal of Civil Engineering and Management*, vol. 11, no. 1, pp. 13–21, 2005.

[26] L. Caldas, "Generation of energy-efficient architecture solutions applying GENE_ARCH: an evolution-based generative design system," *Advanced Engineering Informatics*, vol. 22, no. 1, pp. 59–70, 2008.

[27] M. Ghasemzadeh, *Dimensional Criteria and Design Considerations of Urban Residential Unit Spaces*, Road, Housing and Urban Development Research Center, Tehran, Iran, 2013.

[28] V. Amrhein, S. Greenland, and B. McShane, "Scientists rise up against statistical significance," *Nature*, vol. 567, no. 7748, pp. 305–307, 2019.

Research Article

Study on the Dynamic Response of Composite Box Girder Bridges with Corrugated Steel Webs

Ya-Na Mao,[1,2] Chi Ma [ID],[1] Shi-Zhong Liu,[1] and Li-Yuan Li[1]

[1]*College of Civil Engineering, Lanzhou Jiaotong University, Lanzhou 730070, China*
[2]*Gansu Road and Bridge Highway Investment Co Ltd, Lanzhou, Gansu 730030, China*

Correspondence should be addressed to Chi Ma; 308329771@qq.com

To more accurately consider the dynamic response of composite box girder bridges with corrugated steel webs under the effect of live loads, based on the theory of vehicle-bridge coupled vibration, a refined finite element model of vehicle-bridge coupled vibration analysis for composite box girders was established. The advanced dynamic response analysis of composite box girders with corrugated steel webs and traditional concrete box girders with 30 m single boxes and single cells, as well as with 50 m single boxes and multiple cells, was carried out. The research revealed that the natural vibration frequency of the composite box girder with corrugated steel webs is lower than that of the corresponding concrete box girder. When the bridge deck condition is poor, the dynamic impact coefficient of the composite box girder is much larger than that of the concrete box girder. When the bridge deck is in poor condition, the dynamic impact response is significantly enhanced, and the difference is significantly compared with that when the bridge deck is in good condition, which is greater than three times and even six times at the maximum. Both the difference in the vehicle model and the change in the vehicle speed influence the dynamic impact coefficient of the composite box girder.

1. Introduction

For a composite box girder bridge with corrugated steel webs, replacing a concrete web with a steel web in a composite box girder with corrugated steel webs can effectively reduce the weight of the structure, which will inevitably lead to an increase in the ratio of live load to dead load. Therefore, the dynamic response generated by the live load will become more obvious. Based on the energy variation principle, Zhang et al. [1] comprehensively considered the effects of shear lag, fold, shear deformation, and moment of inertia, derived the dynamic control differential equation and boundary conditions of the continuous composite box girder bridge with corrugated steel webs, and analysed the natural vibration characteristics of the continuous composite box girder bridge with corrugated steel webs in combination with model tests and finite element numerical simulations. Chen et al. [2] constructed a three-span prestressed concrete and continuous corrugated steel web test

beam and carried out a dynamic test on it. The authors also carried out a dynamic test on a real bridge and compared the test results of the test beam and the real bridge with the finite element results. Zheng et al. [3, 4] constructed two corresponding test beams, compared the dynamic characteristics of the two beams with a combination of model tests and finite element numerical simulations, and analysed the influence of external prestress and its parameter changes on the natural frequency of a continuous box girder with corrugated steel webs. Based on box girder vibration theory, Wang et al. [5] proposed a method to calculate the natural frequency of a new composite box girder with corrugated steel webs under the action of time-varying temperature, which considered the slip effect. The proposed method was verified by finite element simulation and model test beam actual measurement. Wei et al. [6, 7] obtained the formula of vertical fundamental frequency correction for a continuous composite box girder with variable section corrugated steel webs by model testing and ANSYS finite element simulation

analysis and obtained the partial and integral impact coefficients of the composite box girder with corrugated steel webs by establishing the coupling vibration equation of the vehicle and bridge with a simply supported composite box girder. The current Chinese General Specification for Highway Bridge and Culvert Design (JTG D60-2015) [8] provides a formula for the dynamic impact coefficient based on the natural vibration frequency of the bridge. From the analysis of the natural vibration frequency of corrugated steel webs, due to the impact of the shear deformation of steel webs, the natural vibration frequency of the composite box girder should be multiplied by the reduction coefficient a_{2n} in the primary beam result [9]. The calculation formula of the impact coefficient provided in the specification is based on the impact coefficient samples of more than 6,600 concrete bridges with 6 m–45 m spans and is obtained by using the method of mathematical statistics and appropriate correction. It is necessary to further verify whether the impact coefficient formula is suitable for composite box girders with corrugated steel webs. Although Chinese bridge codes do not clearly list influence factors such as the deck condition, vehicle type, and speed for the impact coefficient of a bridge, some analyses have indicated that these factors have a certain influence on the dynamic impact coefficient [10–12]. Thus, these factors need to be analysed to provide a reference for the dynamic load test evaluation of this type of bridge in service.

In summary, to more accurately consider the dynamic response of the composite box girder with corrugated steel webs under the effect of live load and to properly analyse corrugated steel webs composite box girders in service, the dynamic impact coefficient of this composite box girder should be investigated.

2. Estimation and Analysis of the Dynamic Impact Coefficient of the Composite Box Girder

2.1. Domestic Highway Bridge Code. The Chinese General Specification for Design of Highway Bridges and Culverts (JTG D60-2015) stipulates that based on the research results of road bridge reliability, the impact coefficient of bridge structures is calculated by structural base frequency. The formula for calculating the impact coefficient μ is presented as follows:

$$\mu = \begin{cases} 0.005, & f < 1.5Hz, \\ 0.1767\text{In } f - 0.0157, & 1.5Hz \leq f \leq 14Hz, \\ 0.45, & f > 14Hz. \end{cases} \quad (1)$$

In the formula, f refers to the fundamental frequency of a structure (Hz). The specification provides the frequency estimation formula for the following simply supported beam:

$$f = \frac{\pi}{2l^2} \sqrt{\frac{EI_c}{m_c}}, \quad (2)$$

where l is the calculated span of the structure; I_c is the moment of inertia of the midspan section of the structure; m_c is the mass per unit length at the middle span of the structure, namely, $m_c = G/g$; G is the gravity of the structure per linear metre at the midspan of the structure; and g is the acceleration of gravity.

By comparing formula (2) with the calculation expression of the fundamental frequency of the composite box girder with corrugated steel webs, we know that due to the shear deformation of the corrugated steel web, the natural frequency of the composite box girder in formula (2) needs to be multiplied by the reduction factor a_{2n}. The impact coefficient in the article interpretation code is based on the actual measurement results of the concrete box girder bridge and is obtained through mathematical statistical analysis. However, the applicability of the composite box girder bridge with corrugated steel webs should be further analysed.

The impact coefficient in the specification interpretation is based on the measured results of the concrete box girder bridge, which is derived from the statistical analysis, and the applicability of the composite box girder bridge with corrugated steel webs should be further analysed.

2.2. International Highway Bridge Code. The 2012 version of the AASHTO bridge design specification is described in terms of dynamic load tolerance (DLA), and its value depends on the limit state and component type. Presently, the impact coefficient used by the US Code for strength assessment of active bridges is determined according to the level of pavement roughness, and the dynamic impact coefficient of the limit assessment of active bridges is specified to be 0.33 [13, 14].

The impact coefficient defined in the Japanese JRA (1996 edition) Highway Bridge Design Code is also a function of the bridge span, but it distinguishes bridges of different material types. The expressions of impact coefficients corresponding to vehicle loads are the same, while there are obvious differences in lane loads [15].

The Canadian 1983 edition of the Highway Bridge Design Code stipulates that the calculation formula of the impact coefficient μ of a bridge is similar to the 2004 edition of the Chinese Highway Bridge Design Code; both are based on the first-order flexural natural vibration frequency f_1 of a bridge. The 1991 edition of the Canadian Highway Bridge Design Code introduced the relationship between the number of axles and the impact coefficient, with a similar relationship specified in the most recent edition of the code. The main difference is that the impact coefficient μ at the bridge joint is 0.5 [16, 17].

By summarizing the simplified calculation formulas of impact coefficients in design codes of highway bridges worldwide, we obtained the following findings: (1) each country's highway and bridge design codes have different requirements on automobile impact coefficients; (2) different codes define the impact coefficient as the expression of different bridge parameters, such as bridge span, bridge natural frequency, and vehicle or lane load type; and (3) the

national codes do not clearly indicate the type of dynamic response of the bridge corresponding to the impact coefficient, and the codes have limited influence factors for simplicity and utility.

2.3. Comparative Analysis of the Dynamic Response of the Composite Box Girder. Many international codes consider the impact of different types of bridges, especially steel bridges and concrete bridges, on dynamic impact. Chinese codes do not subdivide bridge types into steel bridges and concrete bridges. Presently, there is no specification that gives special consideration to the dynamic impact response of the special type of bridge with a corrugated steel web composite box girder. Consequently, composite box girder bridges with corrugated steel webs were analysed and compared with concrete box girder bridges, and samples of single box, single cell, and single box twin cell girders were selected for comparison.

2.3.1. Single Box, Single Cell Composite Box Girder with Corrugated Steel Webs. A section of a composite box girder with corrugated steel webs, as shown in Figure 1(a), is selected, and the span combination of a 1×30 m simply supported beam and a 2×30 m continuous box girder is employed. The elastic modulus of the flange plate is 34.5 GPa, and Poisson's ratio is 0.2. The elastic modulus of the steel is 206 GPa, and Poisson's ratio is 0.3. The characteristics of the steel web are shown in Figure 1(b). The steel web is replaced by a concrete web for comparison and analysis, and the cross-sectional parameters are shown in Figure 1(c). The concrete material properties are identical to the material properties of the corrugated steel web combination box.

The spatial finite element model of the abovementioned composite box girder with corrugated steel webs and concrete box girder was established using ANSYS spatial finite element software to calculate the natural frequency of the model. The natural frequencies of composite box girders with corrugated steel webs and concrete box girders were calculated by the general specification of highway bridges and culverts and the method of [12], respectively. The results are listed in Table 1.

2.3.2. Single Box, Twin Cell Composite Box Girder with Corrugated Steel Webs. A section of a composite box girder with corrugated steel webs, as shown in Figures 2 and 2(a), with a span of 1×50 m is selected. The material characteristics are the same as those of the single box, single-cell composite box girder mentioned above. The characteristics of the steel web are shown in Figure 2(b). The cross-sectional parameters of the concrete box girder used for comparison are shown in Figure 2(c). The box girder deflection, natural vibration frequency calculated by highway specification 89 is shown in Table 2.

By comparing the frequencies in Table 1, we obtained the following findings: (1) The analytical results in this article show agreement with the ANSYS solid finite element results. Tables 1 and 2 show that after the corrugated steel webs are

replaced with ordinary concrete webs, the difference between the calculated low-order frequencies is small. However, as the frequency order increases, the difference between the two frequency values increases, and the frequency of the composite box girder with corrugated steel webs is lower than that of the concrete box beams.

The provisions of the domestic and international codes for the dynamic impact coefficient of bridges are mostly calculated based on the span or frequency, with the exception of distinguishing the material type. Based on an analysis of the natural frequency of corrugated steel webs and the corresponding concrete box girder, the dynamic impact coefficient of composite box girder bridges with corrugated steel webs is calculated according to domestic and international specifications, as shown in Table 3.

As shown in Table 3, according to the different impact coefficients calculated by the domestic and international codes, the Canadian code has the largest value, the Chinese 89 edition code has the smallest value, and the Chinese code, 15th edition, is relatively similar to the American and Japanese codes. In addition, note that the Chinese code, 15th edition, gives frequency estimation formulas for simply supported and continuous beams. The impact coefficient of a 30 m span, simply supported beam calculated according to the relevant formula is 0.257, the impact coefficient of the midsection of the continuous beam span is 0.314, and the impact coefficient of the fulcrum is 0.412.

3. Numerical Simulation of the Dynamic Response of the Composite Box Girder

According to the frequency of the composite box girder with corrugated steel webs and the corresponding concrete box girder and the specifications on the dynamic impact coefficient, when the span and frequency are equivalent, the dynamic impact coefficients of the composite box girder with corrugated steel webs and the concrete box girder are similar. However, the actual situation needs further comparison and analysis. The dynamic test of a bridge is relatively difficult to implement due to factors such as the external environment, the use of the bridge, and costs. Presently, with the rapid development of computer simulation and extensive theoretical research on vehicle-bridge coupling analysis, vibration and shock analysis of bridges can be achieved by numerical simulation.

3.1. Numerical Simulation of Cars. According to relevant research and the provisions of the aforementioned US and Canadian codes, the parameters of vehicles, such as their types, axles, axle load, and vehicle fundamental frequency, have different impacts on the dynamic impact coefficient of bridges. The selected vehicles are the two- and three-axis vehicle models commonly employed by scholars worldwide to analyse the coupling vibration of the axle [1, 2].

3.2. Pavement Smoothness Simulation. Pavement smoothness is an important source of excitation in vehicle-bridge coupled vibration analysis, and it has a large randomness.
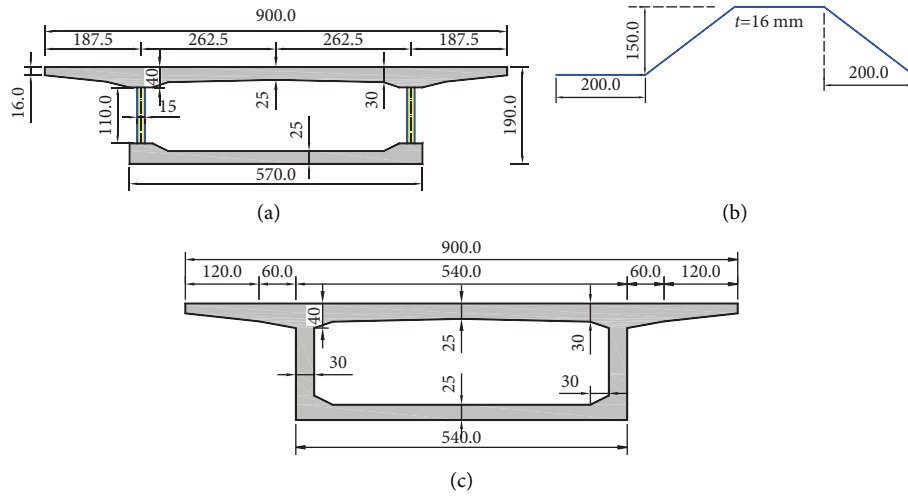
Figure 1: Cross-sectional diagram of the box girder: (a) section of the composite box girder with corrugated steel webs (cm), (b) detail of the corrugated steel web (mm), and (c) reinforced concrete box girder section (cm).

Table 1: Box beam natural frequencies calculated by different methods (unit: Hz).

Frequency order	Calculation method	Simply supported beam		2-Span continuous beam	
		Composite box girder	Concrete box girder	Composite box girder	Concrete box girder
1	Analytical method	4.452	4.479	4.452	4.479
	ANSYS entity	4.396	4.397	4.484	4.491
2	Analytical method	14.637	15.899	6.305	6.506
	ANSYS entity	13.217	14.453	6.087	6.569
3	Analytical method	24.099	30.763	14.637	15.899
	ANSYS entity	20.204	22.075	13.513	14.883
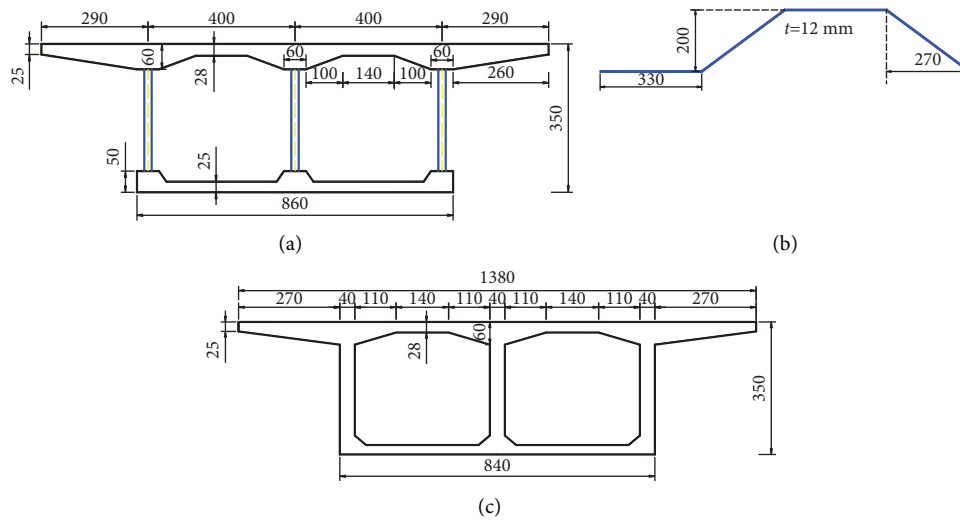
Figure 2: Schematic of the box girder section: (a) section of the composite box girder with corrugated steel webs (cm), (b) detail of the corrugated steel web (mm), and (c) reinforced concrete box girder section (cm).

When numerically simulating pavement smoothness, the method of series is usually applied to generate the pavement flatness curve that meets the power spectrum function. The formula of the power spectral density function of pavement smoothness is as follows [18]:

$$\varphi(n) = \varphi(n_0)\left(\frac{n}{n_0}\right)^{-2}, \ (n_1 < n < n_2), \tag{3}$$

where $\varphi(n_0)$ is the road surface smoothness coefficient corresponding to the standard spatial frequency; n and n_0 are

TABLE 2: Comparison of the natural frequency of the 50 m box girder (unit: Hz).

Frequency order	Composite box girder with corrugated steel webs	Concrete box girder
1	2.975	2.971
2	9.464	11.079
3	18.785	22.583

the spatial frequency and standard spatial frequency, respectively; and n_1 and n_2 are the indices of the road power spectrum in the low frequency band and high frequency band, respectively.

The formula for generating the road surface flatness curve by the series method is as follows:

$$r(x) = \sum_{k=1}^{N} \sqrt{2\varphi(n_k)\Delta n} \cos(2\pi n_k x + \theta_k),\qquad(4)$$

where x is the coordinate along the bridge axis; n_k, Δn, and N are the spatial frequency sampling point, sampling interval, and sampling number, respectively; and θ_k is the random phase angle in the interval $(0, 2\pi)$.

The road surface roughness is divided into five levels according to the International Organization for Standardization: very good, good, normal, poor, and very poor [19]. As the road surface smoothness curve generated according to the series method has large randomness, it masks the essential law of the dynamic impact coefficient. The solution is to use multiple road roughnesses for vehicle-bridge coupling vibration calculations to obtain multiple dynamic response values of the bridge structure, and then to calculate the average value to reduce the randomness of pavement flatness.

3.3. Solution of Vehicle-Bridge Coupling Vibration Equation. There have been many relevant theoretical studies on the dynamic coupling vibration equation of vehicles and bridges [20–23]. According to the relevant research, the dynamic equations of the respective systems of vehicles and bridges are shown in the following equations:

$$\mathbf{M}_v\ddot{\mathbf{d}}_v + \mathbf{C}_v\dot{\mathbf{d}}_v + \mathbf{K}_v\mathbf{d}_v = \mathbf{F}_{vg}\mathbf{F}_{vr},\qquad(5)$$

$$\mathbf{M}_b\ddot{\mathbf{d}}_b + \mathbf{C}_b\dot{\mathbf{d}}_b + \mathbf{K}_b\mathbf{d}_b = \mathbf{F}_{br},\qquad(6)$$

where $\mathbf{M}$, $\mathbf{C}$, and $\mathbf{K}$ are the mass, damping, and stiffness matrices, respectively; d is the system displacement vector; subscripts v and b represent vehicles and bridges, respectively; $\mathbf{F}_{vg}$ is the equivalent node load sequence vector caused by a vehicle's own weight; and $\mathbf{F}_{vr}$ and $\mathbf{F}_{br}$ are the interaction forces between the bridge and the vehicle system.

According to the contact relationship between the wheel and the bridge deck and the contact force between them when a vehicle crosses the bridge, the relationship of formulas (5) and (6) is established, and the important expression of the axle-coupled vibration is formed as follows:

$$\begin{bmatrix} \mathbf{M}_b & \\ & \mathbf{M}_v \end{bmatrix}\begin{Bmatrix} \mathbf{d}_b \\ \mathbf{d}_v \end{Bmatrix} + \begin{bmatrix} \mathbf{C}_b + \mathbf{C}_{b-b} & \mathbf{C}_{b-v} \\ \mathbf{C}_{v-b} & \mathbf{C}_v \end{bmatrix}\begin{Bmatrix} \dot{\mathbf{d}}_b \\ \dot{\mathbf{d}}_v \end{Bmatrix} + \begin{bmatrix} \mathbf{K}_b + \mathbf{K}_{b-b} & \mathbf{K}_{b-v} \\ \mathbf{K}_{v-b} & \mathbf{K}_v \end{bmatrix}\begin{Bmatrix} \mathbf{d}_b \\ \mathbf{d}_v \end{Bmatrix} = \begin{Bmatrix} \mathbf{F}_{b-v} \\ \mathbf{F}_{v-r} + \mathbf{F}_{vg} \end{Bmatrix},\qquad(7)$$

where $\mathbf{C}_{b-b}$, $\mathbf{C}_{b-v}$, $\mathbf{C}_{v-b}$, $\mathbf{K}_{b-b}$, $\mathbf{K}_{b-v}$, $\mathbf{K}_{v-b}$, $\mathbf{F}_{b-r}$, and $\mathbf{F}_{v-r}$ are additional terms resulting from the axle-bridge coupling effect.

For the solution method of vehicle-bridge coupled vibration expression (7), the direct integration method or modal synthesis method is generally adopted [16]. Since this article will establish a spatial solid model of corrugated steel web composite box girders and the corresponding concrete box beams, there will be many nodes and elements. Thus, this article adopts the modal synthesis method, which effectively reduces the calculation workload for more complicated bridges and obtains a more accurate numerical solution. The specific simulation method is described as follows: first, ANSYS spatial finite element software is used to establish a solid finite element model of the composite box girder and the corresponding concrete box girder, to calculate its natural frequency and vibration mode, and to extract the corresponding modal matrix. Then, MATLAB software is used to compile the fourth-order Runge–Kutta method and import the modal matrix of the bridge to solve equation (7) to obtain the dynamic response of the bridge.

4. Analysis of the Dynamic Shock Response of the Composite Box Girder

To analyse the dynamic impact coefficient of the composite box girder, the above example is used, and the test section is the midspan section. The arrangement of measuring points on the composite box girder is shown in Figure 3, and the measuring points of the concrete box girder are the same as those of the composite box girder. To verify the correctness of the vehicle-bridge coupling program in this article, by disregarding the pavement state, reducing the vehicle speed to 1 m/s and setting the load step to 0.002 s, the vertical displacement generated by a vehicle passing the bridge and the analysis results of the static force of ANSYS are compared. The selected measuring points are 8 and 9, as shown in Figures 4(a) and 4(b), and the comparison results are shown in Figure 4.

A comparative analysis of Figure 4 reveals that the error between the simulated static analysis results of the MATLAB program in this article and the static analysis results of the ANSYS solid model is very small (within 5%), which shows

TABLE 3: Dynamic impact coefficient of composite box girder with corrugated steel webs.

Span (m)	Material type	CHN 89 edition specification	CHN 15 edition specification	USA 92 edition specification	JPN 96 edition specification	CAN specification
30	Concrete bridge	0.113	0.249	0.224	0.250	0.400
	Steel bridge	0.222	0.249	0.224	0.250	0.400
50	Concrete bridge	0.000	0.177	0.173	0.200	0.400
	Steel bridge	0.171	0.177	0.173	0.200	0.400
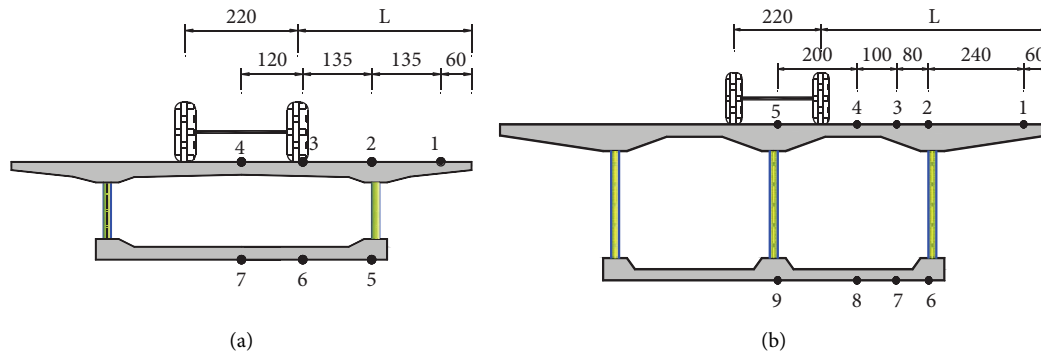
FIGURE 3: Schematic layout of the measuring points of the composite box girder: (a) single box, single cell measuring point arrangement (cm) and (b) single box, twin cell measuring point arrangement (cm).

that the procedure of this article is correct and verifies that the modal order is taken to meet the calculation accuracy requirements.

4.1. Analysis of the Deflection Impact Coefficient of Composite Box Girders with Different Cross-Sections.

In the calculation of the vehicle-bridge coupling analysis program, considering that the pavement state is divided into five levels in the International Organization for Standardization, the relevant specifications also clearly stated that the pavement condition has a greater impact on the impact coefficient. When the vehicle is travelling at a speed of 5 m/s, the time-history curve of the midspan deflection of the 30 m simply supported composite box girder with corrugated steel webs under different bridge deck conditions is shown in Figure 5. Figure 5(b) clearly shows that the dynamic shock response is significantly enhanced when the bridge deck is in poor condition and is significantly different when the bridge deck is in good condition.

To compare the difference between the impact coefficient of the composite box girder and the corresponding concrete box girder at the same frequency, the 30 m simple-supported composite box girder of sample 1 was selected as an example, using the vehicle-bridge coupling program in this article to calculate a vehicle speed of 5 m/s. The calculation results are shown in Tables 4 and 5. Figure 6 shows a comparison of the average value of the dynamic impact coefficient for each measuring point under different bridge deck conditions. Figure 7 shows the dynamic impact coefficient for each measuring point of the roof under different bridge deck conditions.

A comparison of Tables 4 and 5 shows the following findings: (1) The condition of the bridge deck has a great influence on the dynamic impact coefficient. When the condition of the bridge deck ranges from normal to very poor, the calculated dynamic impact coefficient is greater than the dynamic impact coefficient calculated in Table 3 according to the bridge specifications, which indicates that the dynamic impact coefficient given by the current Chinese bridge codes is applicable to the bridge deck in good or better condition. (2) When the bridge deck condition is very good and good, the dynamic impact coefficient of the composite box girder with corrugated steel webs is similar to that of the ordinary concrete box girder, which suggests that when the road surface is in good condition, the dynamic impact coefficient of an ordinary concrete box girder can be used to analyse the corrugated steel web composite box girder by simply changing the web. (3) When the condition of the bridge deck ranges from normal to poor, the average dynamic impact coefficient of the composite box girder is larger than that of the general concrete box girder (as shown in Figure 6), and as the condition of the bridge deck deteriorates, the increasing trend becomes more obvious. When the bridge deck is in poor condition, the impact coefficient of the composite box girder is increased by approximately 70% compared to the concrete box girder. (4) The dynamic impact coefficient of the two types of box girders will gradually increase from the centroid to the outside along the horizontal axis (as shown in Figure 7).

4.2. Analysis of the Strain Impact Coefficient of Vehicles Driving in Different Positions.

After analysing the deflection impact coefficient of the composite box girder and the corresponding concrete box girder, determining whether the strain impact coefficient is consistent with the deflection impact coefficient value needs further analysis. The 50 m simply supported composite box girder with corrugated steel webs of sample 2 was selected as the research object. The
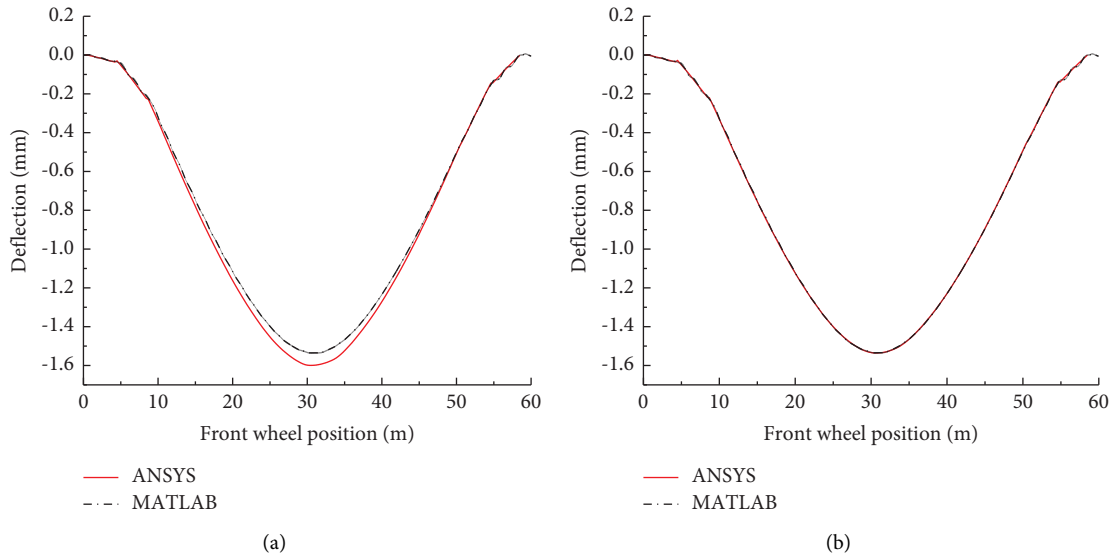
FIGURE 4: Comparison of deflection time history of 50 m composite box girder midspan measurement points in ANSYS and MATLAB. (a) Measuring point 8. (b) Measuring point 9.
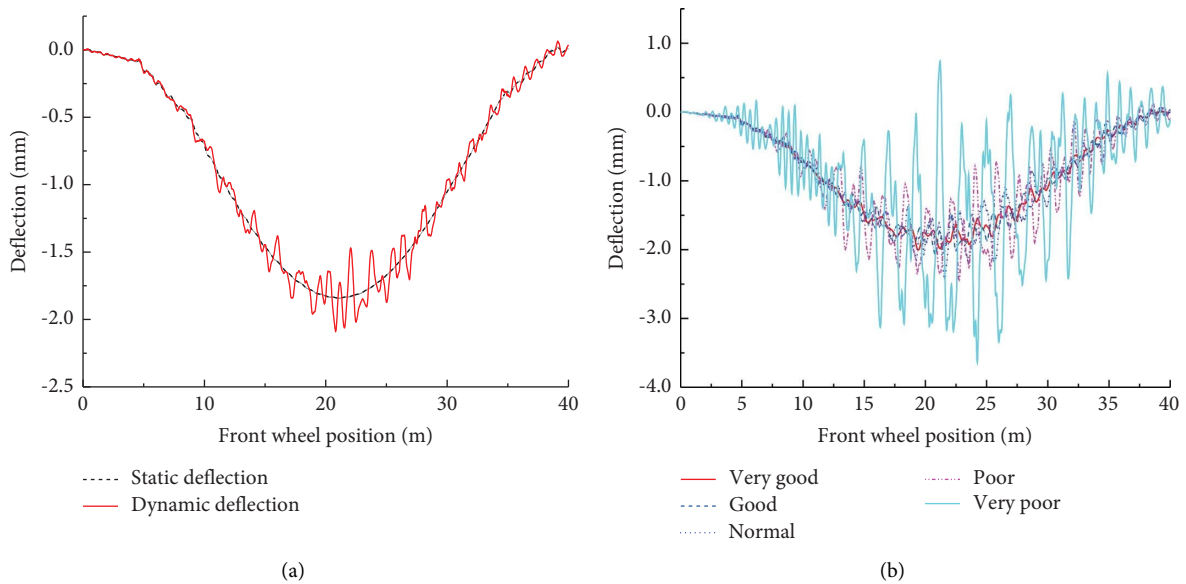
FIGURE 5: Deflection time-history curve of the midspan cross-section of the 30 m simply supported composite box girder under different road conditions. (a) Typical dynamic deflection time history curve (the bridge deck is in good condition). (b) Time point curve of measuring point 5 under different bridge conditions.

TABLE 4: Deflection dynamic impact coefficient of the 30 m simply supported composite box girder.

Measuring point	Very good	Good	Normal	Poor	Very poor
1	0.069	0.134	0.328	0.639	2.032
2	0.059	0.112	0.273	0.555	1.768
3	0.052	0.096	0.231	0.486	1.546
4	0.047	0.084	0.203	0.449	1.369
5	0.060	0.113	0.274	0.557	1.775
6	0.056	0.104	0.254	0.517	1.611
7	0.052	0.092	0.226	0.487	1.413

TABLE 5: Deflection dynamic impact coefficient of the 30 m simply supported concrete box girder.

Measuring point	Very good	Good	Normal	Poor	Very poor
1	0.067	0.139	0.259	0.603	1.087
2	0.061	0.127	0.230	0.538	0.986
3	0.055	0.114	0.204	0.471	0.875
4	0.049	0.104	0.186	0.422	0.794
5	0.061	0.128	0.231	0.538	0.986
6	0.057	0.122	0.215	0.487	0.918
7	0.053	0.113	0.195	0.444	0.828
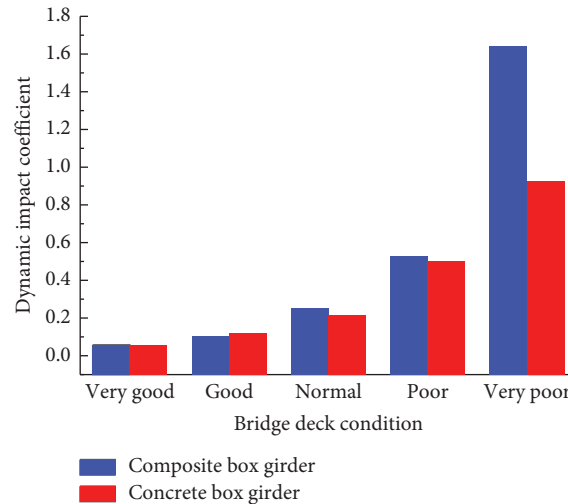
FIGURE 6: Comparison of the dynamic impact coefficients of the two box girders under different bridge deck conditions.
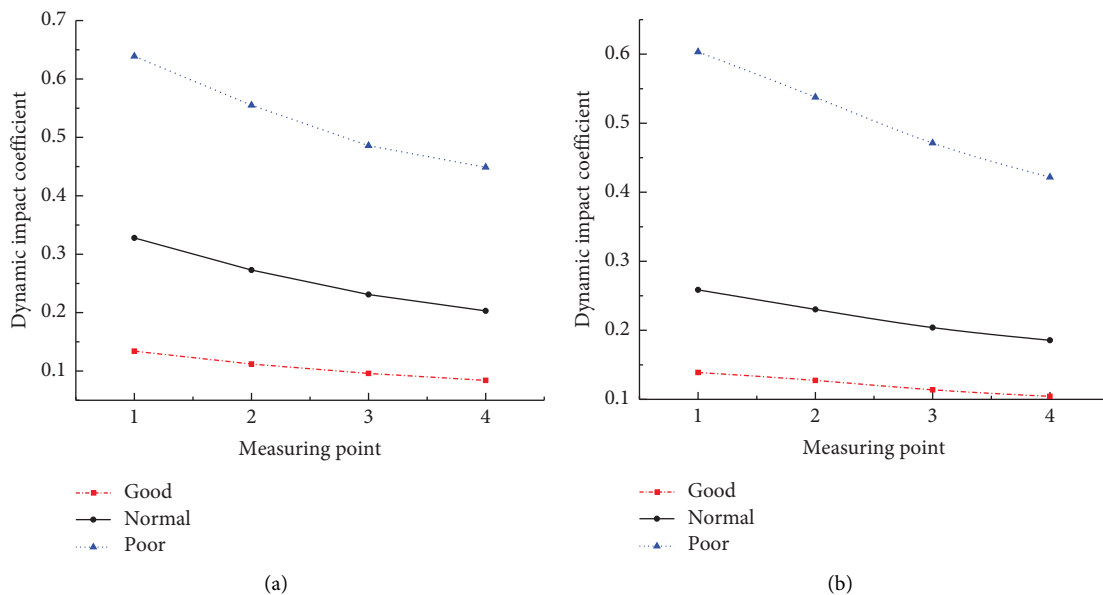
FIGURE 7: Dynamic impact coefficient of each measuring point of the roof under different road conditions: (a) composite box girder and (b) concrete box girder.

typical dynamic strain time-history curve of the 50 m composite box girder midspan floor is shown in Figure 8. The vehicle is driven with two loads, medium load ($L = 5.8$ m) and partial load ($L = 1$ m), and the strain dynamic impact coefficient of each measuring point is analysed, as shown in Tables 6 and 7. Only the three conditions of the bridge deck are good, medium, and poor.

A comparison of Tables 6 and 7 shows the following findings: (1) When the condition of the bridge deck is good, the difference between the strain dynamic impact coefficients of the two driving modes is small, but as the condition of the bridge deck deteriorates, the gap gradually increases. (2) In the case of a poor bridge deck, the eccentric load impact coefficient at point 3 is approximately 68% higher than the intermediate load impact coefficient. (3)

When the bridge deck is in good condition and under the effect of partial load and medium load, the dynamic impact coefficients of measuring point 1 (cantilever plate), measuring point 5 (top plate centre), and measuring point 9 (bottom plate centre) are similar, and in other parts, the midload impact coefficient is less than the eccentric load impact coefficient. (4) Comparing the dynamic impact coefficient (0.177) calculated by current Chinese codes, the strain dynamic impact coefficient is higher than approximately 69% when the bridge deck condition is normal.

The current general code for bridge and culvert design in China stipulates that the dynamic impact coefficient is 0.3 when performing local check calculations on T-beam and box beam cantilever plates. As shown in Tables 6 and 7, under acceptable bridge deck conditions, the longitudinal

TABLE 6: Strain dynamic impact coefficient of each measuring point of the composite box girder when $L = 5.8$ m.

Measuring point	Good	Normal	Poor
1	0.113	0.324	0.441
2	0.102	0.303	0.398
3	0.106	0.308	0.402
4	0.106	0.310	0.404
5	0.124	0.320	0.435
6	0.107	0.305	0.434
7	0.112	0.317	0.441
8	0.118	0.328	0.447
9	0.124	0.335	0.435

TABLE 7: Strain dynamic impact coefficient of each measuring point of the composite box girder when $L = 1.0$ m.

Measuring point	Good	Normal	Poor
1	0.111	0.324	0.597
2	0.122	0.326	0.611
3	0.131	0.353	0.674
4	0.135	0.361	0.735
5	0.128	0.334	0.633
6	0.117	0.336	0.623
7	0.119	0.335	0.634
8	0.122	0.336	0.661
9	0.123	0.337	0.652
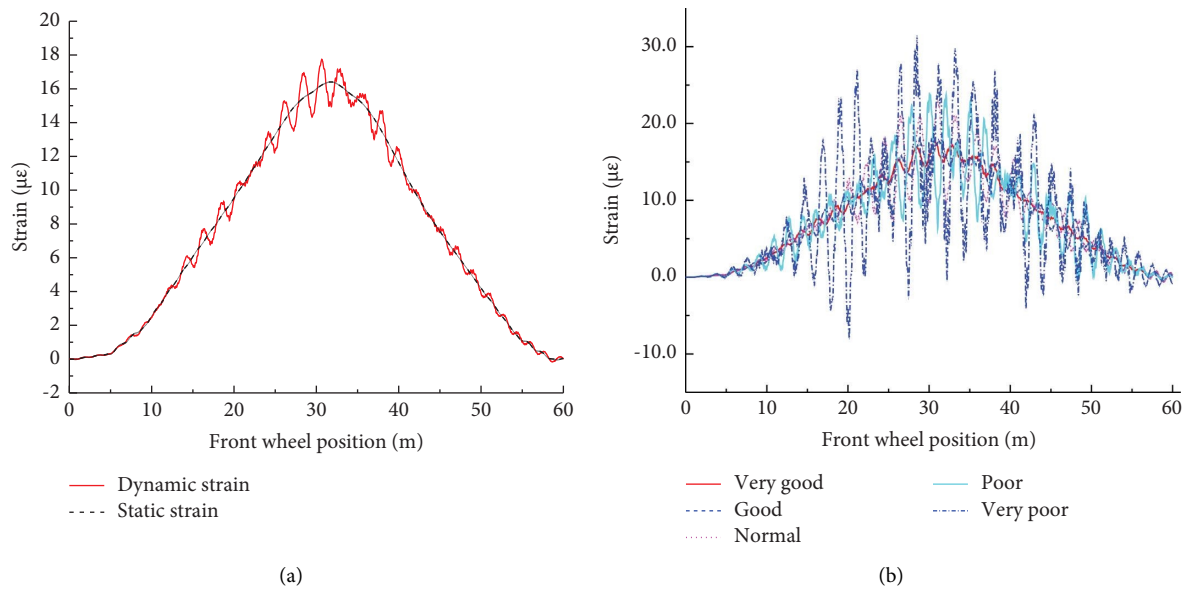
FIGURE 8: Longitudinal normal strain time history curve under different bridge deck conditions: (a) typical longitudinal normal strain time history curve and (b) longitudinal normal strain time history curve under different bridge deck conditions.

normal strain does not exceed the standard value, but when the bridge deck condition is poor, the coefficient obviously exceeds the specification value. The transverse stress of the combined box beam cantilever plate, especially the transverse normal stress at the root of the cantilever plate, is an important part of its local check. Therefore, still taking the 50 m simple-supported composite box girder as an example to analyse the transverse stress impact coefficient of the cantilever plate root, the model is a three-axle vehicle with a lateral L = 2.8 m and a speed of 5 m/s. The bridge deck condition is good, the tension is positive, and the

compression is negative. Figure 9 shows the transverse normal strain time-history curve of the cantilever plate root at the midspan of the composite box girder with corrugated steel webs.

The lateral normal strain time history curve of Figure 9 shows that when the vehicle crosses the bridge, the transverse normal strain at the root of the cantilever plate will have multiple peaks and troughs. When the front axle of the vehicle reaches the position near the midspan, the maximum tensile stress occurs. When the middle axis reaches the midspan (the front axis is approximately 34 m), the second
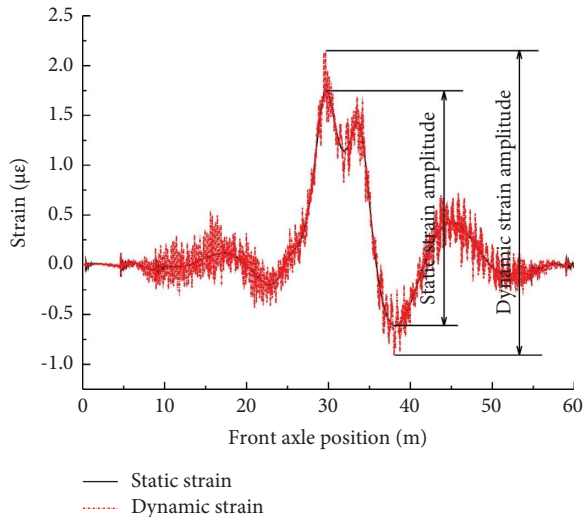
FIGURE 9: Typical lateral normal strain time history curve of the cantilever plate root.

TABLE 8: Transverse strain dynamic impact coefficient of the cantilever plate root of a 50 m simply supported composite box girder.

Measuring point	Lateral strain	Good	Normal	Poor
1	Tensile strain	0.212	0.471	1.357
	Compressive strain	0.637	1.370	4.552
2	Tensile strain	0.219	0.489	1.390
	Compressive strain	0.613	1.307	4.329

peak tensile stress appears. When the rear axle reaches the midspan (the front axle is approximately 38.5 m), the maximum compressive stress occurs. The static stress amplitude and dynamic stress amplitude in the figure are quite different, but these phenomena have an important effect on the fatigue stress amplitude of the transverse reinforcement of the composite box girder and the shear fatigue stress amplitude of the corrugated steel web. Therefore, the lateral dynamic impact coefficient of the cantilever plate root should be clarified.

To analyse the dynamic impact coefficient of the transverse normal strain of the cantilever plate root of the composite box girder, two measuring points (3.2 m and 3.0 m from the edge of the cantilever plate) of the midsection cantilever plate of the 50 m simply supported composite box girder were selected to calculate the transverse normal strain dynamic impact coefficient, as shown in Table 8.

A comparison of Tables 7 and 8, under the same bridge deck conditions, reveals that the transverse strain impact coefficient is greater than the longitudinal strain impact coefficient. When the composite box girder is locally checked and the bridge deck is in good condition, its average transverse strain impact coefficient also reaches 0.42. However, the coefficient given in the current Chinese codes is only 0.3, and the impact coefficient is greater in other bridge deck conditions. As the impact coefficient has an important effect on the calculation of the fatigue stress amplitude of the transverse reinforcement of the cantilever

plate of the combined box girder and the fatigue stress amplitude of the corrugated steel webs under shear, special attention should be given to it.

4.3. Impact Analysis of Vehicle Condition. According to domestic and international codes, the dynamic impact coefficient of the bridge is related to the number of axles and vehicle speeds. To analyse the influence of vehicle factors on the dynamic impact coefficient of the composite box girder with corrugated steel webs, the 30 m simply supported composite box girder with corrugated steel webs of sample 1 was selected, and the deflection dynamic impact coefficient of each measuring point for different axle vehicle loads and different vehicle speeds (7.6 km/h–93.6 km/h) was calculated. The results are shown in Figures 10–12. Both types of vehicles use the same bridge deck conditions, acting on the bridge deck's lateral position L = 3.4 m. The shading in the figure indicates the deflection impact coefficient of the composited box girder analysed in accordance with our country's current codes, the dot-dashed line indicates the limit dynamic impact coefficient analysed according to AASHTO, and 1-7 represent the measurement points shown in Figure 3(b).

Figures 10–12 show that the dynamic shock coefficient calculated by using the US code is greater than the calculation results of the Chinese code. A comparison and analysis of the dynamic impact coefficient of each measuring point reveals that the quality of the bridge deck and the vehicle model and speed will affect the impact coefficient. As the condition of the bridge deck changes from good to poor, the dynamic impact coefficient of each measuring point gradually increases. When the condition of the bridge deck is good, the dynamic impact coefficient of each measuring point is less than the national standard value, and when the condition of the bridge deck is normal, the dynamic impact coefficient of most of the measuring points is greater than the national standard value. When the condition of the bridge deck is poor, the dynamic impact coefficients of almost all the measuring points are greater than the national norms. With an increase in vehicle speed, the dynamic shock coefficient shows a trend of increasing-decreasing-increasing-decreasing, but the specific change range exhibited by different vehicle types is different. For two-axle vehicles, the speed range with a large impact coefficient is between 20 km/h and 50 km/h; for three-axle vehicles, the speed range with a large impact coefficient is between 60 km/h and 80 km/h. To further illustrate the impact of different vehicle types on the impact coefficient, the average value of the dynamic impact coefficient of each measurement point at different vehicle speeds is shown in Figure 13. As the condition of the bridge deck changes from good to poor, the dynamic impact coefficient gradually increases. Under the same conditions and speed of the bridge deck, if the vehicle type is different, the dynamic impact coefficient is different. With increasing speed, the dynamic shock coefficient has changed from being larger for two-axle models than three-axis models to being larger for three-axis models than two-axis models.
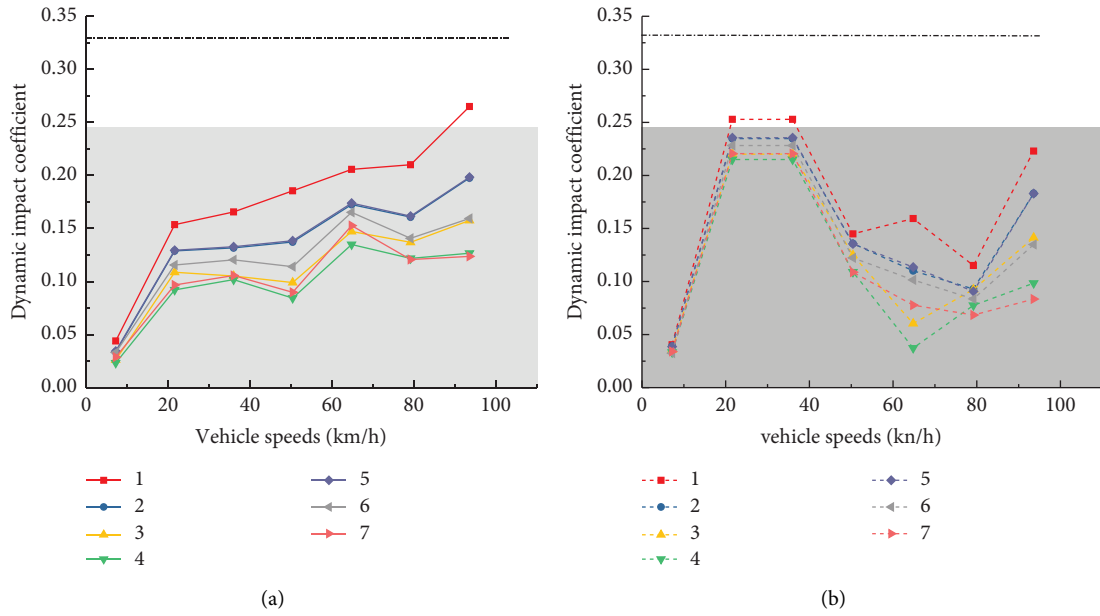
FIGURE 10: Coefficient of dynamic shock when bridge deck is good. (a) Three-axis models. (b) Two-axis models.
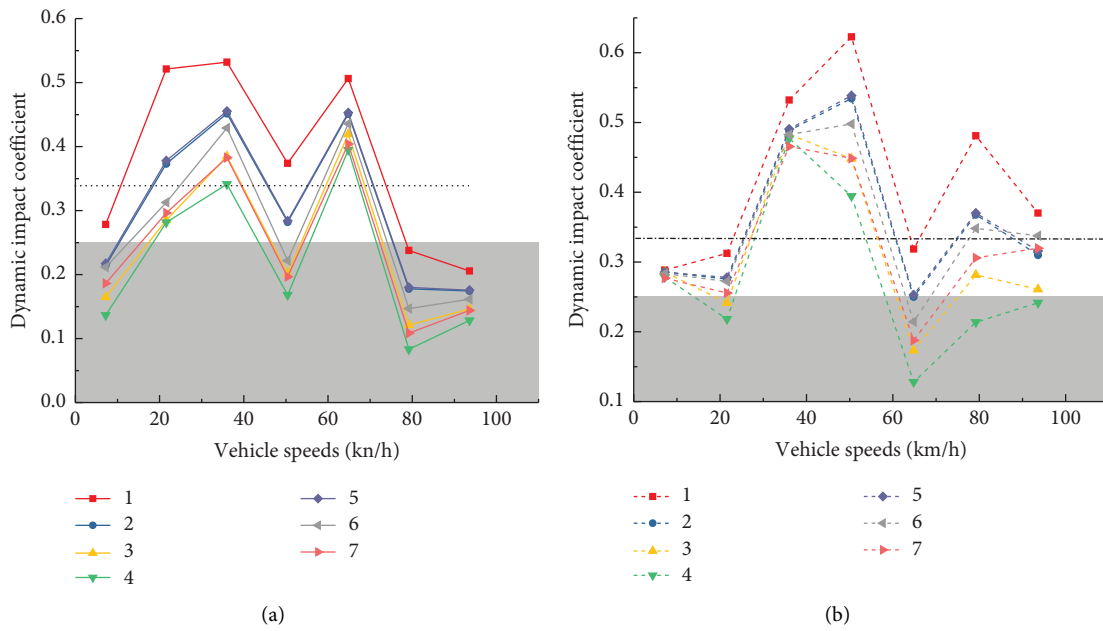
FIGURE 11: Coefficient of dynamic shock when bridge deck is medium. (a) Three-axis models. (b) Two-axis models.

(a)

(b)
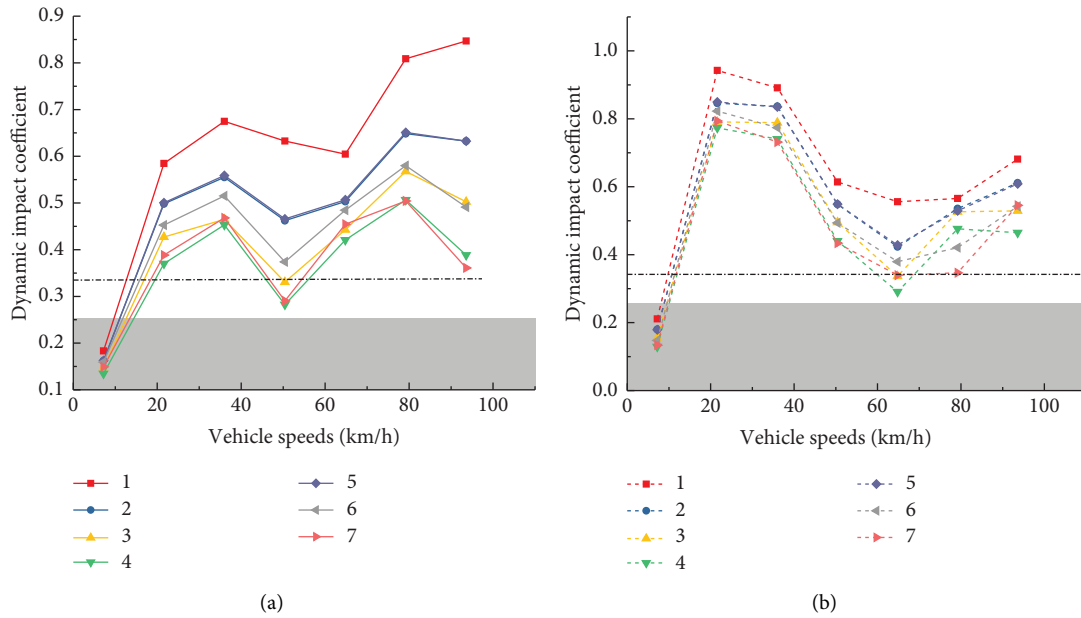
FIGURE 12: Coefficient of dynamic shock when bridge deck is poor (a) Three-axis models. (b)Two-axis models.

(a)

(b)

(c)
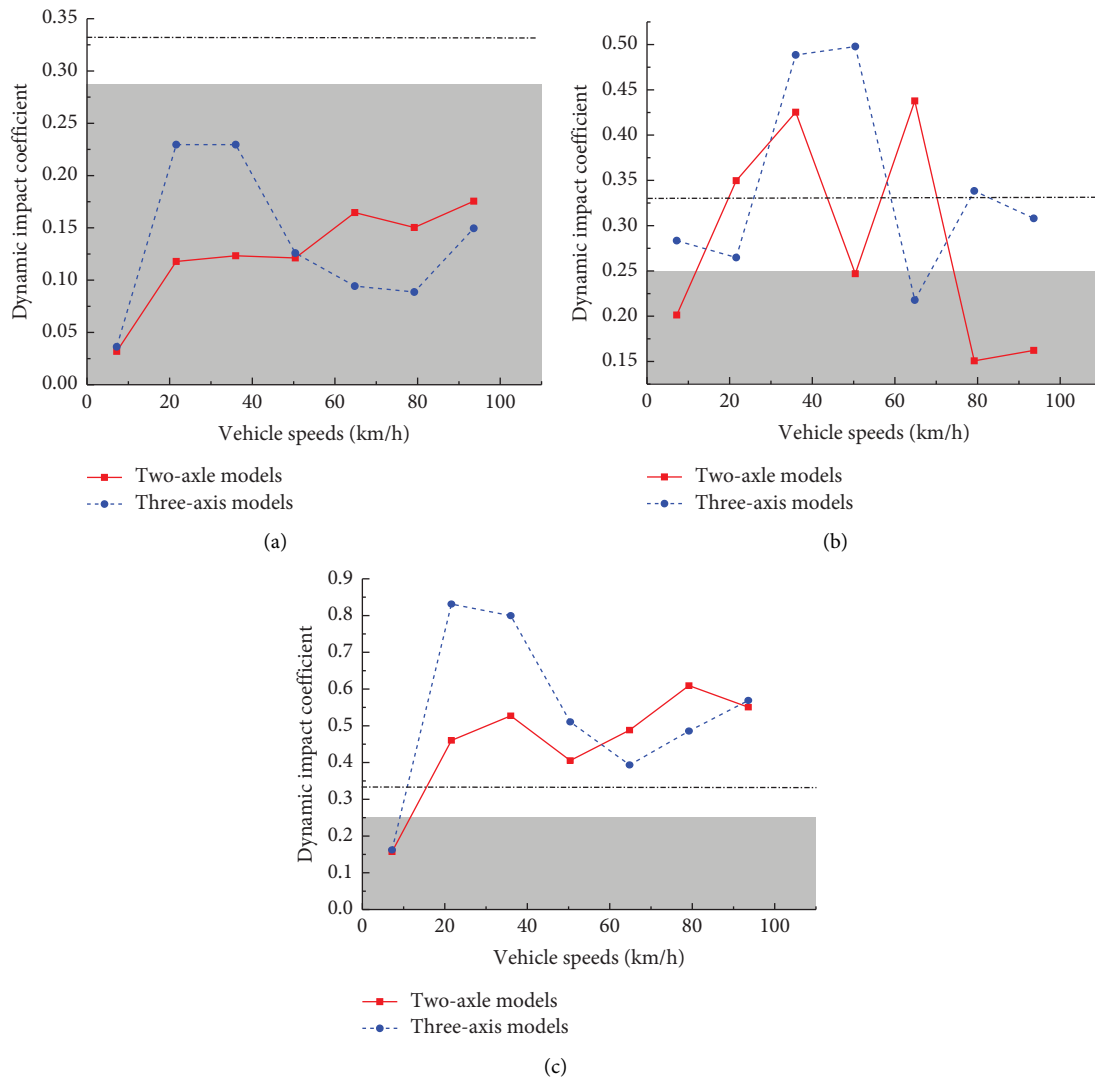
FIGURE 13: Comparison of the mean value of the dynamic shock coefficient of two types of vehicles. (a) Good bridge deck. (b) Normal bridge deck. (c) Poor bridge deck.

5. Conclusion

By an investigation of the dynamic response of composite box girder bridges with corrugated steel webs, the following conclusions are drawn:

(1) When the composite box girder with corrugated steel webs is replaced with an ordinary concrete web with equal wave height, the difference between the low-order deflection natural frequencies of the two box girders is small. However, the difference between them will increase as the frequency order increases, and the frequency of the composite box girder with corrugated steel webs is lower than that of the corresponding concrete box girder. The comparison results of the deflection impact coefficients of the two types of box girder show that when the bridge deck is in good condition, the gap between the two results is small, and when the bridge deck is in poor condition, the dynamic impact coefficient of the composite box girder is much larger than that of the concrete box girder.

(2) A comparison of various factors that affect the flexural dynamic impact coefficient of the composite box girder reveal that the quality of the bridge deck has the most obvious impact on the dynamic response. According to a comparison of the refined vehicle-bridge coupling vibration analysis results, the calculation methods of the impact coefficient in most domestic and international bridge codes are only applicable to the situation where the bridge deck condition is good or better.

(3) Unlike the dynamic impact coefficient of deflection, the local characteristics of the dynamic impact coefficient of strain are relatively obvious, and when a vehicle is driven under the conditions of intermediate load and partial load, the gap between two strain impact coefficients of some measurement points is large. When the combined box girder is locally checked and the bridge deck is in good condition, its average transverse strain impact coefficient also reaches 0.42. However, the coefficient given in our country's current codes is only 0.3, and the impact coefficient is greater in other bridge deck conditions. Thus, special attention should be given to the design.

(4) The quality of the bridge deck and the vehicle model and speed will affect the impact coefficient. As the bridge deck changes from good to poor, the dynamic impact coefficient gradually increases. With increasing vehicle speed, the dynamic shock coefficient shows a trend of increasing-decreasing-increasing-decreasing, but the specific change range exhibited by different vehicle types is different. For two-axle vehicles, the speed range with a large impact coefficient is between 20 km/h and 50 km/h. For three-axle vehicles, the speed range with a large impact coefficient is between 60 km/h and 80 km/h. With increasing speed, the dynamic shock coefficient has changed from being larger for two-axle models larger than three-axis models to being larger for three-axis models than two-axis models.

References

[1] Z. Zhang, G. Wang, and F. Jiang, "Natural vibration characteristics of continuous box composite girder with corrugated steel webs of uniform cross-section," *China Railway Science*, vol. 42, no. 4, pp. 51–59, 2021.

[2] S. Chen, C. Zhang, and G. Shuirong, "An experimental study on dynamic characteristics of a single-box multi-cell composite girder bridge with corrugated steel webs," *Journal of Vibration and Shock*, vol. 36, no. 12, pp. 122–127, 2017.

[3] S. Zheng, S. Wan, and H. Cheng, "Research on the dynamic characteristics of multi－room single box composite girder with corrugated steel webs," *Journal of Railway Engineering Society*, vol. 34, no. 9, pp. 41–46, 2017.

[4] S. Zheng, K. Hu, and H. Cheng, "Analysis on influence of externally prestressed tendons on fundamental frequency of continuous box girder with corrugated steel webs," *Journal of Railway Engineering Society*, vol. 38, no. 5, pp. 53–59, 2021.

[5] W. Wang, D. Zhai, Y. Bai et al., "Loss of QKI in macrophage aggravates inflammatory bowel disease through amplified ROS signaling and microbiota disproportion," *Cell death discovery*, vol. 7, no. 1, pp. 58–65, 2021.

[6] J. Wei, L. Deng, and W. He, "Vehicle-bridge coupled vibration analysis and calculation of dynamic impact factor for the PC box-girder bridge with corrugated steel webs," *Journal of Vibration Engineering*, vol. 29, no. 6, pp. 1041–1047, 2016.

[7] J. Wei, L. Deng, and W. He, "Local and global impact factors analysis for PC box girder bridges with corrugated steel webs," *Vibration and Shock*, vol. 36, no. 8, pp. 22–28, 2017.

[8] *JTG D60-2015 General Specification for Design of Highway Bridges and Culverts*, People's Communications Press Co. Ltd, Beijing, China, 2015.

[9] L. Li, *Flexural Mechanical Properties and Experimental Study of Corrugated Steel Web Composite Box Girders Considering Shear Deformation*, Doctoral dissertation of Lanzhou Jiaotong University, Gansu, China, 2019.

[10] L. Deng and W. Wang, "Research progress of highway bridge dynamic impact coefficient," *Journal of Dynamics and Control*, vol. 14, no. 4, pp. 289–300, 2016.

[11] L. Deng, W. He, and F. Wang, "Dynamic impact factors for simply supported bridges with different cross-section types," *Vibration and Shock*, vol. 34, no. 14, pp. 70–75, 2015.

[12] L. Deng, W. Wang, and X. He, "Optimization and application of fatigue design based on AASHTO code," *Journal of China Highway and Transport*, vol. 30, no. 3, pp. 40–48, 2017.

[13] American Association of State Highway and Transportation Officials, *Standard Specifications for Highway Bridges*, Aashto, Washington, DC, USA, 1992.

[14] American Association of State Highway and Transportation Officials (Aashto), *AASHTO LRFD Bridge Design Specifications 6thed*, AAASHTO, Washington, DC, USA, 2012.

[15] Japan Road Association, *Specifications for Highway Bridges, Part 1*, Common Specifications, Tokyo, Japan, 1996.

[16] Ontario Ministry of Transportation and Communications, *Ontariohighway Bridge Design Code*, Toronto, Ontario, Canada, 1983.

[17] Ontario Ministry of Transportation and Communications, *Ontariohighway Bridge Design Code*, Toronto, Ontario, Canada, 1991.

[18] M. Zhou, Y. Zhang, and L. Li, "Research on bending vibration frequency of thin-walled simply supported box girder," *Highway Transportation Science and Technology*, vol. 35, no. 1, pp. 72–78, 2018.

[19] Ministry of Communications of the People's Republic of China, *JTJ 021-89 General Specification for Design of Highway Bridges and Culverts*, People's Communications Press, Beijing, China, 1989.

[20] L. Deng and C. S. Cai, "Identification of parameters of vehicles moving on bridges," *Engineering Structures*, vol. 31, no. 10, pp. 2474–2485, 2009.

[21] X. F. Yin, Z. Fang, C. S. Cai, and L. Deng, "Non-stationary random vibration of bridges under vehicles with variable speed," *Engineering Structures*, vol. 32, no. 8, pp. 2166–2174, 2010.

[22] L. Deng, *System Identification of Bridge and Vehicle Based on Their Coupled vibration*, Louisiana State University, Baton Rouge, LA, USA, 2009.

[23] X. Li, L. Zhang, and J. Zhang, "State-of-the-art review and trend of studies on coupling vibration for vehicle and highway bridge system," *Engineering Mechanics*, vol. 25, no. 03, pp. 230–240, 2008.

Hindawi

Research Article

Numerical Analysis of a Dual-Layer Geosynthetic-Encased Stone Column Installed in Soft Soil

Neeraj Kumar [ID],[1] Rakesh Kumar [ID],[1] Bhawani S. Nirola [ID],[2] and Akash Jaiswal [ID][1]

[1]*Department of Civil Engineering, MANIT, Bhopal 462003, India*
[2]*College of Science and Technology, Royal University of Bhutan, Phuentsholing 21101, Bhutan*

Correspondence should be addressed to Bhawani S. Nirola; bhawani.cst@rub.edu.bt

Stone columns are being used to reduce soft soil settlement and increase load-carrying capacity. Since there is inadequate lateral support from the local native soil, soft soil undergoes excessive settlement under vertical loading. This issue is effectively resolved by suitably encasing stone column material by geosynthetic with significant axial stiffness, which provides the required additional confinement reported in the literature. In the current study, an effort has been made to examine the load settlement behaviour of the dual-layered geosynthetic-encased stone column (DL-GESC) under vertical loading. In order to simulate the behaviour of stone column-reinforced soft soil, a FEM analysis was performed using PLAXIS-3D and three-dimensional (3D) models made utilising the unit cell idealisation technique for a single column. The stone column diameter, spacing to diameter (s/d) ratio, and encasement layers were varied to determine their influence on load-settling behaviour. The vertical load-carrying capacity of the ground was significantly improved when an additional layer of geosynthetic encasement was inserted into the stone column as compared to SL-GESC. Improvement of 15–25% was observed for the analysis of a single column installed in soft clay, according to the result obtained. Improvement ratios have been discussed in detail for various encasement conditions.

1. Introduction

Using soft clay deposits or fills as a foundation material is generally not suggested. The viability of construction there must be determined in light of the favourable economic conditions for land development brought on by the expansion of urban and industrial regions. Stone columns are, without a doubt, the most popular and desirable alternatives. When the load-carrying capacity of the soil rises, it is less probable that storage tanks, earthen embankments, raft foundations, and other foundations undergo failure due to settlement. Insertion of ordinary stone column increase soil to greater depth and minimise problems induced by settlement. Numerous geotechnical problems that might occur with poor soil can be resolved through ground improvement [1]. Columnar inclusion is among the most flexible and economical ground augmentation techniques available today. Compared to the soil around them, columnar inclusions are more durable and resilient. Stone columns, lime or cement columns, compacted sand piles, or other columnar inclusions can be considered as composite materials. Granular pile reinforcement in soft ground is used to improve field performance by increasing bearing capacity and reducing settlement [2, 3]. Over the past three decades, this method has seen extensive usage for a wide range of applications, including the compression of cohesionless soil and the insertion of stone columns of reinforcement into softer soil. It has outpaced most conventional deep foundation techniques, such as piling. Circumferential bulging of the stone column helps to transmit the longitudinal load, which increases the stiffness of the ground. The lateral confinement or bulging resistance offered by the intervening soil was found to be inadequate for particularly soft soil [4, 5].

The stone column method is economical and environmentally friendly for stabilising unstable ground so that it can withstand low-to-moderate stress situations [6]. It increases the stability and stiffness of the soil, reduces the

likelihood of liquefaction and pore pressure, enhances shear strength and stability, and accelerates the consolidation of drained soil. Introducing tensile materials in horizontal, vertical, and inclined orientations is another well-known method of improving and strengthening soil. Geosynthetics have become a significant component in soil reinforcement because of advancements in polymer engineering and the development of innovative materials. Van Impe [7] was the first to suggest covering a stone column with a geosynthetic material. Since then, numerous research studies have been conducted to use reinforced stone columns to enhance the properties of soft soil by researchers [8–10], whereas Fathi and Mohtasham [11] demonstrated the stone column by increasing the stiffness of geosynthetic materials, improved soil stability, and load-bearing capacity.

In order to strengthen the stone column carrying capacity and prevent any related failures, it was thus necessary to increase the circumferential bulging resistance [12–16]. By adjusting the length of the encasement, Gniel and Bouazza [17] investigated small-scale geogrid-encased columns. In both single and group columns, encasement length reduced the upright strain [18, 19]. Below the encasement, there was a bulging collapse, fully enclosed columns minimise the strain by 80%. It has been proven to be very successful in increasing the bearing capacity in a vertically laden column to utilise a variety of geosynthetics as part of an encasement [20–29].

Various studies proposed that using horizontal layers of geosynthetics encasement helps to improve the bearing capacity and reduce lateral bulging [30–32]. Three-dimensional numerical studies reported that short end-bearing columns with GESC had higher bearing capacities than longer ones because they transmitted compressive load across their entire length and mobilised higher strains for a specified settlement. Also, the short geogrid-encased sand column exhibited less lateral expansion for a given settlement than larger-diameter encasement [33]. Miranda et al. [34] established the critical length using FEM analysis and found that extending the column past the critical length had no advantage. For enclosed stone columns, the required column length should be 1.3–2.5 times the footing's diameter; for OSC, it should be 1.1–1.9 times the footing's diameter. The length of ordinary, encased stone columns should be 2 to 5 times the diameter of the footing. The influence of stone columns coated with geosynthetics under cyclic loads was examined by Gao et al. [35] and concluded that by doing such reduces foundation settlement.

Ordinary stone columns (OSC) built on the soft ground could now be strengthened by using geosynthetic-encased stone columns (GESC), which has gained in importance. An ordinary stone column can also be loaded and arranged such that they do not slide laterally into the ground next to the building. Due to insufficient lateral pressure from the soil around them, GESCs come into play when OSCs in a soil environment are unable to maintain column integrity. The major factor determining which system—the GESC system or the OSC system—offers a lesser cost benefit when both systems are applicable at the same location is the project boundary's specific issues, such as settling requirements,

installation difficulties, and loading conditions. As of now, the following criteria have been used to study geosynthetic reinforcement in general:

(a) Using horizontal layers of geosynthetic reinforcement positioned partially and entirely in relation to the length of the stone column to decrease lateral extension (bulging)

(b) Encasing the sand column completely and partially around with a geogrid sleeve

(c) Encasing geosynthetic sleeves circumferentially around the stone column periphery

(d) Reinforcing stone columns horizontally and vertically along with varying encasement lengths

(e) The dual layer idea, which was just recently presented and will be employed for the first time in vertical loading, is still the subject of investigation

The information, as shown, indicates that the encasing was only applied to the stone column periphery. On the other hand, Jaiswal and Kumar [36] recommended using a dual-layered encasement to improve a stone column shear resistance in situations where the column is susceptible to shear collapse. In order to load stone columns in a vertical position, the dual-layer enclosed stone column (DLESC) idea has yet to be used; hence, more research is needed in this area.

The ongoing research aims to create a design method that takes soil and the load distribution of a dual-layer, encased stone column into account. Numerical analysis was used to analyse the behaviour of a single stone column. The study was conducted using a unit cell concept, with clay deformations restricted to the unit cell, which is represented by the equivalent area of each column. The efficiency of stone columns in SL-GESC and DL-GESC soil was assessed in the current study to determine the impact of geogrid encasing.

2. Numerical Modelling

Using a FEM analysis in PLAXIS-3D using 10 nodes, numerical investigations were conducted as part of this research. This FEM package is made up of reliable computational techniques that have stood the test of time. It enables users to analyse and simulate soil behaviour through the creation of 3D soil models, allowing them to tackle challenging geotechnical engineering challenges. The load versus the settlement study, which was done on a single column, was based on the idea of a unit cell. This is due to the tightest packing provided by this layout.

The equivalent diameter (De) of an equivalent cylindrical unit cell is determined as follows: De = 1.05 × s, where s is the column spacing, which is commonly 2 to 4 times the diameter (d). As indicated by the formula s = 2d to 4d, the distance between the stone columns was shifted in the current inquiry between two and four times their diameters. Investigations were conducted on columns with diameters of 50 mm, 75 mm, 100 mm, 125 mm, and 150 mm. A minimum L/d ratio of 4.5 is required to produce the full limiting axial stress on the stone column; nevertheless, no appreciable

improvement in its capacity has been seen. In this analysis, the load versus settlement behaviour in soft soil reinforced by single-layer geosynthetic encased stone columns (SL-GESC) and dual-layer geosynthetic-encased stone columns (DL-GESC) were compared to that of unreinforced soil and ordinary stone column (OSC). This study used the Mohr–Coulomb model, which has been used by many scholars in the past to analyse the behaviour of soft soil and stone columns [27, 31, 37–39]. It was decided that the geosynthetic encasement should be modelled as a linear elastic material.

Studies on the effect of geosynthetic encasing on settlement behaviour in the stone column-reinforced soft soil of varying undrained shear strengths have shown that an interface element is not needed because column settlement is caused by the stone columns bulging to the periphery, which prevents shear [33, 40]. Therefore, interface elements were not used in the case of GESC; however, Rinter = 0.60 was used for the stone column and soil in this study because it yielded a more accurate validation result than the other values tested.

2.1. Validation of the Numerical Model. Perfectly elastic linear material clay was employed as the bed material, and stone aggregates as the column material and the behaviour of each was simulated using Mohr–Coulomb failure criteria. The Mohr–Coulomb model is applicable in the analysis of embankments and shallow foundations. Laboratory model studies on single configurations of stone columns surrounded by soft clays in a triangular pattern were used to approximate the load settlement behaviour of model tests carried out by Ambily and Gandhi [40], utilising the unit cell approach (Figure 1). This was achieved by simulating the load-settling behaviour seen in tests, which were done using stone columns with a 100 mm diameter and end-bearing columns with a 4.5 L/d ratio. In addition, a cylindrical tank with dimensions of 500 mm in height and 210 mm in diameter was selected following the unit cell idealisation concept to achieve an s/d ratio of 2. It was agreed that the end-bearing condition of loading only one column would be considered for the single-column criterion during the validation process.

Material properties used for validation purposes are the same as in Table 1, which was used by [40]. To simulate the test, a cylindrical mould was developed and given the characteristic of steel. Following that, a series of boundary conditions were used to keep the cylindrical mould fixed to restrict mould movement in any direction. A clay-filled mould and a stone column of 100 mm in diameter and 450 mm in length were used to create the model. As indicated in Figure 1, material characteristics were assigned after creating an interface at the boundary. The mesh was created when the necessary and appropriate properties were provided, as seen in Figure 2.

For the relevant conditions, the numerical analysis employed a maximum specified settlement of 35 mm [41]; above this settlement, the increase in axial stress seems to be constant [40]. Figure 3 depicts the vertical displacement
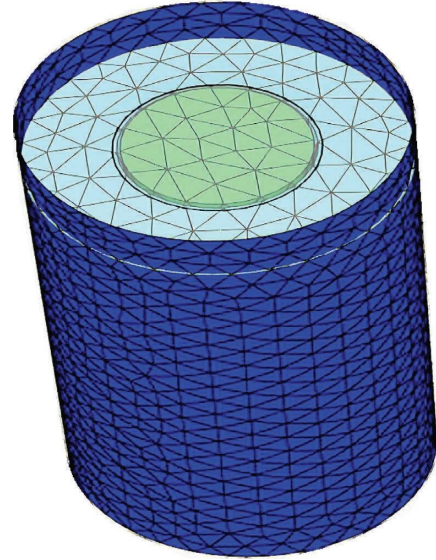
FIGURE 1: Schematic diagram of a soil bed with a single column modelled.

TABLE 1: Material's properties as utilised by Ambily and Gandhi [40].

Parameters	Properties	
	Clay	Stone
Poisson's ratio (μ)	0.42	0.3
Shear strength, c_u (kPa)	30	0
Modulus of elasticity (kPa)	5,500	55,000
Angle of internal friction (ϕ)	0	38°
Dilatancy angle (ψ)	0	4°

applied to the stone column. The result obtained from the numerical study done by PLAXIS-3D is in good agreement with those of the earlier experimental examination by Ambily and Gandhi [40], which was conducted for $s/d = 2$, as shown in Figure 4.

3. Material Properties

Mohr–Coulomb failure criteria were used in the validation of the perfectly plastic linear elastic model used for the behaviour of clay as a bed material and stone aggregates as a column material. The Mohr–Coulomb model has been used by numerous researchers for investigations on stone columns that are similar to those on embankments and shallow foundations [27, 42–45]. The model's input parameters (E, c, φ, and ψ) were obtained from relevant laboratory tests. Five different stone columns, each with a diameter of 50 mm, 75 mm, 100 mm, 125 mm, and 150 mm, were used in the numerical analysis, with variable s/d ratios. Table 2 shows the physical characteristics of the material used in this study. Various parameters were altered to calculate their effects on the soil settling behaviour under various load intensities. The geosynthetic's axial rigidity (J) was fixed at 150 kN/m for both the inner and outer layer
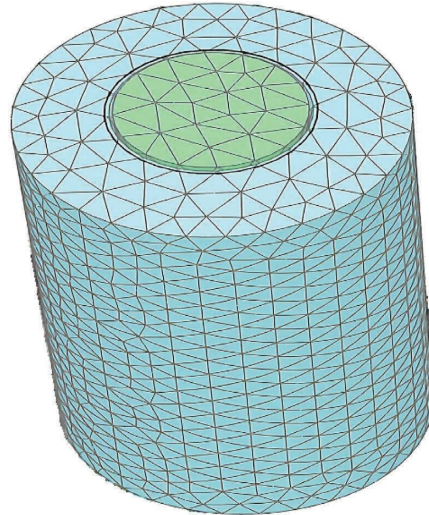
FIGURE 2: Generated mesh of the model with ordinary stone column (OSC).

(a)   (b)
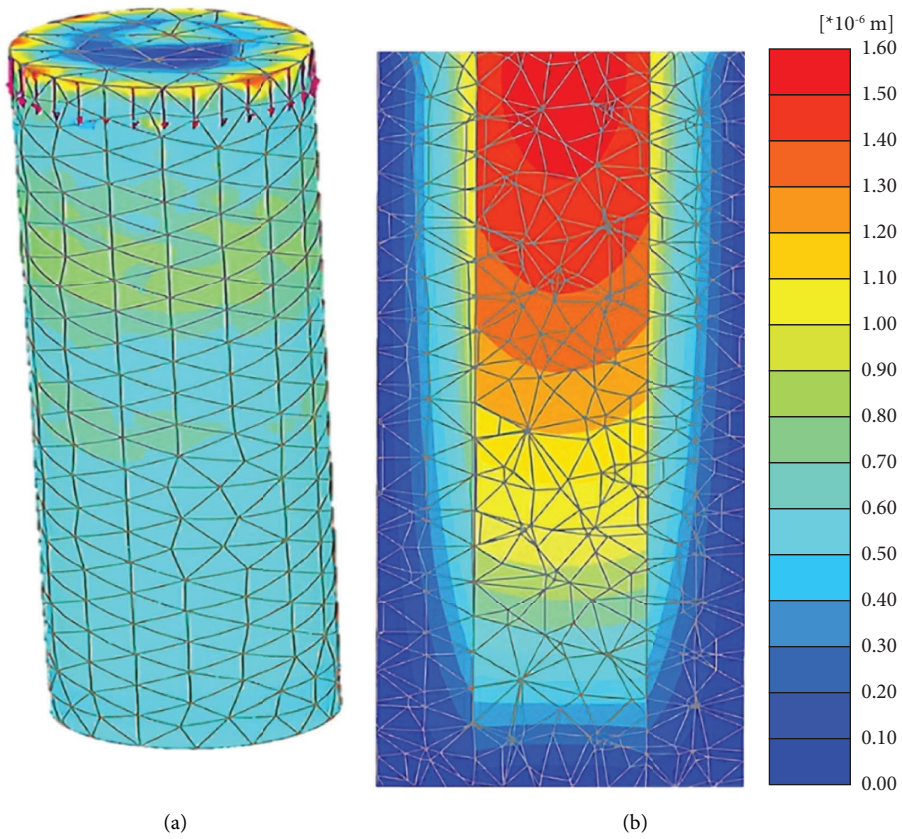
FIGURE 3: (a, b) Stone column with prescribed displacement.
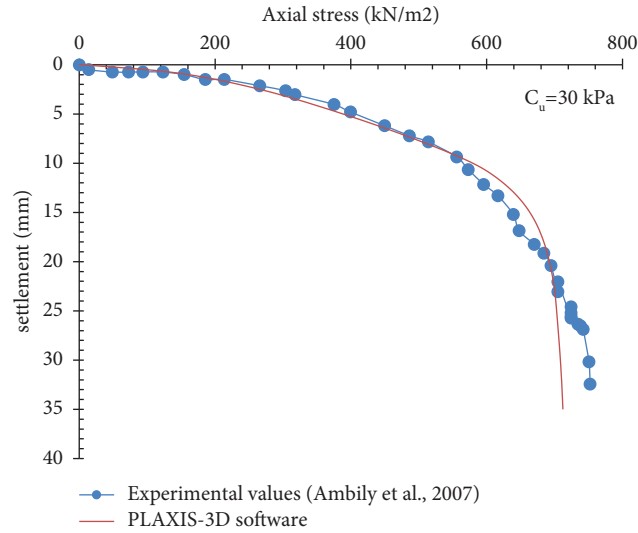
FIGURE 4: Validation of the axial stress versus settlement graph by Ambily and Gandhi [40].

TABLE 2: An overview of the FEM models generated.

| Stone column dia. (mm) | s/d ratio | Single column test Model type | | | |
		DL-GESC	SL-GESC	OSC	CLAY
50	s/d = 2	✓	✓	✓	✓
	s/d = 3	✓	✓	✓	✓
	s/d = 4	✓	✓	✓	✓
75	s/d = 2	✓	✓	✓	✓
	s/d = 3	✓	✓	✓	✓
	s/d = 4	✓	✓	✓	✓
100	s/d = 2	✓	✓	✓	✓
	s/d = 3	✓	✓	✓	✓
	s/d = 4	✓	✓	✓	✓
125	s/d = 2	✓	✓	✓	✓
	s/d = 3	✓	✓	✓	✓
	s/d = 4	✓	✓	✓	✓
150	s/d = 2	✓	✓	✓	✓
	s/d = 3	✓	✓	✓	✓
	s/d = 4	✓	✓	✓	✓

encasings. It was investigated how this dual-layer encasement affected the stone column bulging and load-settlement behaviour.

4. Encasement Conditions

The two types of encasements employed for the single ordinary stone column research were Single-layered geosynthetic-encased stone column (SL-GESC) and dual-layered geosynthetic-encased stone column (DL-GESC). In the case of a single-layer encasement, the encasing layer is placed on the column's outermost periphery, enclosing the whole stone column, as depicted in recent research. While dual-layered encasement employs two layers of encasement, the first layer is the same as that used in single-layered encasement (at the periphery), and this layer remains

consistent throughout all DLGE samples. The second layer of encasement is inserted within the body of the stone column, $0.5d$ from the stone column axis, as shown in Figure 5(a). This leads to a gap of $0.5d$ between the two layers of encasement, which is equal to the spacing between the two layers of the encasement.

5. FEM Modelling by PLAXIS-3D

The diameter and height of the single-column cylindrical tank were maintained by using the unit cell concept and maintaining the L/D ratio of about 4.5. Based on the diameter of a stone column, the PLAXIS-3D software was used to create a cylindrical tank with varying length and diameter. The component of the tank was made of plate elements, and the boundaries of the tank were confined in all three
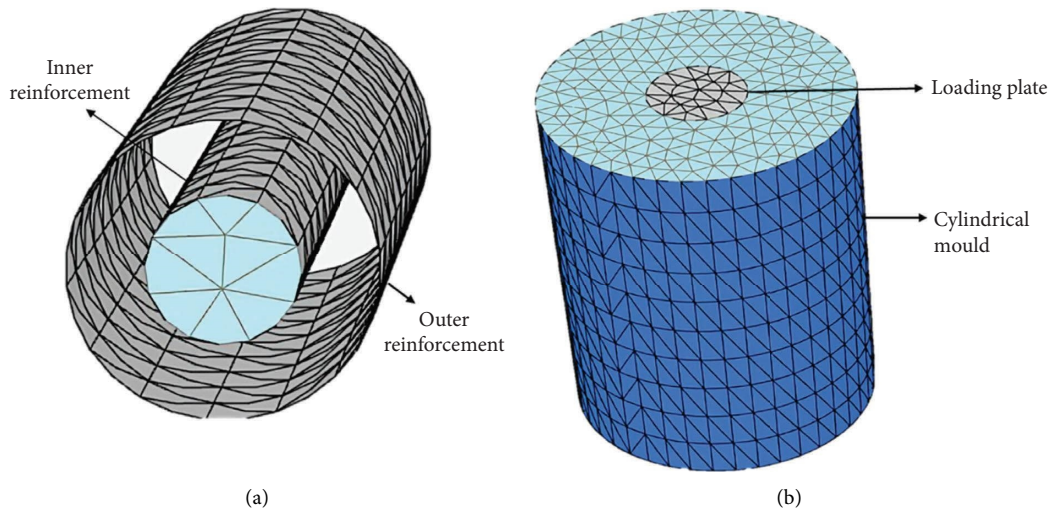
Figure 5: (a) Cross-sectional view of dual-layered encasement for a single stone column and (b) single-stone column setup.

dimensions. The loading plate and its properties were allocated to steel plates with a thickness of 12 mm. A stone column with the requisite diameter was generated in the tank's centre, interacting with the attribute Rinter = 0.6 that is maintained on the column periphery for ordinary stone column (OSC). Encased stone columns (ESC) with a specified tensile strength of 150 kN/m for both the inner and outermost encasement were provided by geogrids. Meshing was done using a medium coarseness, and a predetermined vertical displacement of 50 mm was provided, as shown in Figure 2. On single columns with varied encasement conditions and diameters, 60 FEM models were created and numerically examined. Table 2 displays the general structure of the model, and Figure 5(b) depicts the model of a single ordinary stone column setup with encasement.

6. Results and Discussion

The effect of various factors on the load-intensity versus settlement behaviour of GESCs was analysed using 3D FEM models. Based on their experimental investigation, Ambily and Gandhi [40] suggest that the length of stone columns nearly 4.5d is optimum. In this study also, an end-bearing column with a length to diameter (L/d) ratio of 4.5 was chosen for a single column analysis. The load was applied on top of the stone column in terms of a prescribed displacement of up to 50 mm. The parameters varied included the diameter of stone column, encasement conditions, and s/d ratio. The properties used for the materials modelled in the study are shown in Table 3. Various aspects and outcomes of parametric studies are discussed in detail as follows:

6.1. Effect of Spacing. On the unreinforced soil, ordinary stone column, SL-GESC, and DL-GESC with various diameters and spacings, various FEM analyses were conducted. Figure 6 presents the findings as graphs illustrating the variation in axial stress and axial load for various model parameters. From the result obtained through the FEM

analysis, it shows that the load-carrying capacity of the stone column decreases as the spacing between stone columns increases, this phenomenon continues up to the s/d ratio of 3, beyond which the change becomes negligible. These findings are consistent and in agreement with that of [40, 46]. According to Table 4, which compares the improvement percentage of the DL-GESC to the SL-GESC, there is a considerable improvement when we move from $s/d = 2$ to $s/d = 3$, while the change from $s/d = 3$ to $s/d = 4$ is marginal.

The FEM results for a 100 mm column with various s/d ratios are discussed in detail below, as shown in Figure 7. It has been observed that DL-GESC greatly outperforms OSC and SL-GESC in resisting the vertical load. Similar patterns are observed for columns with diameters of 50, 75, 125, and 150 mm; hence, the prior finding holds true for all of the column diameters stated.

6.2. Effect of Encasement. As seen in Figure 8, the encasement significantly increased the capacity of soft soil to withstand loads after being reinforced with a stone column. The results of FEM for various s/d ratios and variations in diameter are displayed in the accompanying graphs, respectively. For the DL-GESC, it can be seen that the load-carrying capacity significantly improves as the ordinary stone column diameter increases. Results from the experimental study [26] and numerical study [47] also indicates, compared to ordinary stone columns, encased stone columns have a substantially higher stress concentration. Overall, there was an improvement of 15–25% from DL-GESC to SL-GESC. There has been an increase in load-carrying capacity, with $s/d = 3$ producing the best results and accommodating all diameter variations.

The axial load-carrying capacity for various stone column diameters with varying s/d ratios is detailed in Table 5 and well depicted in Figure 6(b); when compared to an ordinary stone column, the axial load-carrying capability of column improves. According to the results of the FEM

TABLE 3: Properties of the materials used for PLAXIS 3D.

Parameters	Properties	
	Clay	Stone material
Poisson's ratio (μ)	0.4	0.3
Shear strength, cu (kPa)	14	0
Modulus of elasticity (kPa)	4000	45,000
Angle of internal friction (ϕ)	0	38°
Dilatancy angle (ψ)	0	8°
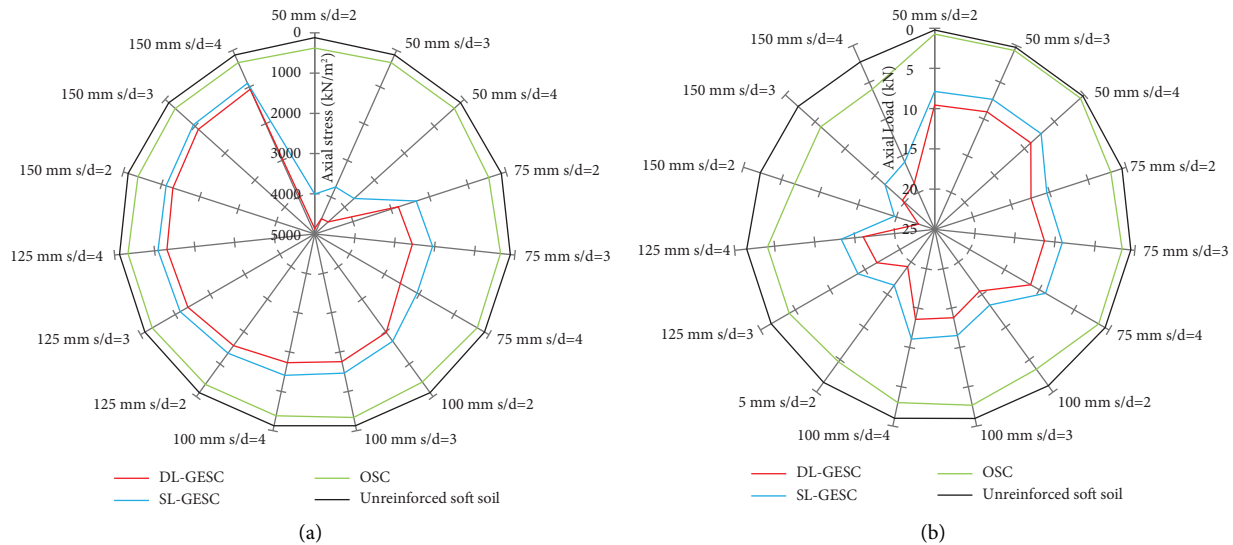
FIGURE 6: Effect of spacing on a single column: (a) axial stress (kN/m^2) and (b) load (kN).

TABLE 4: Improvement in DL-GESC compared to SL-GESC.

s/d	Improvement (%)				
	50 mm	75 mm	100 mm	125 mm	150 mm
2	21.49	19.95	15.97	17.44	15.95
3	23.18	24.72	19.63	19.51	17.61
4	23.66	23.25	22.71	20.55	18.37

study, in comparison to the ordinary stone column, an improvement of 2.15–12.75 times for DL-GESC and 1.6–10 times for SL-GESC has been observed. There has been a rise in axial load capacity of DL-GESC for all the considered cases for various diameters, it has been observed that, with spacing to diameter ratio 3 yielding the optimum results for load-bearing capacity if compared with spacing to diameter ratio of 2 and 4.

The dual-layered, geosynthetic-encased column outperforms the stone column installed in soft soil by a significant margin. The axial stress decreases as the diameter of the stone column grows for varied s/d ratios, as shown in Figure 6(a), illustrating that the load-carrying capacity of the soil increases as a direct result of this modification.

6.3. Effect of Stone Column Diameter on Improvement Ratio (I.R.). The FEM modelling results were analysed and

reported as a bearing capacity improvement ratio (q_r/q_u), where q_r is the vertical stress of reinforced soil at a settlement of 50 mm and q_u is the vertical stress of unreinforced soil at the same settlement. Figure 9 shows the trendlines of the DL-GESC, SL-GESC, and OSC for varying diameters and s/d ratios, and it was observed that when compared to unreinforced soil, the load-carrying capacity of ordinary stone column improve 2.6–3.7 times, for SL-GESC improves 7–33.5 times, and for DL-GESC improves 8.5–40.8 times.

6.4. Failure Mechanism. The length of the column has a crucial role in the failure mechanism of a single stone column loaded across its region. In situations where end-bearing and floating columns are utilized and the length of the column exceeds the critical length, which is estimated to be approximately four times the diameter, the column may experience collapse due to bulging [48]. Similar observations

(a)

(b)

(c)
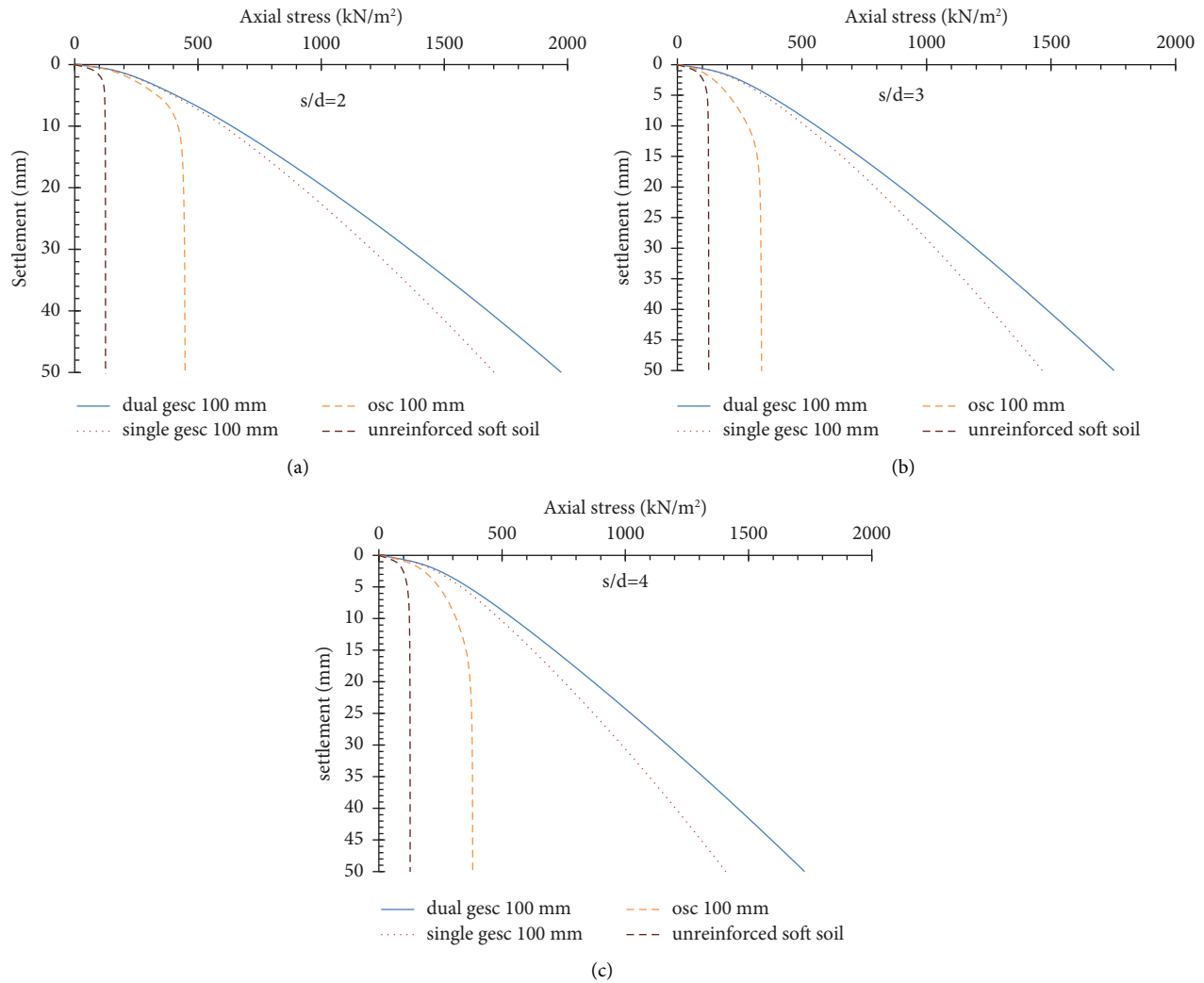
FIGURE 7: Axial stress vs. settlement of single column: (a) $s/d = 2$, (b) $s/d = 3$, and (c) $s/d = 4$.

have also been made in the current study. The outcomes of this numerical study demonstrated that an ordinary stone column without an encasing was bulging along its periphery. Figure 10 depicts the bulging failure, and it can be noticed that there was less bulging in the case of the provided encasement and also that the encasement material did not rupture. While the external reinforcement, in the form of encasing the column in a geofabric, will prevent the column from collapsing by bulging or shearing; it will not let the column to dilate and hence raise the in situ stresses [49]. When compared to SL-

GESC, DL-GESC lessens bulging, which reflects the goal of the current study. If this encasement arrangement is maintained, the stone column will not fail due to bulging under various loading circumstances. The analysis of stone columns with varying diameters and s/d ratios revealed that the load-carrying capacity of OSC increases for single-layered and dual-layered encasement, which can be seen from Table 5. From observations, it has been deduced that the insertion of an encasement into an ordinary stone column increases its capacity to withstand several loading conditions.
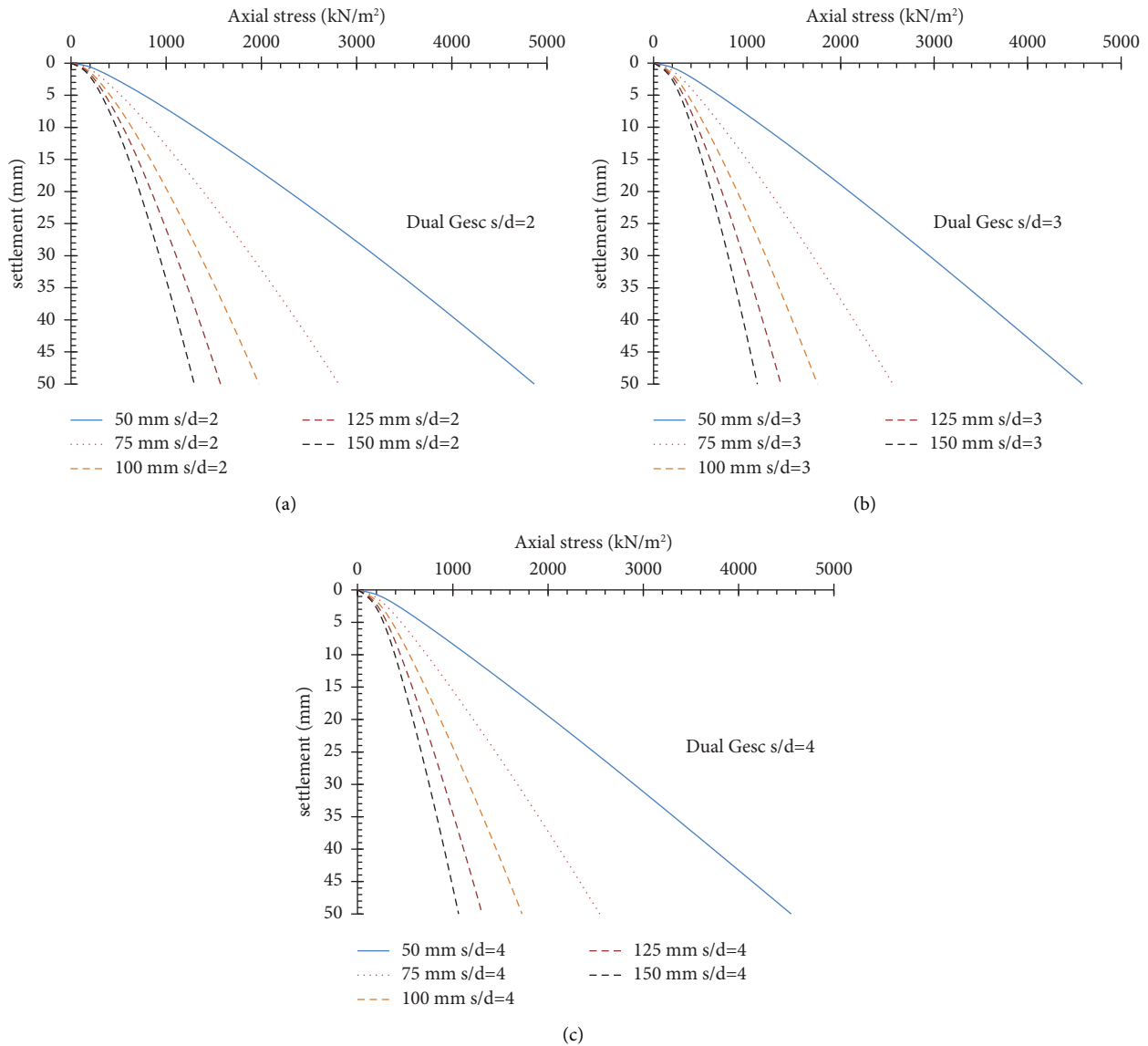
Figure 8: Effect of encasement on axial stress vs. settlement for single column of various diameter of stone column: (a) $s/d = 2$, (b) $s/d = 3$, and (c) $s/d = 4$.

Table 5: Improvement in DL-GESC and SL-GESC compared to OSC.

(mm)		Axial load (kN)			Improvement (%)	
	s/d ratio	OSC	SL-GESC	DL-GESC	SL-GESC	DL-GESC
	2	0.74	7.87	9.56	963.51	1191.89
50	3	0.66	7.31	9.00	1007.58	1263.64
	4	0.65	7.23	8.94	1012.31	1275.38
	2	1.99	10.36	12.43	420.60	524.62
75	3	1.58	9.07	11.31	474.05	615.82
	4	1.49	9.11	11.23	511.41	653.69
	2	3.52	13.37	15.51	279.83	340.63
100	3	2.65	11.51	13.77	334.34	419.62
	4	2.99	11.06	13.57	269.90	353.85
	2	4.64	16.41	19.27	253.66	315.30
125	3	4.12	13.98	16.71	239.32	305.58
	4	4.11	13.32	16.06	224.09	290.75
	2	6.70	19.73	22.88	194.48	241.49
150	3	5.94	16.67	19.61	180.64	230.13
	4	5.94	15.84	18.75	166.67	215.66
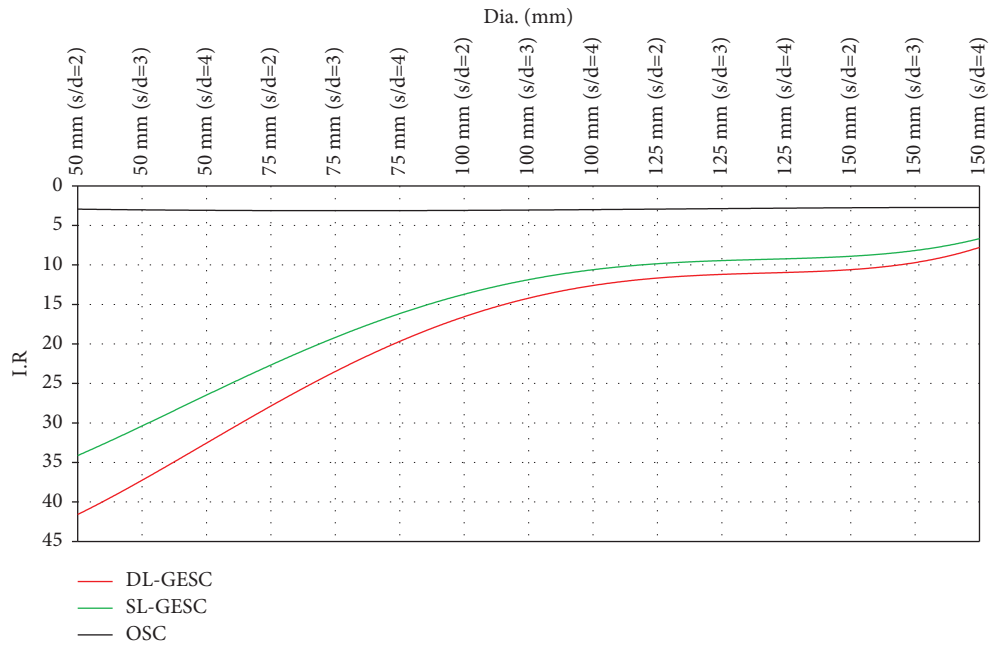
Figure 9: Trendline of I.R. of single column.

(a)   (b)
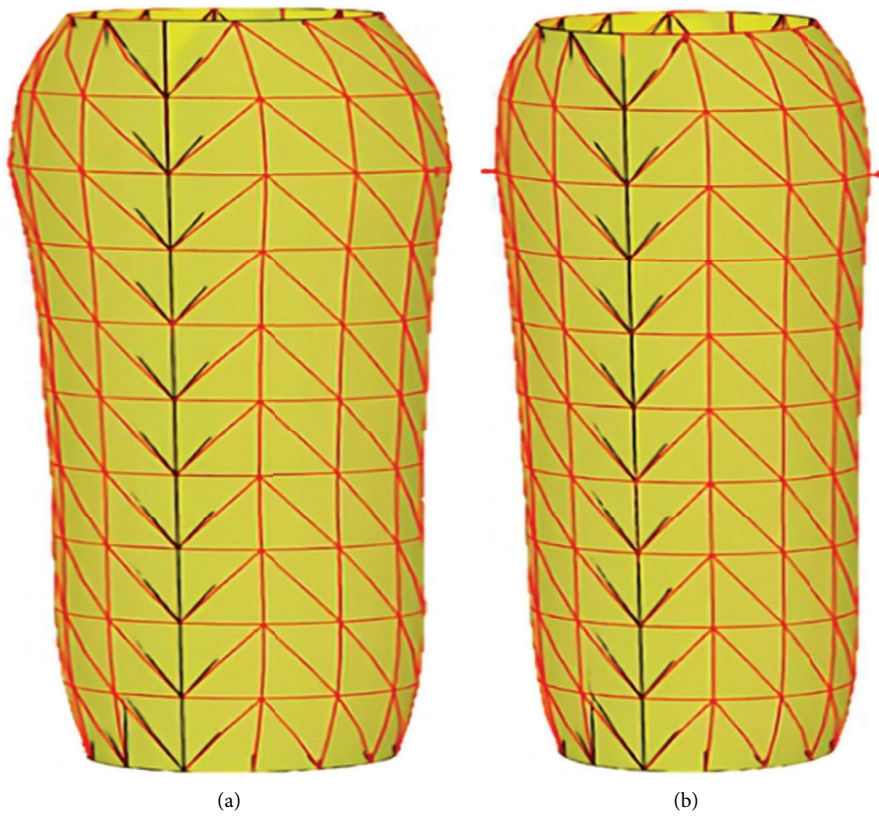
Figure 10: Effect of bulging: (a) SL-GESC and (b) DL-GESC.

7. Conclusions

(i) The spacing-to-diameter ratio influences the axial stresses that occur within the body of the stone column; as the ratio increases, so does the load-carrying capacity of the system, with a spacing-to-diameter ratio of 3 being optimal.

(ii) Insertion of the OSC results in higher axial load values at lower settlement values when compared to the clay bed, an enhancement of 2.5 to 3 times is observed for various cases of the stone column diameter; a higher improvement is observed for the larger diameter.

(iii) The encasement of the stone column resists the bulging of the stone column body, which helps in increasing the load-carrying capacity, in cases where single-layered encasement is used, the load-carrying capacity increases by 1.6–10 times in comparison to ordinary stone column cases.

(iv) Introducing an additional layer of encasement into the body of stone column assists in preventing bulging and promotes the confinement of the stone material. Dual-layered encasements provide a 15–25% greater mobilisation of stress than single-layered encasements.

(v) The analysis of stone columns with varying diameters and s/d ratios showed that DL-GESC exhibits less bulging than SL-GESC, indicating that the load-carrying capacity of OSC is enhanced in cases where dual encasement is provided under various loading conditions.

Data Availability

The authors have agreed to provide the information used and/or analysed during the current work upon reasonable request.

Conflicts of Interest

The authors declare that they have no conflicts of interest.

References

[1] R. Ghanti and A. Kashliwal, *Ground Improvement Techniques – with a Focused Study on Stone Columns*, vol. 30, Dura Build Care PVT LTD, Patna, Bihar, 2008.

[2] B. A. McCabe, G. J. Nimmons, and D. Egan, "A review of field performance of stone columns in soft soils," *Proceedings of the Institution of Civil Engineers - Geotechnical Engineering*, vol. 162, no. 6, pp. 323–334, 2009.

[3] C. J. Serridge, "Some applications of ground improvement techniques in the urban environment," *Iaeg2006*, vol. 296, pp. 1–14, 2006.

[4] J. M. O. Hughes, N. J. Withers, and D. A. Greenwood, "A field trial of the reinforcing effect of a stone column in soil," *Géotechnique*, vol. 25, no. 1, pp. 31–44, 1975.

[5] M. C. Alfaro, A. S. Balasubramaniam, D. Bergado, and J. C. Chai, *Improvement Techniques of Soft Ground in Subsiding and Lowland Environment*, Taylor & Francis, Milton Park, Oxfordshire, 1994.

[6] P. Andreou, W. Frikha, R. Frank, J. Canou, V. Papadopoulos, and J. C. Dupla, "Experimental study on sand and gravel columns in clay," *Proceedings of the Institution of Civil Engineers - Ground Improvement*, vol. 161, no. 4, pp. 189–198, 2008.

[7] W. F. Van Impe, *Soil Improvement Techniques and Their Evolution*, Taylor & Francis, Milton Park, Oxfordshire, 1989.

[8] D. T. Bergado and C. Teerawattanasuk, "2D and 3D numerical simulations of reinforced embankments on soft ground," *Geotextiles and Geomembranes*, vol. 26, no. 1, pp. 39–55, 2008.

[9] R. P. Chen, Y. M. Chen, J. Han, and Z. Z. Xu, "A theoretical solution for pile-supported embankments on soft soils under one-dimensional compression," *Canadian Geotechnical Journal*, vol. 45, no. 5, pp. 611–623, 2008.

[10] A. Lunzhu Li and R. Kerry Rowe, "Effects of viscous behavior of geosynthetic reinforcement and foundation soils on the performance of reinforced embankments," *Geotextiles and Geomembranes*, vol. 26, no. 4, pp. 317–334, 2008.

[11] E. Fathi and R. Mohtasham, *Numerical Analysis of the Reinforced Stone Column by Geosynthetic on Stability of Embankment*, Avestia Publ, Orléans, ON, Canada, 2016.

[12] D. Alexiew, D. Brokemper, and S. Lothspeich, "Geotextile Encased Columns (GEC): Load Capacity," *Geotextile Selection and Pre-Design Graphs*, vol. 23, pp. 1–14, 2005.

[13] D. Lee, C. Yoo, and S. Park, *Model tests for analysis of load carrying capacity of geogrid encased stone column*, OnePetro, Richardson, TX, USA, 2007.

[14] D. Lee, C. Yoo, S. Park, and S. Jung, "Field load tests of geogrid encased stone columns in soft ground," in *Proceedings of the International Offshore and Polar Engineering Conference*, vol. 8, pp. 521–524, Danvers, MA, USA, May 2008.

[15] S. Murugesan and K. Rajagopal, "Geosynthetic-encased stone columns: numerical evaluation," *Geotextiles and Geomembranes*, vol. 24, no. 6, pp. 349–358, 2006.

[16] M. Raithel and H. G. Kempfert, *Calculation models for dam foundations with geotextile coated sand columns*, OnePetro, Richardson, TX, USA, 2000.

[17] J. Gniel and A. Bouazza, "Improvement of soft soils using geogrid encased stone columns," *Geotextiles and Geomembranes*, vol. 27, no. 3, pp. 167–175, 2009.

[18] P. Debnath and A. K. Dey, "Bearing capacity of geogrid reinforced sand over encased stone columns in soft clay," *Geotextiles and Geomembranes*, vol. 45, no. 6, pp. 653–664, 2017.

[19] K. Tilva Vikunj, "Study on geosynthetic reinforced stone column with soft & stiff clay," *International Research Journal of Engineering and Technology*, vol. 4, no. 7, pp. 593–595, 2017.

[20] K. Ali, J. T. Shahu, and K. G. Sharma, "Model tests on geosynthetic-reinforced stone columns: a comparative study," *Geosynthetics International*, vol. 19, no. 4, pp. 292–305, 2012.

[21] K. Ali, J. T. Shahu, and K. G. Sharma, "Model tests on single and groups of stone columns with different geosynthetic reinforcement arrangement," *Geosynthetics International*, vol. 21, no. 2, pp. 103–118, 2014.

[22] S. K. Dash and M. C. Bora, "Improved performance of soft clay foundations using stone columns and geocell-sand mattress," *Geotextiles and Geomembranes*, vol. 41, pp. 26–35, 2013.

[23] M. Khabbazian, V. N. Kaliakin, and C. L. Meehan, "Numerical study of the effect of geosynthetic encasement on the behaviour of granular columns," *Geosynthetics International*, vol. 17, no. 3, pp. 132–143, 2010.

[24] S. R. Lo, R. Zhang, and J. Mak, "Geosynthetic-encased stone columns in soft clay: a numerical study," *Geotextiles and Geomembranes*, vol. 28, no. 3, pp. 292–302, 2010.

[25] S. Murugesan and K. Rajagopal, "Model tests on geosynthetic-encased stone columns," *Geosynthetics International*, vol. 14, no. 6, pp. 346–354, 2007.

[26] S. Murugesan and K. Rajagopal, "Studies on the behavior of single and group of geosynthetic encased stone columns," *Journal of Geotechnical and Geoenvironmental Engineering*, vol. 136, no. 1, pp. 129–139, 2010.

[27] B. Pulko, B. Majes, and J. Logar, "Geosynthetic-encased stone columns: analytical calculation model," *Geotextiles and Geomembranes*, vol. 29, no. 1, pp. 29–39, 2011.

[28] P. A. Suriya, P. Subathra, P. Gopiprasath, and V. Lakshminarayana, "Stabilization of soft soil using stone column – the review," *Journal of Industrial Pollution Control*, vol. 33, no. 1, pp. 1214–1217, 2017.

[29] C. Yoo and S. B. Kim, "Numerical modeling of geosynthetic-encased stone column-reinforced ground," *Geosynthetics International*, vol. 16, no. 3, pp. 116–126, 2009.

[30] T. Ayadat, A. Hanna, and M. Etezad, "Failure process of Stone columns in Collapsible soils," *International Journal of Engineering, Transactions B: Applications*, vol. 21, no. 2, pp. 135–142, 2008.

[31] M. Ghazavi, A. Ehsani Yamchi, and J. Nazari Afshar, "Bearing capacity of horizontally layered geosynthetic reinforced stone columns," *Geotextiles and Geomembranes*, vol. 46, no. 3, pp. 312–318, 2018.

[32] S. Siva Gowri Prasad and P. V. V. Satyanarayana, "Improvement of soft soil performance using stone columns improved with circular geogrid discs," *Indian Journal of Science and Technology*, vol. 9, no. 30, 2016.

[33] S. T. Kadhim, R. L. Parsons, and J. Han, "Three-dimensional numerical analysis of individual geotextile-encased sand columns with surrounding loose sand," *Geotextiles and Geomembranes*, vol. 46, no. 6, pp. 836–847, 2018.

[34] M. Miranda, J. Fernández-Ruiz, and J. Castro, "Critical length of encased stone columns," *Geotextiles and Geomembranes*, vol. 49, no. 5, pp. 1312–1323, 2021.

[35] J. Gao, Y. Zhang, C. Wang, and C. Yuan, "Behavior characteristics of geosynthetic-encased stone column under cyclic loading," *Transportation Geotechnics*, vol. 28, Article ID 100554, 2020.

[36] A. Jaiswal and R. Kumar, "Finite element analysis of granular column for various encasement conditions subjected to shear load," *Geomechanics Engeeniring*, vol. 29, no. 6, pp. 645–655, 2022.

[37] M. Hasan and N. K. Samadhiya, "Experimental and numerical analysis of geosynthetic-reinforced floating granular piles in soft clays," *International Journal of Geosynthetics and Ground Engineering*, vol. 2, no. 3, p. 22, 2016.

[38] J. F. Chen, L. Y. Li, J. F. Xue, and S. Z. Feng, "Failure mechanism of geosynthetic-encased stone columns in soft soils under embankment," *Geotextiles and Geomembranes*, vol. 43, no. 5, pp. 424–431, 2015.

[39] P. Mohanty and M. Samanta, "Experimental and numerical studies on response of the stone column in layered soil," *International Journal of Geosynthetics and Ground Engineering*, vol. 1, no. 3, pp. 27–14, 2015.

[40] A. P. Ambily and S. R. Gandhi, "Behavior of stone columns based on experimental and FEM analysis," *Journal of Geotechnical and Geoenvironmental Engineering*, vol. 133, no. 4, pp. 405–415, 2007.

[41] S. Mitra and B. C. Chattopadhyay, "Stone columns and design limitations," in *Proceedings of the Indian Geotechnical Conference*, pp. 201–205, Calcutta, India, June 1999.

[42] M. Ghazavi and J. Nazari Afshar, "Bearing capacity of geosynthetic encased stone columns," *Geotextiles and Geomembranes*, vol. 38, pp. 26–36, 2013.

[43] M. S. S. Almeida, I. Hosseinpour, M. Riccio, and D. Alexiew, "Behavior of geotextile-encased granular columns supporting test embankment on soft deposit," *Journal of Geotechnical and Geoenvironmental Engineering*, vol. 141, no. 3, 2015.

[44] M. Hasan and N. K. Samadhiya, "Performance of geosynthetic-reinforced granular piles in soft clays: model tests and numerical analysis," *Computers and Geotechnics*, vol. 87, pp. 178–187, 2017.

[45] R. Jamshidi Chenari, M. Karimpour Fard, M. Jamshidi Chenari, and J. Shamsi Sosahab, "Physical and numerical modeling of stone column behavior in loose sand," *International Journal of Civil Engineering*, vol. 17, no. 2, pp. 231–244, 2019.

[46] L. A. Dar and M. Y. Shah, "Three dimensional numerical study on behavior of geosynthetic encased stone column placed in soft soil," *Geotechnical & Geological Engineering*, vol. 39, no. 3, pp. 1901–1922, 2021.

[47] C. Yoo, "Performance of geosynthetic-encased stone columns in embankment construction: numerical investigation," *Journal of Geotechnical and Geoenvironmental Engineering*, vol. 136, no. 8, pp. 1148–1160, 2010.

[48] Civil Planets, "Design and construction for ground improvement-Guidelines," *Burn. Indian Standard*, vol. 15284, pp. 1–20, 2003.

[49] T. Ayadat, A. M. Hanna, and A. Hamitouche, "Soil improvement by internally reinforced stone columns," *Proceedings of the Institution of Civil Engineers - Ground Improvement*, vol. 161, no. 2, pp. 55–63, 2008.

Hindawi

Research Article

Shrinkage Compensation Technology of Concrete Filled Steel Tubular Structure of Large Cross-Sea Bridge

Yi Zhao and Xiao Wu (ID)

College of Water and Architectural Engineering, Shihezi University, Shihezi 832003, China

Correspondence should be addressed to Xiao Wu; wuxiao04520030@163.com

In view of the poor accuracy and unsatisfactory effect of shrinkage compensation for concrete-filled steel tubular structures of large cross-sea bridge (CSTS-LCSB), a new shrinkage compensation technology for CSTS-LCSB is proposed. The shrinkage mechanism of CSTS-LCSB is analyzed, including plastic shrinkage, dry shrinkage, autogenous shrinkage, and carbonation shrinkage. The proportion of dry shrinkage and autogenous shrinkage in ordinary concrete and high-strength concrete is determined. The CSTS-LCSB has different shrinkage forms in different environments, and the shrinkage strain state of CSTS-LCSB in different environments is calculated according to the difference. The shrinkage area of the concrete structure is determined, and the expansion agent is used to compensate for the shrinkage area of CSTS-LCSB. The experimental results show that the proposed compensation technology has a good effect on shrinkage compensation and has certain feasibility.

1. Introduction

As the main building material, concrete is easy to crack in the process of construction and use because of its low tensile strength and small ultimate tensile deformation. Once cracks occur in the concrete structure, it will be difficult for the concrete structure to defend against the erosion of harmful media. The degree of steel corrosion and concrete carbonization will be deepened. Furthermore, the durability of the structure and the functional use of the structure will also be affected. The reinforced concrete-filled steel tube is applied to the large-scalesea-crossing bridge. There are two kinds of cracks in concrete-filled steel tubular structures of large cross-sea bridge (CSTS-LCSB), which are load cracks and nonload cracks. The load cracks caused by the external load can be avoided and controlled by more mature structural design theory, so the load cracks account for about 20% of the total cracks, while the nonload cracks caused by uneven settlement, temperature change, and concrete shrinkage account for about 80%. The direct reason is that the tensile stress (tensile strain) produced by the constraint of the concrete itself or structure deformation exceeds the ultimate

tensile strength (ultimate tensile strain) that the concrete material itself can bear at this age [1, 2]. Up to now, the analysis of the temperature field, temperature stress field, and temperature control design method of CSTS-LCSB are relatively mature. Therefore, the cracks caused by shrinkage deformation of concrete account for the vast majority of nonload cracks.

The main factors affecting the shrinkage cracking of CSTS-LCSB are material stiffness, toughness, shrinkage rate, shrinkage, creep relaxation, and restraint degree [3]. In order to meet the requirements of high fluidity and low energy consumption, the concrete used in modern buildings appropriately reduce the proportion of coarse aggregate in the material ratio and increase the proportion of cement and fine aggregate. Therefore, the control of concrete shrinkage cracks is more complicated. In particular, the problem of early shrinkage cracking has become a common problem in contemporary concrete structure engineering. In addition, with the development of social economy and the deepening of urban construction, the forms of buildings have become more complex and diversified, and more super-long structures are designed to meet various functional

requirements [4]. However, the causes of concrete shrinkage and cracking are complex and uncertain. At present, there is no mature and complete design theory and calculation method to predict and control. It only depends on experience to take relevant measures from the design and construction to avoid, and it is often due to a variety of human or material, environmental, and other objective reasons. Liu et al. introduce a multifield (hydro-thermo-hygro-constraint) coupling model with the hydration degree of cementitious materials as the basic state parameter to estimate the shrinkage cracking risk of hardening concrete under coupling effects, and a design process based on the theoretical model and key technologies is proposed to control the cracking risk index below the threshold value [5]. It is difficult to effectively prevent shrinkage cracks.

In order to improve the shrinkage compensation effect and accuracy of CSTS-LCSB, a new shrinkage compensation method for CSTS-LCSB is proposed in this paper. The technical route is as follows:

Step 1: We analyze its shrinkage mechanism, including plastic shrinkage, drying shrinkage, autogenous shrinkage, and carbonation shrinkage, and determine the proportion of drying shrinkage and autogenous shrinkage in ordinary concrete and high-strength concrete.

Step 2: By determining that the shrinkage of it is different in different environments, the shrinkage strain state of concrete-filled steel tubular construction of large-scale sea cross in different environments is calculated.

Step 3: We determine the shrinkage area of the concrete structure and use the expansion agent to complete the compensation for the shrinkage area of the large cross-sea bridge.

2. Literature Review

How to improve the shrinkage compensation of CSTS-LCSB has become a hot issue in this field. Relevant researchers have carried out a lot of research and achieved certain results [6].

Hasholt et al. proposed research, which was to determine the appropriate time at which shrinkage initiates at an early age for various concrete mixtures under field conditions. Besides, a new approach to determine shrinkage initiation at early age depending on the strains of the free and restrained shrinkage was used in this research [7]. The performance research and shrinkage control method of high-strength concrete for super-high bridge towers are proposed to compensate for the shrinkage [8]. In order to study the influence of zeolite gravel, fly ash ceramic sand and super-absorbent resin (SAP) internal curing materials on the performance of C60 high-strength concrete, the influence of single and multiple internal curing materials on the compressive strength, internal relative humidity, and free shrinkage of concrete was analyzed. The results of this study can provide a reference for the application of mass high-

strength concrete, but there are some deficiencies in its compensation effect, which need further improvement.

An analysis method for crack resistance of shrinkage compensating concrete impervious panels during construction is proposed by Cai et al. [9]. In order to study the causes of impervious panel cracking during construction, a calculation model was established. In addition, the real-time numerical analysis of the temperature field and stress field of shrinkage compensating concrete impervious panel during construction was carried out. The stress distribution of impervious panels under different thermal insulation measures was obtained, and the causes of cracks were analyzed. During the construction period, the temperature difference between the inside and outside of the panel concrete was large. When the temperature reached 4 d, the temperature stress at the edge of the panel reached the peak value, which was higher than that of the corresponding age concrete. It is easy to produce cracks. When adopting the insulation measures, the temperature gradient caused by the difference in temperature between inside and outside can be greatly reduced [10]. The temperature stress of the 4 d age concrete can be reduced by 29% of the 10 mm polystyrene foam insulation plastic board. It can effectively improve the anticrack performance of the impervious panel, but the degree of crack compensation needs to be further expanded.

In addition, reference [11] took the large-diameterconcrete-filled steel tubular bridge tower structure of a river crossing project as an example and evaluated the risk of structural interface debonding and concrete cracking under different expansion performance curves. The temperature change deformation process and strength of concrete in the pipe under different calcium magnesium compound expansion agent contents were further tested and studied. Although the test provides a high-performance expansion agent that can prepare nonshrinkage high crack-resistant concrete, the shrinkage strain state of concrete-filled steel tubular bridge under different environmental factors was not analyzed and discussed, and the adaptability was unknown.

In reference [12], the effects of the composition system of cementitious materials and the strength of aggregate parent rock on the workability and mechanical properties of concrete were studied. The effects of the amount of the expansion agent on the volume stability of concrete were explored, and the microstructure of a high-strengthconcrete-filled steel tube was analyzed by SEM. High-strength concrete with excellent self-compacting shrinkage compensation can be prepared by mixing silica fume, fly ash beads, and an appropriate amount of expansion agent with basalt macadam. It has been successfully applied to the composite structure pier of the Jinyanghe Bridge in Liangshan, Sichuan. However, it focuses on solving the problem of the high-strengthconcrete-filled steel tubular composite structure with high cast-in-place concrete, large fluidity, and low shrinkage. It does not analyze the shrinkage strain state under different environments, and the shrinkage compensation effect needs to be further improved.

3. Methodology

3.1. Shrinkage Mechanism Analysis of CSTS-LCSB. The concrete-filled steel tube of large-scalecross-sea bridge gradually hardens in the air, and the volume shrinks. The length shrinkage deformation of concrete can reach $(300–600) * 10^6$ after decades and even $(800–1000) * 10^6$ under adverse conditions. However, if the concrete is put into the water, the volume will expand, and the maximum length deformation can reach $150 * 10^6$. The shrinkage of concrete has the following different reasons and mechanisms, and the shrinkage deformation is the superposition of various shrinkage states [13]. It mainly includes the following aspects.

3.1.1. Plastic Shrinkage. During the period from pouring to the final setting of concrete-filled steel tube (generally about 4–15 hours), the hydration reaction of cement is intense, the molecular chain is gradually formed, and there are phenomena such as bleeding, rapid evaporation of water, and uneven settlement between aggregate and cement slurry [14]. Because these phenomena occur in the plastic stage before the final setting of concrete, it is called plastic shrinkage. Plastic shrinkage can be subdivided into three types: dehydration condensation, chemical shrinkage reduction, and settlement shrinkage [15–18]. The amount of plastic shrinkage can reach about 1%, which will cause irregular surface cracks on the upper surface of the concrete, especially in the parts with poor maintenance, often distributed along the reinforcement [19].

3.1.2. Drying Shrinkage. Shrinkage of concrete for Large Cross Harbour Bridge after the cessation of curing is lost in unsaturated air and the adsorptive water of internal pores and gel holes. The reason is that the internal moisture of concrete-filled steel tube disappears, but the loss of free water at the beginning of drying does not cause concrete shrinkage; the disappearance of internal adsorbed water is the main influence factor [20]. The loss of adsorbed water in the micropore produces capillary negative pressure in the pore and promotes the formation of the gas-liquid meniscus, which causes tensile stress in the pore wall and causes the shrinkage of cement paste.

3.1.3. Self (Body) Shrinkage. Volume change of concrete-filled steel tube of large-scale cross sea bridge has no moisture exchange with surrounding environment. It is the self-drying of concrete in the process of cement hydration due to no external water supply or the speed of external water migrating into the system through pores is less than the speed of hydration water consumption [21]. The cause is that the water in the pores becomes unsaturated, forming a gas-liquid meniscus and making the pores under negative pressure. The volume of cement hydrate is smaller than that of cement and water involved in the hydration reaction, which is an inherent shrinkage caused by the cement hydration reaction. When the water-cement ratio of concrete is small, the self-drying phenomenon generally occurs in the pores, which is manifested as the macro self-shrinkage. When the water-cement ratio is large, the self-drying phenomenon only occurs in the local pores, and the self-shrinkage can be ignored in the macro [22].

3.1.4. Carbonation Shrinkage. The volume shrinkage is caused by the chemical reaction between cement hydrate in concrete and CO_2 in the air under appropriate relative humidity. There are different alkalinity of various hydrates, different amounts of crystal water and water molecules, and different sizes of carbonation shrinkage. The main influencing factors are the dissolution of $Ca(OH)_2$ crystal and the deposition of $CaCO_3$ in cement hydrates [23]. The carbonation rate depends on the water content of concrete, environmental humidity and CO_2 concentration, and the component size.

Both drying shrinkage and self-shrinkage of CSTS-LCSB are caused by capillary stress, splitting tension, and other changes caused by water loss, but the mechanism of water loss is different. The former is caused by internal water being consumed by a hydration reaction, while the latter is caused by water diffusing into the external environment [24]. The drying shrinkage starts from the moment when the concrete is exposed to the atmosphere and continues through the whole life cycle of the concrete structure. The shrinkage starts from the outside to the inside, which accounts for the largest proportion of the total shrinkage. Autogenous shrinkage occurs uniformly in the concrete without water exchange with the outside. It is the result of cement hydration. Although it is earlier than drying shrinkage, its value is less than drying shrinkage [25–27]. Therefore, for ordinary concrete, it is mainly drying shrinkage. For high-strength concrete or high-performance concrete with a low water cement ratio, besides drying shrinkage, autogenous shrinkage cannot be ignored. The proportion relationship between drying shrinkage and autogenous shrinkage in ordinary concrete and high-strength concrete is shown in Figure 1. It can be seen that drying shrinkage is the most important component of concrete shrinkage, which cannot be avoided in any concrete structure shrinkage problem. Correctly distinguishing different types of shrinkage helps take corresponding compensation control measures [28].

3.2. Shrinkage Analysis of CSTS-LCSB. In order to realize the shrinkage compensation technology of CSTS-LCSB, it is necessary to analyze its shrinkage of it. There are some differences in the forms of shrinkage of concrete-filled steel tubular constructions of large-scale sea cross in different environments [29]. The shrinkage strain of that in the natural environment can be expressed as follows:

$$\varepsilon_t = \varepsilon_{\Delta T} + \varepsilon_{sh} + \varepsilon_{as} + \varepsilon_{ds}. \tag{1}$$

In the formula, $\varepsilon_{\Delta T}$ represents the contraction strain caused by temperature changes, ε_{as} represents the self-shrinkage strain of large sea bridge, ε_{ds} represents dry shrinkage strain of large sea bridge, and ε_{sh} represents the sum of self-shrinkage and dry shrinkage strain of concrete.
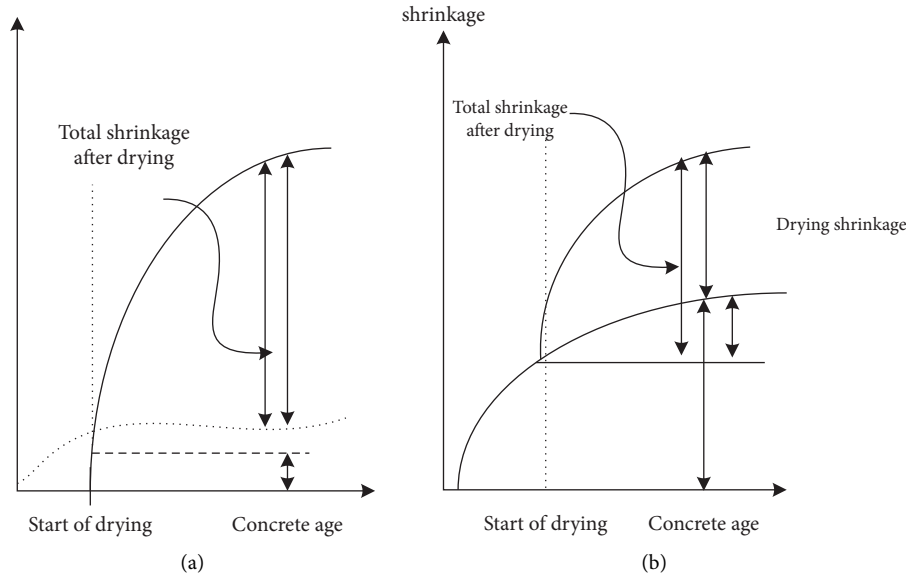
FIGURE 1: The proportion of dry shrinkage and autogenous shrinkage in ordinary concrete and high-strength concrete.

In the actual application environment, the concrete pipe shrinkage of large sea cross is mainly affected by relative humidity, and the shrinkage caused by temperature is as follows:

$$\varepsilon_{\Delta T} = \mu \times \Delta T = 1 \times 10^{-5} \times \Delta T. \tag{2}$$

In the formula, μ represents the linear expansion coefficient of concrete over large sea bridge and ΔT represents the temperature increment.

When the CSTS-LCSB hardens in the air, the phenomenon of volume reduction is shrinkage. When analyzing the structural stress, not only the temperature change of the structure should be considered, but also the influence of shrinkage on its structure should be analyzed [30]. The composition of concrete-filled steel tube is also the key factor affecting its strain value.

$$\varepsilon_y(t) = \varepsilon_y^0 \times m_1 \times m_2 \times m_n \left(1 - e^{-bt}\right), \tag{3}$$

In the formula, $\varepsilon_y(t)$ represents the strain value of the concrete shrinkage, b represents the construction experience factor, ε_y^0 represents the contraction of the normal limit, and $m_1/m_2/m_n$ represent different correction factors.

3.3. Concrete Creep and Stress Relaxation of Large Sea Bridge.
Creep of CSTS-LCSB refers to the phenomenon that the deformation of the concrete structure increases with time under continuous load. There are two kinds of creep in super-long structure: one is creep deformation, that is, the stress does not change, and the strain increases with the increase of holding time. The other is stress relaxation; that is, the stress decreases with time when the strain is constant. The stress relaxation caused by the concrete creep effect on concrete structures is also an important factor of structural deformation, so the phenomenon of stress relaxation needs more attention [31]. Creep deformation and stress relaxation

of structural materials are very important for studying the stress state caused by the deformation of super-long structures. The calculation theory of creep is complex. Linear creep theory is used for super-long concrete and reinforced concrete with low reinforcement ratios. The process of engineering simplified calculation is to calculate the elastic stress first and then multiply it with the relaxation coefficient to get the loose stress.

The relaxation coefficient $H(t, \tau)$ is related to the age and duration of the constraint stress, and the formula is expressed as follows:

$$H(t, \tau) = \frac{\sigma^*(t, \tau)}{\sigma_x(\tau)}. \tag{4}$$

In the formula, $\sigma^*(t, \tau)/\sigma_x(\tau)$ represents the relaxation stress persistence value and $\sigma_x(\tau)$ represents the elastic stress of the instantaneous loading.

On this basis, the binding force around it is also considered. When the CSTS-LCSB contacts along the water surface, the horizontal relative displacement will produce a certain shear stress on the contact surface due to friction and bond resistance [32]. In this case, the point shear stress on the structure can be assumed to be proportional to the horizontal displacement of the point.

$$\tau_x = -C_x \times \delta(x). \tag{5}$$

In the formula, τ_x represents the friction resistance between the peripheral binding force and the concrete, $-C_x$ represents the horizontal resistance coefficient, and $\delta(x)$ represents the distance of the horizontal displacement.

The load transfers of concrete and surrounding constraints of a large sea bridge are shown in Figure 2.

3.4. The Shrinkage Compensation Technology of Concrete Steel Pipe Structure of Large Cross-Sea Bridge.
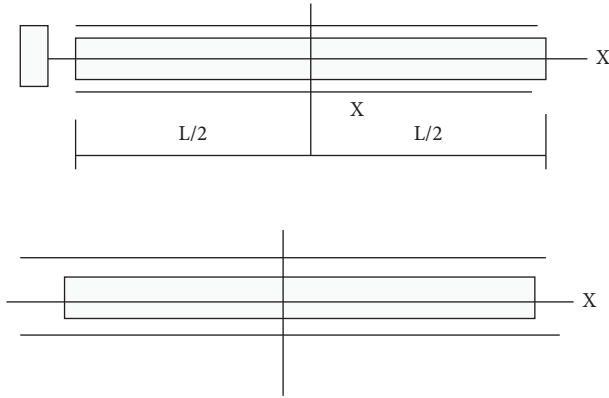Based on the shrinkage, creep, and stress relaxation of the large span

FIGURE 2: Schematic diagram of load transfer of steel tubular concrete and surrounding constraints of the large cross-sea bridge.

bridge mentioned previously, the shrinkage of the concrete-filled steel tube structure is compensated. Generally, the expansion agent can be used to compensate for the shrinkage structure of the large-scale bridge. Before compensation, the area to be compensated should be determined first. In this paper, the area to be compensated is determined, and its parameters are calculated.

It is assumed that there is an indirect relationship between the compressive strength and the shrinkage area of concrete-filled steel tubular structure as follows:

$$y(t) = r' \frac{t}{b + ct}. \tag{6}$$

In the formula, $y(t)$ represents the mean compressive strength at t moment, r' represents the mean value of the compressive strength, and b/c represents common coefficients.

According to the compressive strength of the shrinkage area of the concrete-filled steel tubular structure determined

previously, the shrinkage area is directly proportional to its age. Therefore, it is necessary to correct the pressure of the shrinkage area [33].

$$e_c(t) = ke_c. \tag{7}$$

In the formula, $e_c(t)$ represents the compressive strength of the concrete at t day age and k represents the compressive strength coefficient in the contraction area.

On this basis, the areas requiring compensation are determined as follows:

$$R_c = \sum_{c=1}^{n} (p \times f_c). \tag{8}$$

In the formula, R_c represents the weight within a unit volume, p represents the axial core tensile strength, and f_c represents the area to be compensated for.

After determining the compensation area of the shrinkage area, the expansion agent is used to compensate for the shrinkage area of the concrete-filled steel tubular structure. The effect of different expansion agents on shrinkage compensation is different. In this paper, the concrete structure shrinkage compensation needs to consider its application environment, and its amount should also be determined. If the content is too small, it cannot achieve the expected effect of shrinkage compensation. If the content is too large, it may lead to the expansion and cracking of concrete. The sulphoaluminate expansive agent is widely used in China because of its composition and expansion source. The types of sulphoaluminate expansive agents are shown in Table 1.

Aluminite is the most widely used expansive that uses calferitecrystals $C_3A * 3CaSO_4 * 32H_2O$. It expands the volume of the concrete. The mechanism of the type CSA expansion agent is as follows:

$$C_4A_3\bar{S} + 6C_a(OH)_2 + 8CasO_4 + 96H_2O \longrightarrow 3(C_3A^*3CasO_4^*32H_2O). \tag{9}$$
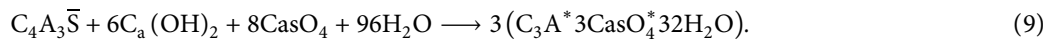
Calcite is a kind of only micron crystallization generated in the process of cement hardening, which grows in radiation among the colloidal particles with continuous volume expansion, realizing the concrete shrinkage compensation. The process of stress change of the concrete structure of a large cross-sea bridge is shown in Figure 3.

4. Experimental Result

4.1. Design of Shrinkage Experiment Scheme for CSTS-LCSB.
In order to verify the effect of the proposed compensation technology, a simulation experiment is carried out. In the experiment, a section of concrete-filled steel tubular structure in a sea cross is taken as the research object, which is a steel-concrete structure. Due to the deficiency of the bridge foundation conditions, a supporting pile is set in the experiment, whose size is 60 m * 30 m * 0.4 m. Because the structure is

long, a section of the pouring belt is set, and the experiment is carried out by continuous pouring of the expansive agent. Firstly, the concrete shrinkage structure of the research object is obtained. The area to be compensated and the change in the overall stress are judged, and the observation is carried out for one month. Among them, the concrete strength grade is C35, and the impermeability grade is p6. The cement used in the experiment is the standard grade cement, which is compensated according to the actual shrinkage structure characteristics. The experimental parameters of the expansion agent are shown in Table 2.

4.2. Shrinkage Test Index of CSTS-LCSB.
According to the design of the previous experimental scheme, the comparative experiment is used to analyze and compare the technology. The performance of the shrinkage control method of

TABLE 1: Types of sulphoaluminate expansive agents.

| Expansion and variety	Abbreviation	Expansion source	Standard dosage (%)	Basic composition
Calcium sulphoaluminate expansion agent	CSA	Ettringite	8	Calcium sulphoaluminate clinker and gypsum
Type U expansion agent	UEA	Ettringite	12	Calcium sulfur aluminate clinker, gypsum
Calcium aluminate expansion agent	AEA	Ettringite	10	Calcium sulfur aluminate clinker, gypsum
Alumite expansion agent	EA-L	Ettringite	15	Alumite, gypsum
Type U is a highly efficient expansion agent	UEA-H	Ettringite	8	Calcium sulfur aluminate clinker, gypsum
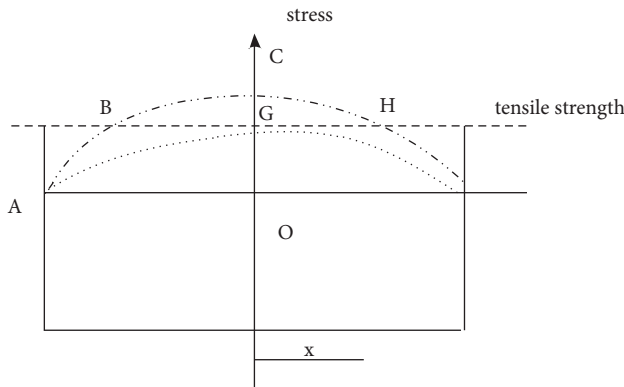
Figure 3: Stress change process of shrinkage compensation for concrete steel pipe structure of the large cross-sea bridge.

Table 2: Mix proportion of the expansion agent for compensation.

Material names	Scaling (%)
Calcium aluminate expansive agent	10%
Water	40%
Cement	5%
Calx	3%
Sand	5%
Other	—
Number of compensations	100

super-high tower high-strength concrete, the anticrack performance analysis of shrinkage compensating concrete impervious panel during the construction period, and the effect of compensation are analyzed. Among them, the compensation effect is reflected by the cracks of the compensated concrete members. The lower the amount of cracks, the better the compensation effect.

4.3. Analysis of Shrinkage Test Results of CSTS-LCSB

4.3.1. Comparison Results of Compensation Accuracy. The accuracy of shrinkage compensation for the structure is an important index to reflect the effectiveness of the method and can reflect the quality of the compensation effect. Therefore, the experimental analysis of the technology in this paper, the performance research and shrinkage control method of high-strength concrete for super-high bridge tower, and the anticrack performance analysis method of the antiseepage panel of shrinkage compensating concrete during the construction period are carried out. The precision of shrinkage compensation for the concrete-filled structure of large sea-cross is shown in Figure 4.

It can be seen from the analysis of Figure 4 that under the same experimental environment, there are some differences in the accuracy of shrinkage compensation for large-scalecross-sea bridge concrete-filled steel tubular construction by using the technology in this paper, the performance research and shrinkage control method of ultra-high tower high-strength concrete, and the anticrack performance analysis method of shrinkage compensating concrete impervious panel during construction. Among them, the

accuracy of the proposed method for compensating the sample flood concrete specimen is always high, up to about 97%, and the accuracy of shrinkage compensation by using the performance research and shrinkage control method of super-high bridge tower high-strength concrete is up to about 81%. The crack resistance performance analysis method of shrinkage compensating concrete impervious panels during the construction period has the highest accuracy of 78% for the shrinkage compensation. In contrast, the accuracy of the proposed compensation technology is higher than that of the other two traditional methods. This is because the proposed method fully analyzes the key factors such as concrete creep before compensation, which improves the effectiveness of the compensation technology.

4.3.2. Comparison Results of Crack Amount of Concrete Samples. On the basis of ensuring the previous compensation accuracy, the technology in this paper, the performance research and shrinkage control method of high-strength concrete for super-high bridge towers, and the anticrack performance analysis method of the antiseepage panel of shrinkage compensating concrete during construction are compared in the experiment. The crack generation amount of sample concrete specimens is analyzed, and the results are shown in Figure 5.

By analyzing the data in Figure 5, it is found that with the change of observation time, there are some differences in the production of concrete cracks after compensation among the proposed technology, the performance of high-strength concrete for super-high bridge tower, and the shrinkage control method, as well as the analysis method of anticrack performance of shrinkage compensating concrete impervious panel during the construction period. There are different fluctuations in the three methods. Among them, the fluctuation degree of performance research and shrinkage control method of high-strength concrete for super-high bridge tower is higher than that of the other two methods, and the amount of cracks is also the highest among the three compensation technologies. Its maximum amount of crack generation reaches 12.8%. As for the shrinkage control method, the maximum amount of crack generation reaches 11.7%. In contrast, the amount of cracks in concrete compensated by this compensation technology is lower than that of the other two methods. Therefore, it is proved once again that the method proposed in this paper can achieve better shrinkage compensation effect. This is because the compensation area is confirmed before compensation, and the reasonable proportion of expansion agent is considered to improve the compensation effect.

In order to verify the practical application effect of this experiment, this research method is applied to the practical application research and analysis of a large cross-sea bridge concrete-filled steel tube structure. MgO expansive agent and calcium sulphoaluminate expansive agent are used for hydration, and the effect of compensating the shrinkage of cement materials with a low water-cement ratio is shown in Figure 6.

Figure 6 shows the magnesium oxide composite expansion agent composed of MgO and CaO in different proportions. In the environment of water-saturated curing
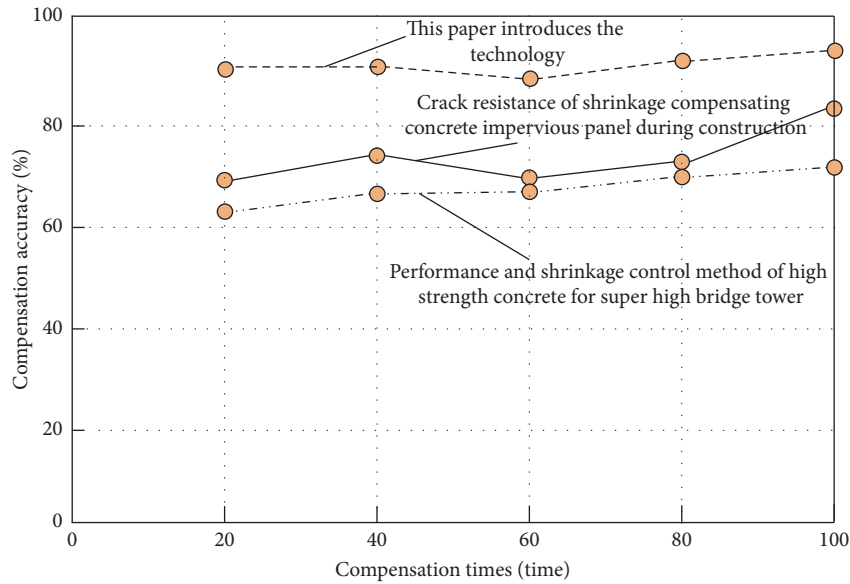
FIGURE 4: Comparison results of compensation accuracy of different compensation technologies.
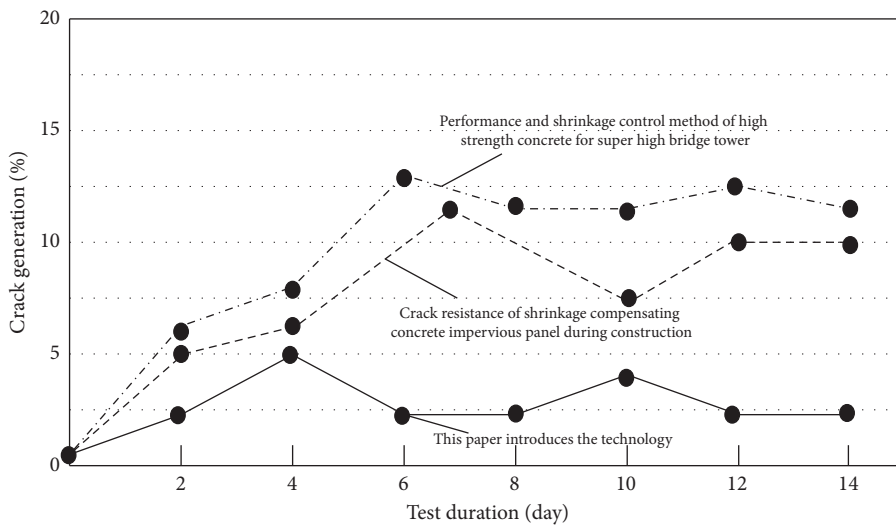
FIGURE 5: Comparison results of the crack amount of concrete samples with different compensation techniques.

or sealing, the use of a reasonable proportion can effectively eliminate the early autogenous shrinkage or autoexpansion of concrete and has a very obvious effect of inhibiting shrinkage. In practical application, the delayed microexpansion of MgO concrete can be used to compensate for the volume shrinkage of mass concrete in the bad state of cooling. The method proposed in this paper can achieve a better shrinkage compensation effect.
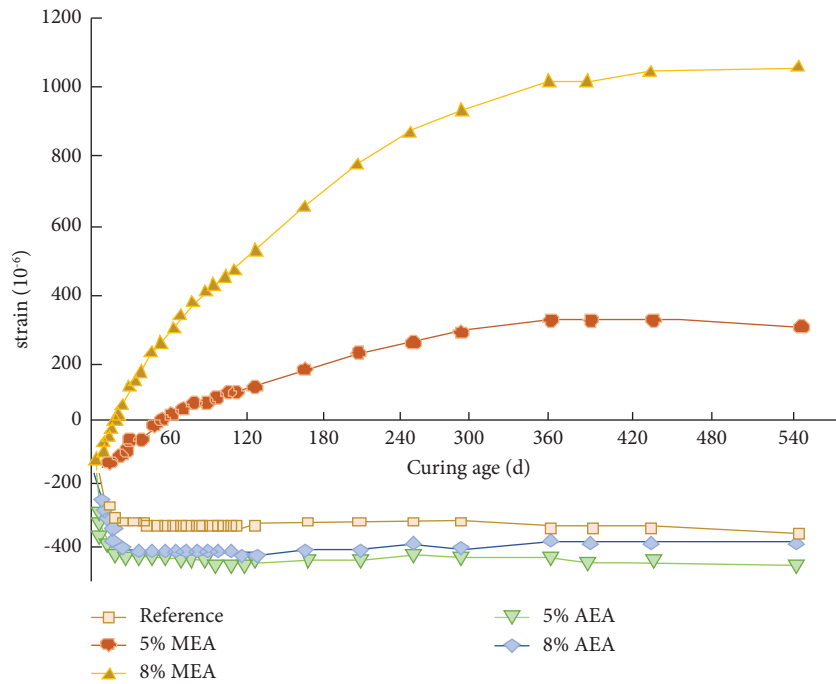
FIGURE 6: Autogenous deformation of Portland cement pastes containing various contents of MEA under nonwet curing conditions.

5. Conclusion

On the basis of referring to the existing literature on shrinkage compensation of concrete-filled steel tubular structures, a new shrinkage compensation technology is proposed. Firstly, the shrinkage mechanism of CSTS-LCSB is analyzed to improve the shrinkage compensation effect of CSTS-LCSB, analyzing objects including plastic shrinkage, dry shrinkage, autogenous shrinkage, and carbonation shrinkage. The proportion of dry shrinkage and autogenous shrinkage in ordinary concrete and high-strength concrete is determined. The structure has different shrinkage forms in different environments, and the shrinkage strain state in different environments is calculated. The shrinkage area of the concrete structure is determined, and the expansion agent is used to compensate for the shrinkage area of CSTS-LCSB. In order to verify the applicability and the actual shrinkage compensation effect of the method proposed in this paper, a cross-section of CSTS-LCSB is taken as an experimental object for simulation experiments and compared with the performance research and shrinkage control method of super-high-strength concrete for bridge tower and the anticrack performance analysis method of antiseepage panel of shrinkage compensating for concrete during the construction period. The experimental results are as follows:

(1) By comparison, the proposed method has the highest compensation accuracy of 97% for the structural shrinkage of concrete samples and has a certain compensation accuracy.

(2) In contrast, the amount of cracks produced by the proposed method is the least-always less than 5% after shrinkage compensation, which verifies that the effect of the proposed method is effectively alleviated. In practical application, the delayed microexpansion of MgO concrete can be used to compensate for the volume shrinkage of mass concrete in the bad state of cooling and achieve a better shrinkage compensation effect.

Experiments showed that the method proposed in this paper has high precision of shrinkage compensation and the ideal effect of shrinkage compensation. At the same time, this paper analyzes the different causes and mechanisms of concrete shrinkage and analyzes how the shrinkage of CSTS-LCSB is affected by different environmental factors including temperature, humidity, and so on. Although the technology in this paper has achieved some results in the current stage, the environment of concrete is constantly changing. If we want to continuously improve the compensation effect, we need to consider more environmental impact. In future research, we will focus on the improvement of this aspect and contribute to the improvement of concrete performance.

Data Availability

The data used to support the findings of this study are available from the corresponding author upon request.

Conflicts of Interest

The authors declare that they have no conflicts of interest.

References

[1] J. Li and Y. Narita, "Analysis and optimal design for the damping property of laminated viscoelastic plates under general edge conditions," *Composites Part B: Engineering*, vol. 45, 2013.

[2] M. F. Wang and X. F. Zhu, "Experimental study on seismic performance of high damping ECC and CFRP bars reinforced concrete shear wall with concealed bracing," *Earthquake Engineering and Engineering Vibration*, vol. 40, no.5, 2020.

[3] Z. Huang, Z. Y. Liu, and Y. Zhou, "Influence of design parameters on mechanical properties of nonlinear viscous damper," *Earthquake resistant engineering and Retrofitting*, vol. 40, no.5, 2018.

[4] F. M. Ye and M. Meng, "Analysis of contact strength of gear and rack in self-elevating offshore platform," *Computer Simulation*, vol. 34, 2017.

[5] J. P. Liu, Q. Tian, Y. J. Wang, H. Li, and W. Xu, "Evaluation method and mitigation strategies for shrinkage cracking of modern concrete," *Engineering*, vol. 7, no. 3, 2021.

[6] M. Mastali, P. Kinnunen, A. Dalvand, R. M. Firouz, and M. Illikainen, "Drying shrinkage in alkali-activated binders – a critical review Construct," *Build. Mater*, vol. 190, 2018.

[7] M. T. Hasholt, O. M. Jensen, K. Kovler, and S. Zhutovsky, "Can superabsorent polymers mitigate autogenous shrinkage of internally cured concrete without compromising the strength?" *Construction and Building Materials*, vol. 31, 2012.

[8] Z. G. Yan, M. Z. An, B. J. Yin, Y. Wang, and J. Z. Liu, "Performance and shrinkage control of high strength concrete for super high bridge tower," *Journal of Railway Engineering Society*, 2020.

[9] J. Cai, "Ship electronic information identification technology based on machine learning," *Journal of Coastal Research*, vol. 103, no. sp1, 2020.

[10] L. Wang, T. Yang, B. Wang, Q. Lin, and S. Zhu, "RALF1-FERONIA complex affects splicing dynamics to modulate stress responses and growth in plants," *Science Advances*, vol. 6, 2020.

[11] Z. F. Yan, X. G. Dong, R. Yang, M. Li, and W. Xu, "Design and preparation of non shrinkage high crack resistant concrete in large diameter steel tube," *Jiangsu Construction*, vol. 5, 2021.

[12] X. J. Zhou, S. Pang, Q. J. Ding, T. Y. Mu, J. Q. Peng, and C. J. Li, "Preparation and application of self compacting shrinkage compensating high strength steel tube concrete," *China Concrete and Cement Products*, vol. 6, 2021.

[13] W. K. Li, "Mechanism of concrete damping in Zhounan expressway," *Road Machinery & Construction Mechanization*, vol. 37, 2020.

[14] D. Luo and M. F. Wang, "Seismic performance of high damping concrete core walls with steel plate concealed bracings and different boundary elements," *Earthquake Engineering and Engineering Vibration*, vol. 39, 2019.

[15] J. J. Guo, S. W. Zhang, Y. Xia, and S. S. Wang, "Analysis of Crack resistance of shrinkage? Compensating concrete impervious face slab during construction period," *Yellow River*, vol. 42, February 2020.

[16] M. W. Braestrup, "Concrete plasticity-A historical perspective," *Structural Concrete*, vol. 22, 2021.

[17] T. Park, B. Ahmed, and G. Z. Voyiadjis, "A review of continuum damage and plasticity in concrete: Part I–Theoretical framework," *International Journal of Damage Mechanics*, vol. 31, 2022.

[18] H. Zhang, Y. Liu, and Y. Deng, "Temperature gradient modeling of a steel box-girder suspension bridge using Copulas probabilistic method and field monitoring," *Advances in Structural Engineering*, vol. 24, 2021.

[19] T. D. Shao and C. M. Zhang, "Seismic performance of multi-storysteel-concrete structure for civil high-rise buildings," *China Earthquake Engineering Journal*, vol. 42, 2020.

[20] S. P. Shang and C. Liu, "Application of reinforced concrete friction damper in seismic isolation layer," *Journal of Railway Science and Engineering*, vol. 16, 2019.

[21] Q. Li, K. Zhou, and X. Li, "Damping estimation of high-rise buildings considering structural modal directions," *Earthquake Engineering & Structural Dynamics*, vol. 49, 2020.

[22] G. L. Hou, M. Li, S. Hai et al., "Innovative seismic resistant structure of shield building with base isolation and tuned-mass-damping for AP1000 nuclear power plants," *Engineering Computations*, vol. 36, 2019.

[23] N. Vogler, P. Drabetzki, M. Lindemann, and H. C. Kühne, "Description of the concrete carbonation process with adjusted depth-resolved thermogravimetric analysis," *Journal of Thermal Analysis and Calorimetry*, vol. 147, 2021.

[24] M. Tarp, C. Georgakis, A. Brandt, and R. Brincker, "Experimental determination of structural damping of a full-scale building with and without tuned liquid dampers," *Structural Control and Health Monitoring*, vol. 28, 2020.

[25] H. Huang, M. Huang, W. Zhang, and S. L. Yang, "Experimental study of predamaged columns strengthened by HPFL and BSP under combined load cases," *Structure and infrastructure engineering*, vol. 17, 2020.

[26] M. Ghasemi, C. Zhang, H. Khorshidi, and L. Sun, "Seismic performance assessment of steel frames with slack cable bracing systems," *Engineering Structures*, vol. 250, 2021.

[27] X. X. Dai and Z. Y. Wen, "New alkali slag concrete technology," *Architectural Technology*, vol. 1, 1999.

[28] S. Al-Subaihawi, C. Kolay, T. Marullo, J. M. Ricles, and S. E. Quiel, "Assessment of wind-induced vibration mitigation in a tall building with damped outriggers using real-time hybrid simulations," *Engineering Structures*, vol. 205, 2020.

[29] M. Bottlang, A. Rouhier, S. Tsai, J. Gregoire, and S. M. Madey, "Impact performance comparison of advanced bicycle helmets with dedicated rotation-damping systems," *Annals of Biomedical Engineering*, vol. 48, 2020.

[30] N. Zhou, W. X. Shi, and J. Z. Shang, "Seismic response of a light steel structure integrated building with steel mortise-tenon connections," *Advances in Structural Engineering*, vol. 22, 2019.

[31] J. H. Hu, W. J. Chen, and Y. G. Qu, "Safety and serviceability of membrane buildings: a critical review on architectural, material and structural performance," *Engineering Structures*, vol. 210, 2020.

[32] J. Yuan, Y. Zhao, and Q. Y. Long, "Simulation of stress test of concrete lining structure based on prestress," *Computer Simulation*, vol. 38, 2021.

[33] K. Himoto, "Conceptual framework for quantifying fire resilience – a new perspective on fire safety performance of buildings," *Fire Safety Journal*, vol. 120, 2020.

Research Article

Comparison and Cost Analysis of Soft Soil Foundation Treatment Schemes in Port Construction

Qiang Ren ⓘ

Department of Engineering Management, Sichuan College of Architectural Technology, Deyang 618000, China

Correspondence should be addressed to Qiang Ren; renqiang@scac.edu.cn

Due to the characteristics of soft soil foundations in port engineering construction, there is a problem of insufficient bearing capacity, which needs to be treated. This paper analyzes the construction process and key points of the dynamic compaction method, vacuum preloading method, and vibroflotation method, and expounds on the advantages and disadvantages. The cost of different methods is compared. It can be seen that compared with other methods, the vibration impact method has a simple construction process and low cost.

1. Introduction

In recent years, with the rapid economic development of coastal cities, many port projects, cofferdams, and coastal new areas have begun to build, and land resources have become a key factor restricting their sustainable development. Therefore, the most important project for the development and utilization of tidal flat resources and the development of the marine economy is to reclaim land from the coastal tidal flat to alleviate the contradiction between rapid economic development and the relative shortage of land resources [1]. Port projects and other near-shore projects have undergone nearly 20 years of large-scale construction; the natural excellent port sites have been basically developed and constructed. To this end, people gradually began to shift their vision back to the original view that is not suitable for the construction of port sites, through a variety of man-made means to improve their natural conditions, so that they also have the corresponding construction conditions [2]. Soft soil foundation is one of the most common problems in offshore engineering.

Soft soil foundation is widely distributed throughout the world, in which marine facies and lacustrine facies are the main characteristics: high water content, easy compression, low strength, a small permeability coefficient, and easy

thixotropy. In our coastal areas, the Bohai Bay, the East Sea coast, the Taiwan Strait, the Pearl River estuary, and nearby waters are widely distributed. There are some problems, such as insufficient bearing capacity in port engineering construction on soft soil foundations. Improper treatment will directly affect not only the quality and cost of the project but also may cause engineering accidents [3]. In order to improve the soft soil foundation and make it meet the requirements of shear, compression, and dynamic characteristics of the project, as well as to ensure the safety and normal use of port engineering [4, 5]. Aiming at the soft soil foundation, foundation treatment, as a commonly used technique, can effectively improve the bearing capacity of the foundation or reduce the settlement of the foundation or other special requirements.

At present, there are several kinds of treatment methods in port engineering. Replacement method: The main idea of this method is to excavate all or part of the weak soil and then use better materials to replace it. This kind of method can effectively improve the bearing capacity and obviously reduce foundations settlement. Some scholars use the dynamic compaction replacement method in the treatment of soft soil foundation of expressways, using the lifting equipment to lift the heavy hammer to a certain height to make it fall down freely, and using the impact energy to

repeatedly tamp the crushed and gravel cushion laid on the soft soil surface, squeeze it into the soft soil layer, occupy the soft soil position, and play the role of replacement, so as to improve the bearing capacity of the foundation within a certain range, reduce its compressibility, and improve the bearing performance of the foundation. This method has strong applicability and remarkable reinforcement effect, and can effectively reinforce the soft soil subgrade of expressways [6, 7]. Drainage consolidation method: Drainage consolidation is a method to drain the soil, promote the dissipation of excess pore water pressure, reduce the pore ratio of soil, improve the shear strength of the soil, so as to improve the bearing capacity of the foundation, and reduce the settlement of the foundation after construction. Some scholars have used the dynamic drainage consolidation method of multidrop and multitamping combined with depth and shallowness during the reclamation of coastal tidal flats. This method combines precipitation and dynamic consolidation through the dynamic characteristics and dynamic consolidation mechanism of saturated soft clay to achieve foundation treatment. Dynamic compaction is used to change the structure of soil mass, resulting in excess pore water pressure, and then dynamic drainage is used to accelerate the dissipation of excess pore water pressure, strengthen the soil mass, shorten the consolidation time of the soil mass, improve the strength of the soil mass, and reduce the compressibility of the soil mass, which has a good application effect [8, 9]. The surcharge preloading method, vacuum preloading method, and vacuum combined surcharge preloading method are mainly used in port engineering. Low-energy dynamic compaction can reduce the compaction energy and improve the bearing capacity of the foundation. The cost of treatment is low, and the operation is very simple, reducing the impact on the surrounding environment. Some scholars have adopted the construction technology of the low-energy dynamic compaction method and CFG pile to jointly treat the foundation, which not only solves the load requirements of the engineering ground and foundation but also meets the extremely strict settlement design value. It has the advantages of a short construction period, low cost, low pollution, and high safety. However, due to the large vibration during the dynamic compaction construction, it is necessary to consider whether the surrounding environment of the proposed building is allowed before construction [10]. Vibroflotation is a method of compacting the soil by vibration or compaction in order to improve the bearing capacity of the foundation and reduce settlement.

Because of its high compressibility, a large amount of deformation, long duration, and low shear strength, soft soil may cause such engineering disasters as pavement cracking, bridgehead jumping, serious embankment deformation, and even instability, which is a major hidden danger for road safety and stability [11–13]. Therefore, in order to solve the problem of settlement or differential settlement brought by soft soil foundations in a coastal area, this paper studies different foundation treatment schemes and their cost comparison. The research flow of the article is shown in Figure 1.
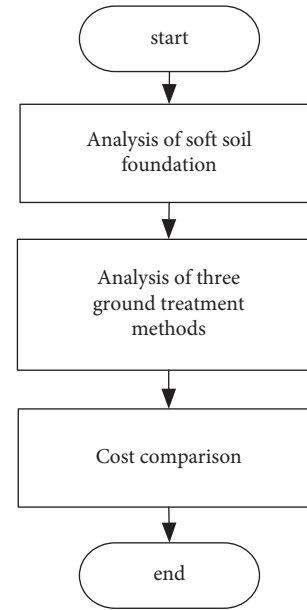
Figure 1: Flow chart.

2. Characteristics of Soft Soil and Common Treatment Methods of Soft Soil Foundation

Because of its easy deformation, soft soil foundation is easy to appear unstable. In its natural state, it can maintain stability, but when the soft soil is disturbed, its structure is easy to destroy and begin to flow. Therefore, the main engineering problems in the treatment of soft ground are attributed to the promotion of settlement and the maintenance of stability. Soft soil is divided into many kinds according to its different forms. But they all have the following common engineering characteristics, as shown in Figure 2.

(1) The natural water content is high, generally higher than the liquid limit, generally higher than 30% or even higher than 200%, and the relative water content is higher than 1.0. (2) The natural void ratio is large, and e is generally greater than 1.0. (3) The permeability coefficient is small, with a range of 10–6 to 10–8 cm/s, and the natural settlement consolidation speed is slow and the time is long. (4) High clay content and large plasticity index. (5) The strength index is small and has a high consolidation quick shear strength index, and the shear strength is less than 0.02 MPa.

Foundation treatment generally refers to the engineering measures taken to change the bearing capacity of the foundation or improve the deformation or permeability. Through the foundation treatment, we generally want to achieve the following purposes:

(1) To improve the bearing capacity of the foundation, the concrete manifestation of the shear failure of the foundation is that the bearing capacity of the foundation is insufficient and the shear strength is insufficient. Therefore, in order to prevent shear failure, we must take certain foundation treatment measures to improve the shear strength of foundation soil.

Figure 2: Flow chart of the land-based processing method.

(2) Reduce the compressibility of the foundation soil. The compressibility of the foundation mainly lies in the settlement and differential settlement of the foundation. Therefore, the foundation treatment method is adopted to improve the compression modulus of the soil so as to make the post-construction settlement and settlement difference meet the use requirements.
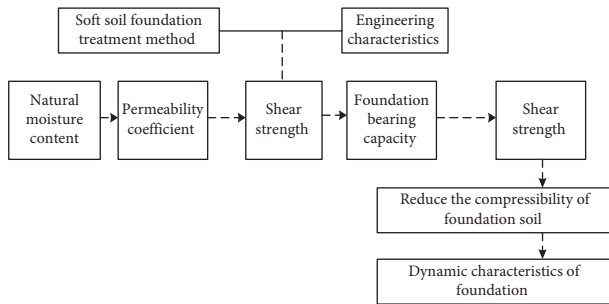
(3) Improving the seepage and dynamic characteristics of the foundation. Due to the poor permeability of the soft soil foundation, some of the soft soil will liquefy under dynamic load. The purpose of foundation treatment is to improve the dynamic characteristics of the foundation.

Commonly used methods of soft soil foundation treatment include chemical reinforcement, load reduction, filling, drainage consolidation, composite foundations, and other methods. Methods for comparative analysis are given as follows.

3. Comparison of Construction Schemes for Soft Foundation Treatment in Different Ports

After nearly 10 years of development, port engineering has achieved fruitful results, especially the progress of soft foundation treatment technology. At present, the methods of soft foundation treatment commonly used in port engineering include the vacuum preloading method, pile-up preloading method, vacuum combined surcharge preloading method, dynamic compaction method, and vibroflotation replacement method [14]. The cost analysis at the design stage is mainly based on the Provisions on the Budget Preparation of Coastal Port Construction Projects and the supporting quotas (hereinafter referred to as the "current quotas") [15]. However, there is a contradiction between the development of soft foundation treatment technology and the relative lag of the current quota, which makes it particularly important to master the construction methods and techniques, properly use the quota, and obtain the price index for correctly compiling the cost documents of soft foundation treatment [16]. In this paper, three classical methods of soft soil foundation treatment are selected, namely dynamic compaction, vacuum preloading, and vibroflotation replacement. The characteristics and construction process are summarized.

Various types such as ZCQ75, ZCQ100, ZCQ132, ZCQ180A, and ICEV230 are adopted for the port foundation treatment project, and the matching model is selected through the vibration test of the test section. As shown in Table 1.

3.1. Dynamic Compaction.

Dynamic compaction is often used in foundation treatment. This method is a new technology of soft soil reinforcement that has been developed and studied for more than 10 years. There is a marked difference between the construction method and the dynamic compaction method [17]. According to the basic principle of dynamic compaction, the structure of the soil must be destroyed first and then consolidated again. However, dynamic compaction can only be used in the case of clay with a certain water content. The low-energy dynamic compaction method can be used to tamp the soil under the condition that the structure of the soil does not change or significant damage does not occur.

3.1.1. Mechanism Analysis of Consolidation by Dynamic Compaction.

According to the previous research results, the mechanism of dynamic compaction is as follows: the shock wave produced by compaction breaks the connection between soil particles, and with the increase of compaction energy, the pore and a particle shape of the pit subsoil develop from a pore shrinkage stage to a particle deformation stage to a particle inlay stage, thus changing the distribution state of all kinds of pores in the soil and their relative content [10]. That is to say, compaction destroys the original loose structure of the soil, changes the connecting mode between the skeleton particles, and makes the soil particles rearrange into a dense structure. With the recovery of soil thixotropy, the cohesive, colloidal, and crystalline salts in a more compact state can play a better role in cementation and improve the shear strength and deformation resistance of the soil. The dynamic consolidation of filler is shown in Figure 3.

According to Mena's equation, the relationship between the depth of reinforcement and the main influencing factors is established.

$$H = \beta \sqrt{\frac{Qh}{10}}. \tag{1}$$

In (1), β is the coefficient related to the properties of foundation soil. Q is the hammer weight, kg. h is the height, m. H for design reinforcement depth, m.

Key indexes of the dynamic compaction method: The indexes affecting the effect of dynamic compaction mainly include compaction energy (weight of the hammer and falling distance), times of compaction, compaction distance, and safety distance. As shown in Figure 4.

(1) Tamping energy: Tamping energy is the most significant factor that affects the effective depth of dynamic consolidation and is also the decisive factor in cost of the treatment project. The choice of

TABLE 1: Main technical parameters of vibroflotation device.

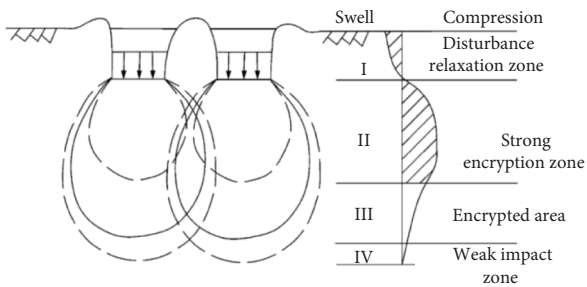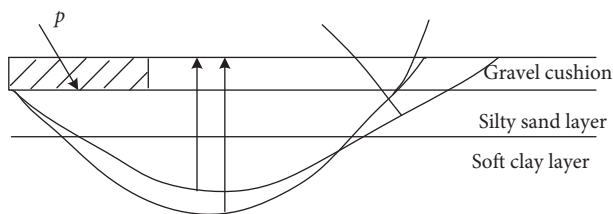| Project	ZCQ75D	ZCQ75D	ZCQ132A	ZCQ180A	ICE V230
Motor power	75	100	132	180	230
Speed	1460	1480	1480	1480	3000
Rated current (A)	150	197	246	336	—
Exciting force (kN)	160	190	220	300	388
Overall dimension	420 * 3210	402 * 3215	402 * 4003	402 * 4470	—
Weight (kg)	1800	1900	2500	3000	3260

FIGURE 3: Dynamic consolidation of filler.

FIGURE 4: Schematic diagram of the depth of the foundation holding layer.

ramming energy is mainly based on the depth of reinforcement and the extrusion of the abutment. According to the predicted depth of treatment, the maximum tamping energy should not be less than 40 tm.

(2) Determination of hammer weight and fall distance: In order to maximize the performance of dynamic ramming machinery, generally, the greater the rammer weight is, the better (the weight shall be more than 10 t). After the rammer weight is determined, the fall distance can be determined according to the ramming energy.

(3) Tamping times: The engineering data show that the dynamic stress at the same position increases with the increase of tamping times; the dynamic stress of soil tends to be stable after 3–5 hits, and the tamping settlement of soil tends to be stable after 5–10 hits, which indicates that the soil is compacted. According to the ramming energy, the criterion for judging the end of ramming is that the difference between the adjacent two ramming sinks is less than 3–5 cm.

(4) Tamping point layout and spacing: Tamping point layout generally uses plum blossom or square network arrangements with a tamping point spacing of 3 to 5 m. Considering the actual situation of the project, it is suggested that the first ramming point should be arranged as a regular triangle with a spacing of 3 m, and the second ramming point should be located at the center of the first ramming point.

(5) Safety distance: Reducing the impact of ramming on bridge structures and ensuring the stability of embankments is the key to limiting the applicable scope of this method. In design, in order to ensure ramming quality and avoid quality accidents such as abutment cracking and embankment instability, the distance from the ramming point edge to the abutment (embankment edge) shall be determined before ramming, that is, the safety distance. According to the contour map of dynamic compaction hole pressure distribution, when the radial distance is more than 2 m, the impact degree of compaction is obviously reduced, so the safety distance can be determined as 2 m.

3.2. Vacuum Preloading.

The vacuum preloading method is one of the most commonly used technologies for soft soil foundations. Its weak drainage effect and siltation of the drainage plate seriously restrict the consolidation effect [2]. This method is generally applied to soft clay and ultra-soft clay and is suitable for storage yards and warehouses. It is characteristic that the foundation does not increase the total stress, the soil is in lateral compression, it does not need to carry out heaping, and it can save the relevant information. The construction example is shown in Figure 5.

3.2.1. Mechanism Analysis of Strengthening by Vacuum Preloading.

When using a vacuum load to reinforce a soft soil foundation, the vacuum load is applied to a sand cushion by a vacuum pump. The vacuum load is transferred to the deep part of the soil through the plastic drainage plate; thus, the pore water pressure of the soil is gradually reduced, and the effective stress of the soil is correspondingly increased. This is the basic principle of vacuum preloading [18]. In the vacuum preloading method, a vertical drainage channel is set up in the soft soil foundation and a layer of sand cushion is laid on the ground as a horizontal drainage channel. A vacuum under the membrane forms a pressure difference. This pressure difference is what we usually call a "vacuum." The vacuum formed in the sand cushion is transferred to the deep soil through the vertical drainage passage, and the pore water pressure of the soil is reduced so that the water of the soil is seeped up to the sand cushion along the vertical

FIGURE 5: Construction example.

drainage passage, and finally, the water is drawn out of the reinforcement area to achieve the effect of drainage consolidation.

The vacuum preloading method uses the vacuum pump to reduce the pressure under the sealing membrane to P_n', and the pressure outside the sealing membrane to P_0, thus forming a certain degree of vacuum $\Delta P = P_0 - P_n'$.

The empty load is transferred to the deep soil through the plastic drainage slab, which makes the pore water pressure in the plastic drainage slab decrease rapidly. But because the permeability coefficient of soil is small and the transfer speed of vacuum in the soil is slow, the atmospheric pressure P_n of soil is in the state before vacuuming, so the pore water pressure difference between soil and the plastic drainage plate is formed. Under the action of the pressure difference, the pore water in the soil is drained up through the plastic drainage plate, the pore water pressure in the soil is reduced gradually, and the soil is consolidated.

The degree of consolidation can be drawn as a hyperbola according to the settlement plate of each reinforcement area, and settlement calculation can be carried out according to the load change. The equation is as follows:

$$S_t = S_o + \frac{t}{\delta + \eta t}. \tag{2}$$

After deduction, the following may be obtained:

$$\frac{t}{S_t - S_o} = \delta + \eta t,$$

$$S_\infty = S + \frac{1}{\eta}. \tag{3}$$

In the equation: t is the time from the full load. S_o is the foundation settlement under full load; S_∞ is the final settlement of the foundation δ, β is the constant related to foundation and load; It can be determined according to the linear expression of (2) α, β. The measured settlement value is determined by (2), and the linear regression is analyzed. In the equation: t is the time starting from the full load. S_o is the settlement of the foundation at full load. S_∞ is the final

settlement of the foundation. δ and η is the constant relating to the foundation and load. δ and η value can be determined according to the linear expression (2), and the measured settlement value can be determined by the expression (2), and linear regression analysis is conducted.

3.3. Impulse Displacement Method.

In port engineering, this kind of method can be divided into two kinds: the vibration and impact replacement method and the vibration and impact compaction method. The method of vibration and impact compaction, in which the displacement material is not filled into the vibration and impact hole but only the effect of vibration and impact is used. Filling the vibration punching hole with broken stone or coarse sand to form a replacement pile is called the vibration punching replacement method [19]. Such methods are applicable to sandy soil, silty soil (silty clay), and unsaturated soil (mixed soil). The final characteristic is that the composite foundation can be formed, the speed of reinforcement is faster, the equipment is simpler, and the construction process is more convenient.

3.3.1. Mechanism Analysis of Vibration and Impulse Replacement Reinforcement.

The vibration and impact displacement method also uses the water impact force and the horizontal vibration force to form the hole, and it vibrates the backfill material in the hole with the vibrator. A series of piles are made in the foundation soil to replace part of the soft clay in the foundation soil to form a composite foundation [20]. The gravel pile is composed of vibrating stone piles and soft clay on the original foundation. The gravel pile not only has the bearing capacity of a pile foundation but also can play a certain drainage role to accelerate the drainage and consolidation of foundation soil. In the process of vibrating and punching piles, the horizontal vibrating force produced by the vibrating and punching machine will squeeze the backfill material out of the hole and push it into the soft soil layer around the hole wall, so that the diameter of the pile body is further enlarged. When the external force

produced by vibrating and punching with the constraint force of the soil body, the diameter of the pile body is fixed [21]. It should be noted that if the strength of the original soil in the foundation is low, the binding force of the backfill to resist the squeezing of the backfill under the external force will be relatively small, and the backfill will become coarser if it is further diffused around the hole. If the original soil strength in the foundation is too low to balance with the forcing force produced by vibroflotation, the backfill will spread around the hole unlimitedly, the pile body cannot be generated, and the vibroflotation replacement method cannot be used to strengthen the soft foundation. The scene shock picture is shown in Figure 6.

Vibroflotation foundation reinforcement requires a certain amount of gravel, coarse sand, gravel, or slag for backfilling, and its effects are mainly in two aspects: the vibrator impacts to form a hole, and the vibrating body may be left on the foundation soil after it is lifted upwards. Holes: the backfill is used to backfill this part of the holes, which is the first function of the backfill. The horizontal excitation force generated by the vibrator during operation will vibrate and compact the backfill, and the backfill continuously filled in the hole will act as a force transmission medium and further compact the foundation soil by squeezing. Body: this is the second function of backfilling. The suitable degree of backfill gradation in the course of vibration impact construction can be judged by index, and the suitable number is calculated by the following equation :

$$S_n = 1.7 \sqrt{\frac{3}{D_{50}^2} + \frac{1}{D_{20}^2} + \frac{1}{D_{10}^2}}. \tag{4}$$

In the equation, D_{50}, D_{20}, and D_{10} are corresponding to the particle diameter (mm) of 50%, 20%, and 10%, respectively.

In vibroflotation construction, if broken stone is used as backfilling material, weathered stone or semi-weathered stone should not be used as much as possible. In the course of vibroflotation construction, the strength and permeability of piles formed by vibroflotation become lower and worse because of broken weathered stone and semi-weathered stone caused by vibroflotation [22, 23]. Equation (5) can be used to estimate the amount of backfill to be filled in per unit volume of sand foundation:

$$V = \frac{(1 + e_w)(e_0 - e_1)}{(1 + e_0)(1 + e_1)}. \tag{5}$$

In equation (5), V is the amount of filler needed to be based on a unit volume. e_0 is the original void ratio of sand layer before vibration and scour. e_w is the void ratio of the pile. e_1 is the required void ratio after vibration impact.

Gravel, broken brick, crushed stone, slag, pebble, and so on can be used as pile materials in the vibroflotation replacement construction process, so it is an economical choice to take materials on the spot. However, no matter which material is used as backfill, there should not be more than 10% clay content. Generally, the gradation of backfill is not required, but the maximum particle size of backfill is

Figure 6: On-site vibroflotation.

more than 50 mm, which may cause the hole problem and will wear out the shell of the vibrator, so do not choose it easily.

Based on the above methods, the advantages and disadvantages of different methods are compared and analyzed. The results are shown in Table 2.

4. Cost Analysis

4.1. Cost of Dynamic Compaction Method [24]. The current quota contains dynamic tamping items with tamping energies of 1000 kN/m, 2000 kN/m, and 3000 kN/m and is divided into many cases according to the number of tamping points for every 100 m^2, including a tamping pit material backfilling a quota. The number of ramming points per 100 m^2 in the dynamic compaction quota is determined by multiplying the reciprocal of the shortest square distance between the ramming points in the layout of the final ramming points by 100 m^2, excluding the ordinary ramming points. The quota of dynamic compaction, including the number of tamping, the number of tamping times, and the number of knocking times of dynamic compaction should be adjusted according to the design. During the construction of dynamic compaction, the drainage machinery of the compaction pit has been calculated into other ship and machinery fees, and the use of the quota does not need to be increased. When the underground water level is unfavorable to construction, the sandstone cushion that needs to be bedded may be calculated according to the relevant quota of the bedding layer. Leveling includes leveling before ramming, after ramming, and in the ramming room. No additional calculation is required. For example, when ramming a strip foundation, the manpower in the ratio is multiplied by the coefficient of the ship. The backfill type of rammed pit material should be adjusted according to the design, such as soil, sandstone, or mountain soil.

TABLE 2: Comparison of advantages and disadvantages of different treatment methods.

Method	Advantage	Shortcoming
Dynamic compaction	(1) The dynamic compaction method is applicable to the treatment of gravel soil, silty soil, and cohesive soil with low saturation of sandy soil, collapsible loess plain fill, and miscellaneous fill. Especially for the treatment of collapsible loess, the practice has proved to be effective and reliable. (2) It exerts great impact energy on the foundation, and the general energy is 1000 kN m~8 000 kN. m. The shock wave and dynamic stress generated in the foundation can improve the strength of the foundation, reduce the compressibility of the soil, and eliminate the collapsibility of the collapsible loess. (3) Relative excavation and replacement can reduce the area of arable land occupied by spoil; reduce the amount of sand and gravel; compared with other soft soil subgrade treatment methods, the cost is low, the reinforcement effect is obvious, the construction period is short, and the cost is low.	(1) The reinforcement depth should not exceed 7 m. It has certain limitations. (2) The magnitude and dissipation speed of pore water pressure depends on the level of groundwater level and the permeability of the soil, which limit the construction period. (3) The noise and vibration are large, and it is not suitable for use in densely populated cities and residential areas.
Vacuum preloading method	(1) In addition to vertical compression, the soil will also be accompanied by lateral contraction during the reinforcement process, which will not cause lateral extrusion, making it especially suitable for the reinforcement of super-soft soil foundations. (2) Generally, the vacuum degree under the membrane can reach 600 mmhg, and the equivalent load is 80 kPa, which is about equivalent to a 4.5 m soil load; the vacuum preloading load can be overlapped with the surcharge preloading. When a preloading reinforcement load greater than 80 kPa is required, it can be used simultaneously with the surcharge preloading method. The preloading load exceeding 80 kPa is supplemented by the surcharge preloading. (3) Vacuum preloading load will not cause foundation instability, so it is not necessary to control the loading rate during construction. The load can be applied quickly at one time, with fast reinforcement speed and a short construction period. (4) Construction machines and equipment are simple and easy to operate; convenient for construction, high operation efficiency, low reinforcement cost, suitable for large-scale foundation reinforcement, easy to promote, and apply. (5) It does not need to load materials vigorously, which can avoid the transportation tension, turnover difficulties and construction interference caused by the transportation of materials; no noise, vibration, and environmental pollution during construction. (6) Suitable for foundation reinforcement in narrow sections and near slopes.	(1) Sufficient and continuous power supply is required: the reinforcement time should not be too long, otherwise, the reinforcement cost may be higher than the surcharge preloading of the same load. (2) In the process of vacuum preloading reinforcement, horizontal deformation will occur around the reinforcement area to the inside of the reinforcement area, and cracks often occur around 10 m away from the edge of the reinforcement area. Therefore, during construction near buildings, attention should be paid to the impact of foundation horizontal deformation on the original buildings during vacuum pumping.

TABLE 2: Continued.

Method	Advantage	Shortcoming
Vibroflotation method	(1) Reduce the settlement, form a composite foundation through the replacement principle of gravel pile, and greatly improve the bearing capacity and integrity of the foundation. (2) Eliminate liquefaction, and eliminate the liquefiable sand layer through the vibration compaction principle. (3) To improve the strength of foundation soil, the gravel pile is used as the vertical drainage channel of the foundation to squeeze and discharge the water in the saturated soft clay void, so that the foundation will gradually undergo consolidation deformation under the gradual action of the upper load, and finally improve the strength of foundation soil.	Gravel, electricity, water, and other materials are used in large amounts, and it is difficult to discharge sewage, especially in the process of vibroflotation.

In practical applications, it is found that the unit price of dynamic compaction quotas is expensive, and dynamic compaction with larger compaction energy is often used in construction. When the compaction energy is more than 3000 kN/m, there is no quota, and the engineering cost needs to be calculated by using the related cost indexes in the near future. In the northern port engineering area, the unit price of 3 times of the ramming technology (the first 2 times of point ramming, ramming capability of 5000 kN/m, ramming interval of 8 m, 10 strikes per ramming point, 3 times of normal ramming, ramming capability of 1000 kN/m) is generally about 50 yuan/m², and the actual bid price in construction is lower. In the southern port area, the unit price of 3 times ramming technology is generally about 25 yuan/m², and the actual construction price is lower.

4.2. Cost of Vacuum Preloading Method. The current quota mainly includes a vacuum preloading quota suitable for silt soil, and also includes leveling, sand cushion cleaning, fabrication and installation, etc. If the geotextile reinforcement is increased, the impervious layer quota of the laid plastic sheet can be adopted and the plastic sheet can be changed into geotextile. However, the artificial sand cushion can remove the loader and the bulldozer, and when the sand layer is blown to fill a large area, there is no relevant quota, and the real cost table of the project site is used, or the price is obtained through relevant exchanges with the owner. Compared with the general straight-row vacuum preloading, the supercharging system uses the drainage plate late supercharging; the supercharging system increases 4 yuan/m², and the other parts of the joint increase costs. But compared with the straight type, it needs more than 4 months to vacuum according to the treatment experience of dredger fill in Wenzhou, and the technology can achieve the expected effect in 3 months and can save about 10 yuan per m². The cost of pressurized vacuum preloading is basically the same as that of conventional direct vacuum preloading.

4.3. Cost of Pulse Displacement Method. First, the current quota situation. There is no relevant quota in the current quota. The second is the matter needing attention in the

application. There is a direct relation between the unit price, diameter, spacing, and length of vibrating piles, so the cost can be calculated according to the unit price index of vibrating piles, and the cost of filling materials can be calculated separately. For example, in the Dalian area, the diameter of piles is 1.2 meters, the distance between piles is 1.8 meters, and the length of piles is 15 meters, which can be calculated by using a 130 KW vibrator. The unit price of a vibration-driven pile is related to the distance between piles, the length of pile, and the soil to be reinforced. The cost may be calculated according to the unit price index of the prolonged rice, and the cost of the supplementary packing shall be separately calculated and listed. In the northern port area, the unit price of vibrating crushed stone piles (excluding the price of gravel filling materials) with a diameter of 1.2 m, a spacing of 1.8 m between piles, and a length of 15 m adopting a 130 kW vibrator is generally about CNY15/m².

To sum up, the cost comparison of different methods is shown in Table 3.

5. Discussion

(1) Dynamic compaction: This method is suitable for coarse-grained soil with a particle size of more than 0.05 mm, such as sandy soil, mountain soil, and so on. It is characterized by less equipment used and a faster speed of reinforcement, but its vibration and mechanical wear are relatively large. The cost of a project needs to be calculated by using the recent relevant cost indicators for the project location, and the cost is unstable.

(2) Vacuum preloading method: The vacuum preloading method is suitable for general soft clay and super-soft clay and is suitable for storage yards, warehouses, airports, and roads. Its characteristic is that the foundation does not increase the total stress, the soil has lateral compression, the effective compaction rate is high, it does not need to pile, and it saves the investment. The cost may adopt the recent cost index of the place where the project is located, which is usually obtained through the exchange of price inquiries with the owner and the relevant construction entities.

TABLE 3: Cost comparison of different methods.

Method	Cost (yuan/m^2)
Dynamic compaction	25
Vacuum preloading method	40
Vibroflotation method	15

(3) Vibration-impact replacement method: It is mainly suitable for clay soil and not suitable for soft reclaimed soil; its final characteristic is that it can form a composite foundation. With a relatively fast speed of reinforcement and relatively simple machinery and equipment, the construction process is more convenient. Compared with other methods, the vibroflotation method is simpler and cheaper. So long as it is used properly, there will be more room for development in the consolidation of underwater soft soil foundations.

In the above analysis, the vacuum preloading method has the characteristics of underwater construction that cannot be obtained, and the replacement method needs a lot of excavation and replacement that is expensive. The vibration and impact method is widely used in land buildings at present, but there are few cases of underwater construction in port engineering. Compared with other methods, the vibroflotation method is simpler and cheaper. So long as it is used properly, there will be more room for development in the consolidation of underwater soft soil foundations. Therefore, the construction of some small port projects can be shifted to this method on the premise of ensuring safety and paying less cost to meet the construction requirements of the project. In the design, it is necessary to analyze the relevant regulations, but there is a certain lag in the quota standards, so it is necessary to have a clear grasp of the construction methods and techniques and the applicable quota standards to ensure that they can be better controlled at cost.

6. Conclusion

This paper discusses the characteristics of various construction schemes applicable to soft soil foundations and studies the reinforcement principle, reinforcement method, application scope, and cost of the dynamic compaction method, vacuum preloading method, and vibroflotation replacement method. By comparing the construction technology, application advantages, and limitations of different methods, the cost of different methods is analyzed. Through the comparison results, it can be seen that the vibroflotation method has lower costs and is more cost-effective.

Data Availability

The data used and/or analyzed during the current study are available from the corresponding author upon reasonable request.

Conflicts of Interest

The author declares that there are no conflicts of interest.

References

[1] S. Lu and X. Shi, "Selection of treatment methods for soft foundation of river in a reclamation area," *IOP Conference Series: Earth and Environmental Science*, vol. 474, Article ID 072004, 2020.

[2] W. Zhu, J. Yan, and G. Yu, "Vacuum preloading method for land reclamation using hydraulic filled slurry from the sea: a case study in coastal China," *Ocean Engineering*, vol. 152, pp. 286–299, 2018.

[3] F. Q. Chen, G. H. Yang, S. K. Sun, D. S. Guan, and S. J. Zhu, "In-situ test of soft soil in Pearl River Delta: engineering practices and effect analysis of result applications," *Journal of Yangtze River Scientific Research Institute*, vol. 36, no. 4, p. 129, 2019.

[4] F. Kassou, J. B. Bouziyane, A. Ghafiri, and A. Sabihi, "Slope stability of embankments on soft soil improved with vertical drains," *Civil Engineering Journal*, vol. 6, no. 1, pp. 164–173, 2020.

[5] J. Yuan, D. Lei, Y. Shan, H. Tong, X. Fang, and J. Zhao, "Direct shear creep characteristics of sand treated with microbial-induced calcite precipitation," *International Journal of Civil Engineering*, vol. 20, no. 7, pp. 763–777, 2022.

[6] H. Huang, M. Huang, W. Zhang, and S. Yang, "Experimental study of predamaged columns strengthened by HPFL and BSP under combined load cases," *Structure and infrastructure engineering*, vol. 17, no. 9, pp. 1210–1227, 2021.

[7] Y. Zhai, G. Liu, F. Jin et al., "Construction of Covalent-Organic Frameworks (COFs) from amorphous covalent organic polymers via linkage replacement," *Angewandte Chemie*, vol. 131, no. 49, Article ID 17843, 2019.

[8] Y. Guo, Y. Yang, Z. Kong, J. He, and H. Wu, "Development of similar materials for liquid-solid coupling and its application in water outburst and mud outburst model test of deep tunnel," *Geofluids*, vol. 2022, pp. 1–12, 2022.

[9] L. Wang, T. Yang, B. Q. Wang et al., "RALF1-FERONIA complex affects splicing dynamics to modulate stress responses and growth in plants," *Science Advances*, vol. 6, no. 21, Article ID eaaz1622, 2020.

[10] S. Wu, Y. Wei, Y. Zhang et al., "Dynamic compaction of a thick soil-stone fill: dynamic response and strengthening mechanisms," *Soil Dynamics and Earthquake Engineering*, vol. 129, Article ID 105944, 2020.

[11] P. Barua and S. H. Rahman, "Aquatic health index of coastal aquaculture activities at South-Eastern coast of Bangladesh," *Water Conservation and Management*, vol. 4, no. 2, pp. 51–57, 2020.

[12] Z. Ding, J. Jin, and T. C. Han, "Analysis of the zoning excavation monitoring data of a narrow and deep foundation pit in a soft soil area," *Journal of Geophysics and Engineering*, vol. 15, no. 4, pp. 1231–1241, 2018.

[13] Z. Wu, J. Xu, H. Chen, L. Shao, X. Zhou, and S. Wang, "Shear strength and mesoscopic characteristics of basalt fiber-–reinforced loess after dry–wet cycles," *Journal of Materials in Civil Engineering*, vol. 34, no. 6, Article ID 247530357, 2022.

[14] X. Jiang, Q. Lu, S. Chen, R. Dai, J. Gao, and P. Li, "Research progress of soft soil foundation treatment technology," in *Proceedings of the IOP Conference Series: Earth and Environmental Science*, vol. 455, Article ID 012081, Nanchang, China, January 2020.

[15] Y. Chen, Y. Wei, and L. Peng, "Ecological technology model and path of seaport reclamation construction," *Ocean & Coastal Management*, vol. 165, pp. 244–257, 2018.

[16] X. Y. Wang, "Optimization design of subgrade strength for urban road reconstruction project," *Computer Simulation*, vol. 35, no. 4, pp. 311–314, 2018.

[17] M. Shen, J. R. Martin, C. S. Ku, and Y. C. Lu, "A case study of the effect of dynamic compaction on liquefaction of reclaimed ground," *Engineering Geology*, vol. 240, pp. 48–61, 2018.

[18] L. Fan and S. Chen, "Consolidation analysis and effect analysis in the treatment of soft foundation by vacuum preloading," in *Proceedings of the IOP Conference Series: Earth and Environmental Science*, 2021, Article ID 012135.

[19] Y. W. De, C. Sheng, and C. L. Xiao, "Field test and inspection of large area hydraulic sand ground improved by vibro-compaction," *IOP Conference Series: Earth and Environmental Science*, vol. 304, Article ID 032068, 2019.

[20] C. Ramanathan and P. Prasad, "Vibro compaction technique in liquefaction mitigation and its value addition — a case study," in *Proceedings of the Indian Geotechnical Conference 2019*, pp. 311–319, Singapore, 2019.

[21] R. Tao, X. Hua, R. Huang, and X. Feng, "Offshore vibro-flotation with stone column by jack-up under extreme wave condition," in *Proceedings of the The Fourteenth ISOPE Pacific/Asia Offshore Mechanics Symposium*, Dalian, China, 2020.

[22] J. H. Pogu, C. C. Okafor, and J. C. Ezeokonkwo, "Suitability of sands from different locations at Nsukka as backfill material for vibroflotation," *Nigerian Journal of Technology*, vol. 37, no. 4, pp. 867–874, 2018.

[23] Z. Zhu, Y. Wu, and Z. Liang, "Mining-induced stress and ground pressure behavior characteristics in mining a thick coal seam with hard roofs," *Frontiers of Earth Science*, vol. 10, Article ID 843191, 2022.

[24] J. Qian and P. Wang, "Treatment plan and cost index of soft-soil foundation," *Building Technique Development*, vol. 48, no. 14, pp. 109-110, 2021.

Research Article

Stress-Strain Relationships and Failure Load Analysis of Cement-Stabilized Rammed Earth under Concentric and Eccentric Loading Using Finite Element Modelling

B. M. Sreedhara [1], **M. Rahul Raj,** [1] **Geetha Kuntoji,** [2] **Sujay Raghavendra Naganna** [1] **and Zaher Mundher Yaseen** [3,4]

[1] *Department of Civil Engineering, Siddaganga Institute of Technology, B. H. Road, Tumakuru 572 103, Karnataka, India*
[2] *Department of Civil Engineering, B. M. S. College of Engineering, Bengaluru 560 019, Karnataka, India*
[3] *Department of Earth Sciences and Environment, Faculty of Science and Technology, Universiti Kebangsaan Malaysia, Bangi 43600, Selangor, Malaysia*
[4] *New Era and Development in Civil Engineering Research Group, Scientific Research Center, Al-Ayen University, Nasiriyah, Thi-Qar 64001, Iraq*

Correspondence should be addressed to Zaher Mundher Yaseen; yaseen@alayen.edu.iq

Among many alternative building materials, soil in the form of rammed Earth is the most ancient construction material and technology. Large-scale application of the rammed Earth technology in the construction industry requires the assessment of its strength and failure behaviour. Therefore, this study focused on performing a nonlinear stability analysis of cement-stabilized rammed Earth (CSRE) specimens having a height-to-thickness (H/T) ratios—3 and 4 and loaded under varying degrees of eccentricities 0, 1/3, 1/6, and 1/12. The maximum compressive strength and the stress-strain behaviour of the CSRE specimens were determined through finite element (FE) modeling. The experimental results of the cement-stabilized rammed Earth (CSRE) have been obtained from literature for validation by FE simulation. As the H/T ratio was increased from 3 to 4, the load-bearing capacity of the CSRE specimens increased by 2.91% under concentric loading condition; however, when the eccentricity of load application was swapped from 0 to 1/12, 1/6, and 1/3, the load-bearing capacity decreased incrementally. The results of the FE analysis of the specimens showed that the compressive strength and elastic properties of the CSRE specimens did not differ significantly. The stress-strain relationships were nonlinear and elastic properties were affected by soil textural composition and density.

1. Introduction

Various materials are used in the construction industry from simple to complex constructions [1]. Some are naturally available materials such as wood/timber and soil, and some are man-made like cement, steel, and bricks. The production of the conventional construction materials such as cement and steel involves the consumption of a huge amount of raw materials and energy along with the release of millions of tons of waste/by-products, noise, dust, and toxic gaseous emissions such as sulphur dioxides, and oxides of nitrogen

and carbon. The CO_2, a greenhouse gas, one of the major culprits in environmental deterioration, is produced in the highest amount during the manufacturing process of cement. Along with this, the transportation of these building materials to the site will also witness the emission of CO_2 from the automobiles. Hence, there is an urgent requirement to innovate or bring changes in the building materials that meets the sustainability and structural stability criteria for the greater good of the environment and the society [2]. Among many alternative sustainable building materials available, a historical rammed Earth construction

technology that uses natural subgrade soil as a raw material has recently started gaining popularity [3]. Rammed Earth has been perceived as a fast, simple construction method for the construction of defensive walls in an economical way; build dwellings; and a sustainable way of construction that uses only whatever is accessible on site [4]. This technology basically involves the placing of soil between the formwork boards in layers and compacting it to the required density, to build a homogeneous wall mass. Modern era engineers typically consider rammed Earth technology as a response to the question of making residences for people with restricted financial capital [5].

Usually, the soil to be used in rammed Earth construction should have more clay content since it provides the cohesion between the material particles, which is required for ensuring the stability of the constructed structure. The topsoil is usually not used in the rammed Earth construction process, as it contains biodegradable organic material and absorbs water easily, and also at times, it can be compressed to a large extent, which is not preferred for rammed Earth construction [6]. There are two categories of mixtures in rammed Earth material such as unstabilized and stabilized. The stabilized rammed Earth consists of a mixture of soil, aggregates, and additives, which can be inorganic or organic (cement or lime) that act as a stabilizer to improve the overall strength and performance of the rammed Earth [7], whereas unstabilized rammed Earth does not use any additives and consists of only Earth; that is, the only binder is clay of the soil. The minimum permissible compressive strength values for unstabilized rammed Earth vary from 0.25 MPa to 0.6 MPa, while values for stabilized rammed Earth range between 1 MPa and 15 MPa, although this obviously depends on the amount of stabilizer added [8]. There is a substantial increase of using the rammed Earth construction method in developed countries such as United Kingdom, Australia, the United States of America, and New Zealand owing to global sustainable construction agenda. These countries have developed guidelines, codes, standards, or reference documents for the rammed Earth construction [9–13]. Unfortunately, in India, due to the lack of material testing and case studies on rammed Earth, there are no separate guidelines, standards, or national reference codes being formulated for earthen buildings, and therefore, masonry codes and guidelines are still being followed.

Extensive research is available on rammed Earth technology by various researchers considering both stabilized and unstabilized mixes. The geotechnical properties of the soil play a very important role in rammed Earth construction, and these properties will suggest the suitability of soil. Burroughs [14] considered linear shrinkage and plasticity index as the key indicators for determining the suitability of soil. The range of permissible percentage of shrinkage varies from 0.05% to 3%. Despite decades of research, some countries still design the structural rammed Earth structural elements using suitable Earth, considering the masonry design rules [15]. The structural components like wallets and prisms are usually used to study the compressive strength of rammed Earth of different height-to-thickness ratios. Data from several studies suggest that the

strength reduces by about 30 percent on increasing the height-to-thickness ratio from 5 to 20 [16, 17]. Rammed Earth supports for the construction of ideal sustainable housing units satisfying both eco-friendly and structural stability parameters [18, 19]. Based on the knowledge of weathering processes that dominate in any given area, rammed Earth construction can be undertaken using locally available soil designed to obtain suitable strength and durability characteristics using stabilizers [3, 20–22]. Bui et al. [23] in practice found that the tensile and shear strengths of rammed Earth to be around 10 percent of the strength under compression. A comprehensive review by Ávila et al. [24] provides extensive information on the characterization of unstabilized rammed Earth constructions, considering all mechanical, thermal, and acoustic properties. Finite element modeling has been recognized by a number of researchers as a viable method for investigating the mechanical behaviour of rammed Earth units. Chazallon and Chazallon [25] present elastoplastic modeling of a rammed Earth wall based on finite element simulation to study the hydro-mechanical behaviour of rammed Earth construction under static loading. Similarly, for out-of-plane loading conditions, Shrestha et al. [26] simulated finite element models to predict the response of the rammed Earth building components. Also recently, Strazzeri et al. [27] incorporated micromechanics approach to build a multiscaling model that predicts the macroscopic linear elastic behaviour of cement-stabilized rammed Earth (CSRE) taking into account of material heterogeneities. Over time, an extensive literature on laboratory tests conducted by changing soil properties to study the strength and stability of rammed Earth elements (such as prism, wallets, and full-scale wall for different slenderness ratios under both concentric and eccentric loading conditions) reveals a number of gaps and shortcomings. To check the suitability of soil for rammed Earth construction, different soil properties, and strength and stability of different rammed Earth elements such as prism, wallets, and full-scale wall can be studied using finite element modeling. There is very limited research on the analytical studies of rammed Earth using a finite element analysis to understand its nonlinear behaviour through finite element modeling [25, 28]. Hence, in this study, the objective was to analytically determine the compressive strength and stress-strain behaviour of cement-stabilized rammed Earth (CSRE) elements with different H/T ratios (3 and 4) under different load eccentricities (0, 1/3, 1/6, and 1/12) as per Indian Masonry code IS 1905–1987 [29].

2. Methodology

2.1. Experimental Data. The data of cement-stabilized soil required for the finite element analysis of rammed Earth specimens were collected from literature titled "Strength and durability of rammed Earth for walling" [22]. The suitability of soil properties and their range for rammed Earth construction were taken from the literature titled "Behaviour of cement-stabilized rammed Earth walls under concentric and eccentric gravity loading" [17].

The locally available soil was used in the experimental works of literature [22], and their properties are tabulated in Table 1. The soil property data conformed to be within the

TABLE 1: Properties of soil used for modeling.

Textural composition	
Sand (0.075–4.75) mm	61%
Silt (0.002–0.075) mm	17%
Clay (<0.002) mm	22%
Atterberg's limits	
Liquid limit	29
Plastic limit	22
Shrinkage limit	20
Plasticity index	7
Shrinkage index	9
Maximum dry density (kg/m^3)	2020

Adopted from Suresh and Anand [22].

range of basic soil properties necessary for rammed Earth structures as per literature [17]. Finite element modeling was carried out, and the obtained results were compared and validated with the previous research [22] for concentric loading conditions. The study was further extended by considering cement-stabilized rammed Earth specimens for different H/T ratios (3 and 4) and under different eccentricities (0, 1/3, 1/6, and 1/12) to determine the compressive strength and stress-strain behaviour.

2.2. Finite Element Modeling.
A method that was used primarily to solve the partial differential equations numerically is termed as the finite element method or finite element analysis [30]. In simple terms, a physical phenomenon is discretized into smaller or simpler elements, which are then solved to obtain the overall solution by combining the solutions of smaller elements. These discretized elements are referred to as finite elements. The finite elements are connected to each other by nodes. This whole system of finite elements and the nodes is called as a mesh. The mesh is simply a system of mathematical equations, whose unknowns are the values of dependent variables in nodes. The equations are solved using the nodal values of dependent variables. The value of the whole element is found using shape functions. Thus, a piecewise approximation of spatial variation in dependent variables is obtained [31]. The Newton–Raphson method was used to solve the system of nonlinear equations and for the refinement of the finite element mesh. In this study, a macromodeling approach was considered in the ANSYS software platform for implementing finite element analysis.

2.3. Modeling Considerations and Calibration.
The prism specimen of dimension 150 mm × 300 mm × 450 mm of (H/T = 3) was modeled, in three layers with a lift of 150 mm similar to the construction technique where the soil is rammed or compacted in layers of 150 mm. The mild steel plate is considered on top of the specimen for the application of load in order to avoid direct application of load on the specimen, which may cause local failure of the specimen. The thickness of the mild steel plate considered was 20 mm. The geometry modeled should be assigned with the material properties in order to carry out the analysis. The material properties considered for the study are as follows:

(1) Soil + 7% cement

(2) Structural steel (plate)

For the materials defined, various properties have to be assigned as inputs such as density, young's modulus, Poisson's ratio, and specimen dimensions in order to perform the nonlinear analysis in ANSYS workbench [32]. The input of stress and strain values of the material is mandatory for performing nonlinear analysis. The required stress and strain values of the material were taken from the experimental investigation [22]. The contact region between the layers of the elements should be connected by some sort of connections like rigid or frictional surface. The connections between the layers are usually automatically generated by the ANSYS workbench, but it is always preferred to create the connections again according to our requirements. In this study, the rammed Earth prism specimen was modeled as a set of stacked layers (of 150 mm) of finite elements to simulate the interfaces between compaction layers. The interface between the layers has to be connected to one another. This can be done using the connection options in ANSYS. In this case, frictional contact was used between the topmost soil layer and mild steel plate; and bonded contact was used between the stacked soil layers. A global coordinate system was considered in this study.

ANSYS being an FEM analysis tool, the specimen or model will be divided into finite elements, and each element will be analysed from the given inputs. Here, the model is divided into finite elements by meshing. Any mesh size can be assigned, but considering the system features and the capacity to simulate, the corresponding mesh size should be given as input, because as we decrease the mesh size, the number of elements increases and as the number of elements increases, the software has to analyse each element; hence, the simulation/analysis time would increase. The mesh size given as input in our case was 10 mm. The basic idea behind finite element analysis is that the analysis of each step is divided into the specified number of substeps till the result converges to the inbuilt reference of ANSYS workbench. Therefore, in this study, the maximum number of substeps assigned was 15. The support conditions for the FE model were assigned as "FIXED" at the base of the prism specimen. A concentric uniformly distributed compressive load was applied on the specimen through a mild steel plate. The uniformly distributed compressive load was incrementally increased at the rate of 10 kN till failure in the finite element analysis. However, during analysis after the application of certain incremental load, the loading rate changes to 1 kN in order to obtain the exact failure load of the specimen due to compression. Prior to failure, the CSRE prism elements are considered to be linearly elastic and isotropic. Final failure of CSRE prism elements is indicated by the lack of symmetry in the displacements or by the convergence of the displacements. The results obtained from the modeling for concentric loading were validated with the experimental results of the literature [22].

Furthermore, this study was extended to analyse the behaviour of prism specimens (150 mm × 300 mm × 600 mm) with H/T = 4 at different ratios of eccentricity (E/T) as given below:

(i) Specimen—1 (150 mm × 300 mm x 450 mm): H/T = 3 and E/T = 0 (concentric load)

(ii) Specimen—2: H/T = 3 and Load at E/T = 1/3 (50 mm from the axis along the thickness)

(iii) Specimen—3: H/T = 3 and load at E/T = 1/6 (25 mm from the axis along the thickness)

(iv) Specimen—4: H/T = 3 and load at E/T = 1/12 (12.5 mm from the axis along the thickness)

(v) Specimen—5 (150 mm × 300 mm × 600 mm): H/T = 4 and E/T = 0 (concentric load)

(vi) Specimen—6: H/T = 4 and Load at E/T = 1/3 (50 mm from the axis along the thickness)

(vii) Specimen—7: H/T = 4 and load at E/T = 1/6 (25 mm from the axis along the thickness)

(viii) Specimen—8: H/T = 4 and load at E/T = 1/12 (12.5 mm from the axis along the thickness)

3. Simulation Results and Discussion

3.1. Analysis of CSRE Prism Specimen under Concentric Loading. The CSRE prism specimen with H/T = 3 was considered to study the deformation, failure load, and stress-strain behaviour under concentric loading, and the model results were validated with the experimental results. Figure 1 shows the FE model of CSRE specimens. The incremental load of 10 kN was applied to study the deformation of prism specimen, and the maximum load taken by the specimen was found to be 103 kN with 5.38-mm deformation. The CSRE prism loaded at the centroid of the cross section demonstrated increased load-bearing capacity (failure load) as the H/T ratio was increased from 3 to 4, owing to homogeneous longitudinal stress distribution along the height of the prism and the absence of local buckling (which occurs only when the height-to-thickness ratio is greater than 10). Table 2 shows the comparison of the FE model results and the experimental results. A root mean square error of 1.95 mm was obtained between the model and experimental results. Stress and strain values observed at the centre of the specimen were noted for different loading intensities until failure and a stress v/s strain curve was plotted for the same as shown in Figure 2. CSRE specimen failure results from a unique and critical combination of biaxial stresses. Under concentric loading conditions, the load-carrying capacity of CSRE prisms was relatively higher, and the tendency for out-of-plane deformation was lower. It could be observed from the stress-strain curve that the FEM model is following the same trend and has good correlation with the experimental results. The FE model results validated against the experimental results encouraged for further study of CSRE specimens with varying H/T ratios under different eccentric loading conditions.
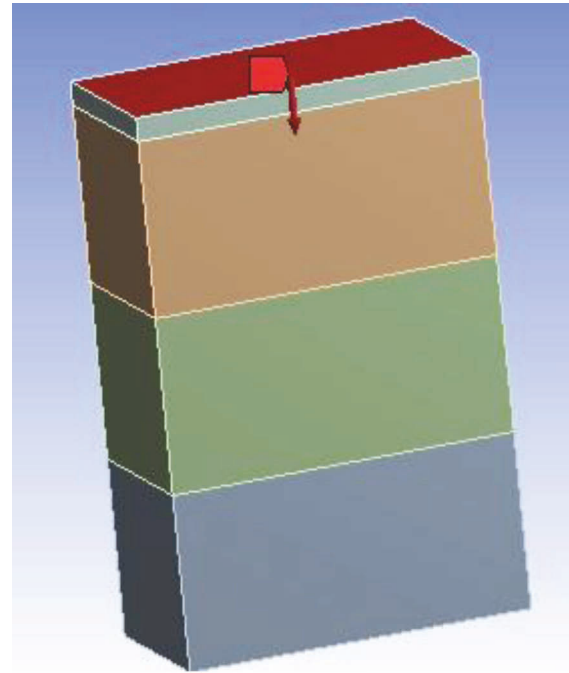

Figure 1: FEM model of CSRE prism (H/T = 3) under concentric loading.

3.2. Analysis of CSRE Prism Specimen under Eccentric Loading with H/T = 3. The CSRE prism (specimen size—150 × 300 × 450 mm) with H/T = 3 was considered for the FE modeling and analysed under different eccentric loading conditions to obtain the maximum compressive strength as well as stress and strain values at the centre of the specimen. The FE models of the specimen with H/T = 3 under different load eccentricities are shown in Figure 3. Figure 4 shows the deformation curve of the CSRE specimen with H/T = 3 under 4 different eccentricities, that is, 0, 1/3, 1/6, and 1/12. It was found that the maximum compressive load of the specimen decreases as the eccentricity of load application increases. On average, the compressive strength decreases by 32% as the eccentricity increases from 0 to 1/6, while it decreases to 42.8% when eccentricity is changed from 1/6 to 1/3. The deformation contours presented in Figure 5 indicate that the deformation was maximum at the top and minimum at the bottom. A faster loss of stability could be seen when the load eccentricity increases leading to a reduced compressive strength of prism specimens.

The maximum stress and strain values of each specimen at the centre are tabulated in Table 3. The stress values of the specimen remain the same for eccentricities 0 and 1/12, and on average, it decreases by 31.08% as the eccentricity is increased from 1/6 to 1/3. The strain of the specimen decreases by 43.47% on average as eccentricity is increased from 1/12 to 1/3, whereas the strain value for eccentricity 0 is 3 times lesser than that of eccentricity—1/12. The stress values add up in the specimen under eccentric loading due to the moment created by the load, which can be found manually using the bending equation. The strain within the specimen increases with an increase in the eccentricity as

TABLE 2: Load-deformation values of CSRE prism (H/T = 3; E/T = 0).

| Load (kN) | Deformation (mm) | | % error $= (M_i - E_i)/E_i \times 100$ | Root mean square error (mm) $= \sqrt{\sum_{i=1}^{N} (M_i - E_i)^2/N}$ |
	Finite element model (M_i)	Experimental (E_i)		
0	0	0	0	
10	0.506	0.6	15.67	
20	1.04	1	3.85	
30	1.56	1.47	5.77	
40	2.09	1.85	11.49	
50	2.6	2.35	9.62	1.95
60	3.15	2.65	15.88	
70	3.7	2.9	21.63	
80	4.29	3.3	23.08	
90	4.91	3.5	28.72	
100	5.22	4	23.38	
103	5.38	4.35	19.15	
104	Failure load		Mean = 14.85	
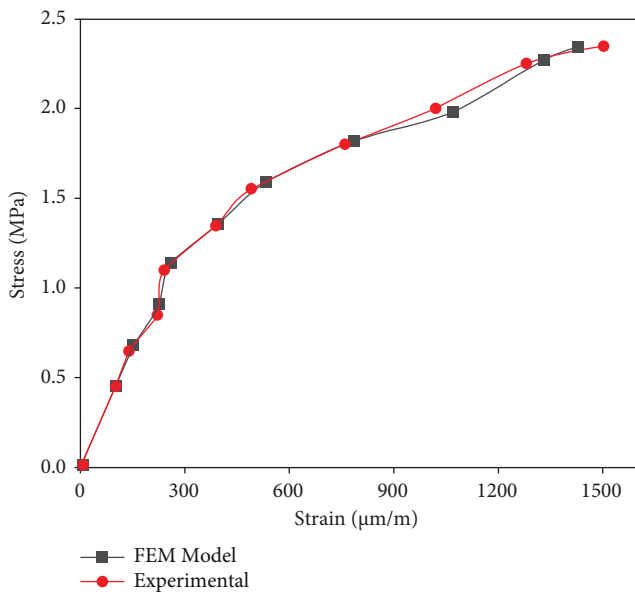
FIGURE 2: Stress-strain curve at the centre of CSRE prism with H/T = 3 under concentric loading.

FIGURE 3: CSRE specimens with H/T = 3 models at different eccentricities.

shown in Figure 4. This demonstrates how the eccentric load affects the rigidity of the CSRE prism, leading the specimen to lose stability more quickly. Furthermore, when the eccentricity of the load increases, the load-bearing capacity of the prism specimen decreases monotonically.

3.3. Analysis of CSRE Prism Specimen under Eccentric Loading with H/T = 4. The CSRE prism (specimen size—150 × 300 × 600 mm) of H/T = 4 with different eccentricities were modeled and analysed in a similar fashion as that of the CSRE specimen of H/T = 3, to obtain the maximum compressive strength and stress v/s strain behaviour at the centre. Different material properties can be defined in the FE model to simulate the changes in the behaviour of the entire unit considered. In the model with H/T = 4, another layer of cement-stabilized soil was placed on t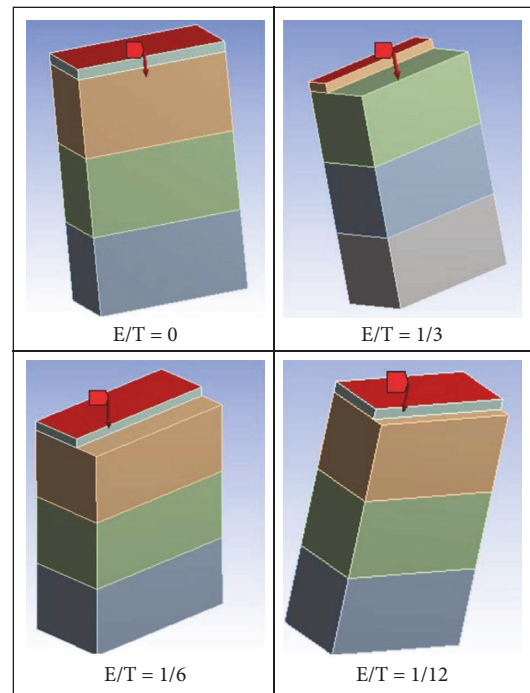he previous layer with a lift of 150 mm to obtain an overall specimen height of 600 mm. The connection between the layers of soil was bonded in nature. The models of the specimen with H/T = 4 with different eccentricities are shown in Figure 6. Figure 7 shows the deformation curves of the specimens with H/T = 4 under four different eccentricities, that is, 0, 1/3, 1/6, and 1/12. The maximum compressive strength of the specimen on an average decreases by 33.96% when the eccentricity is increased from 0 to 1/6, while it decreases by 42.8% when the eccentricity is further increased from 1/6 to 1/3. The CSRE prism loaded at the centroid of the cross section demonstrated increased load-bearing capacity (failure load) as the H/T ratio was increased from 3 to 4, owing to homogeneous longitudinal stress distribution along the height of the prism and the absence of
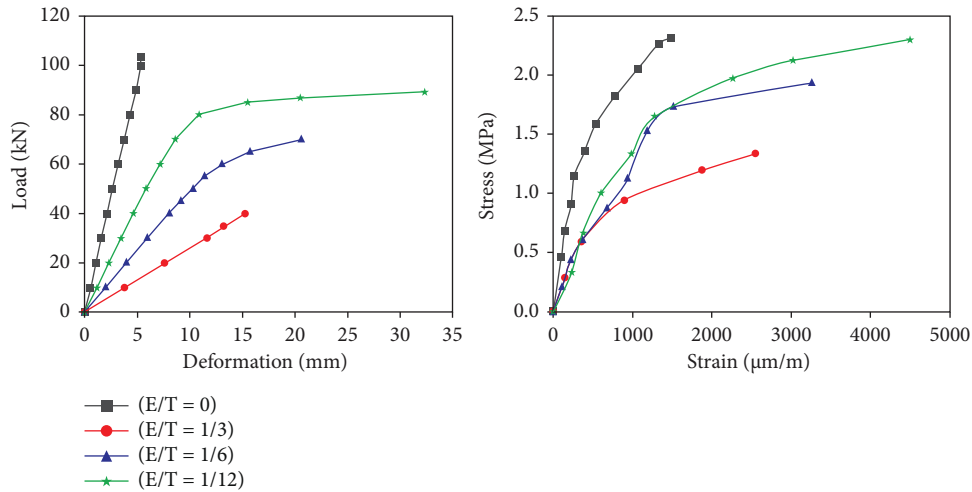
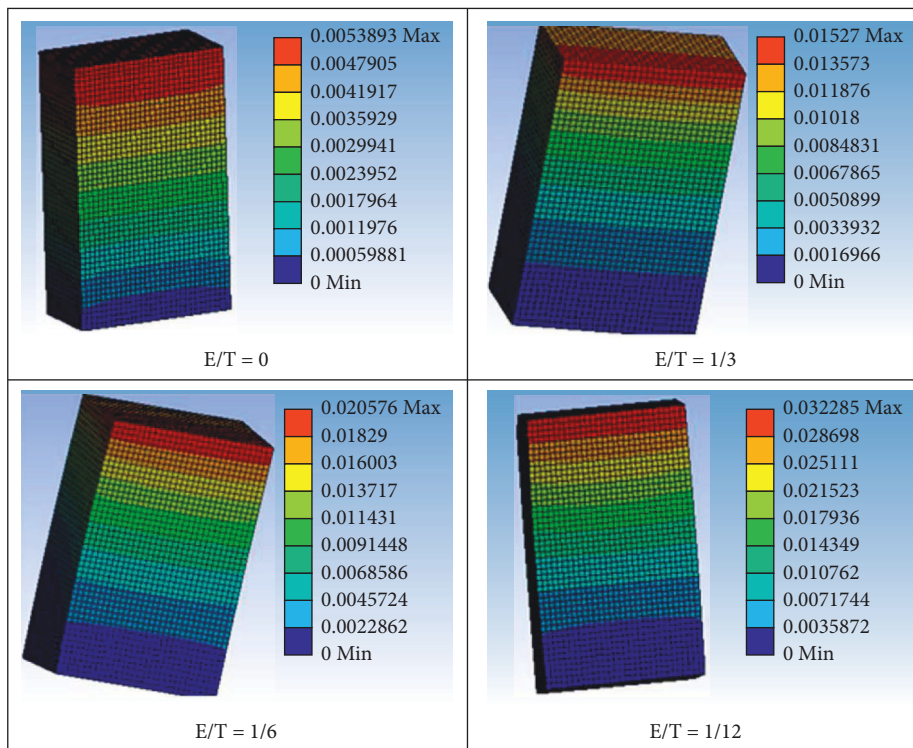Figure 4: Load-deformation curve and stress-strain curves at the centre for CSRE specimens with H/T = 3.

Figure 5: Deformation contours of specimens with H/T = 3.

Table 3: Result summary of the finite element model of CSRE specimens.

Eccentricity ratio	E/T = 0		E/T = 1/3		E/T = 1/6		E/T = 1/12	
CSRE prism specimens	H/T = 3	H/T = 4	H/T = 3	H/T = 4	H/T = 3	H/T = 4	H/T = 3	H/T = 4
Failure load (kN)	103	106	40	40	70	70	89	88
Maximum deformation (mm)	5.38	7.77	15.27	25.62	20.57	37.90	32.30	47.90
Maximum stress (MPa)	2.31	2.33	1.33	1.29	1.93	1.72	2.30	2.29
Maximum strain (μm/m)	1428	1460	2538	2705	3258	3210	4490	4405

local buckling (which occurs only when the height-to-thickness ratio is greater than 10). The deformation contours shown in Figure 8 indicate that the deformation was maximum at the top and minimum at the bottom. The stress v/s strain curves drawn for the CSRE specimen with H/T = 4 under different eccentric loading conditions are presented in
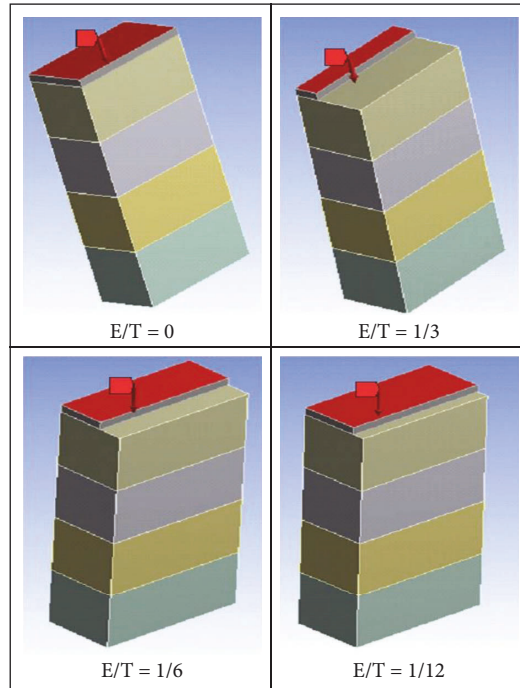
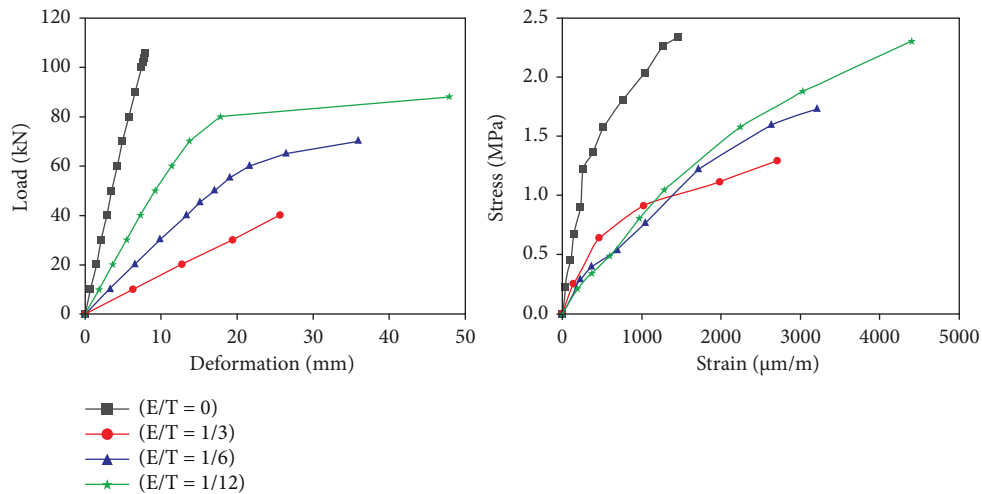FIGURE 6: CSRE specimens with H/T = 4 models at different eccentricities.

FIGURE 7: Load-deformation curve and stress-strain curves at the centre for CSRE specimens with H/T = 4.

Figure 7. The stress value of the specimen almost remains the same for the eccentricities 0 and 1/12, whereas on average, it decreases by about 25% when the eccentricity is increased from 1/6 to 1/3. The strain within the specimen decreases by 43.66% on average as eccentricity is increased from 1/12 to 1/3, whereas the strain value for eccentricity 0 is about 3 times lesser than that of eccentricity—1/12 as shown in Table 3.

The eccentric loading over CSRE prism specimens poses an uncertain situation, since the strain distribution over the section and randomness of fracture propagation within the prism is often complex.

The finite element modeling was capable of effectively predicting the stress-strain behaviour of CSRE prism specimens of different height-to-thickness ratios (3 and 4)
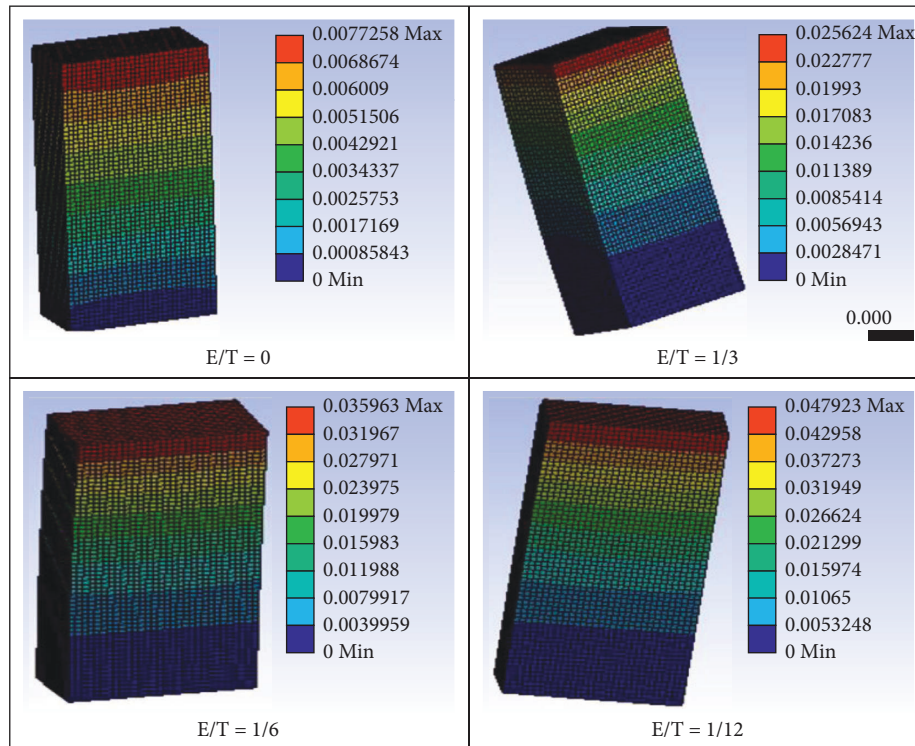
FIGURE 8: Deformation contours of specimens with H/T = 4.

along with their collapse/failure loads. The finite element model estimates of failure loads and the deformation values aid in the prediction of sufficiently accurate failure mechanisms.

4. Conclusions

The finite element analysis of cement-stabilized rammed Earth prisms of different height-to-thickness ratios (3 and 4) subjected to compressive load at different eccentricities 0, 1/3, 1/6, and 1/12 arrived at the following conclusions:

(1) The finite element model of CSRE prism having H/T ratio = 3 was subjected to varying magnitudes of concentric compressive load, and the deformation values obtained had a root mean square error of 1.95 mm in validation with the experimental results.

(2) Maximum compressive load—As the eccentricity of load application was increased from 0 to 1/6, the maximum compressive load decreased by 32% for the prism with H/T ratio = 3, whereas it decreases by 33.96% for the prism with H/T ratio = 4. When the eccentricity was increased from 1/6 to 1/3, the maximum compressive strength decreased by 42.8% in the prisms with H/T ratios = 3 and 4.

(3) Stress—The stress value was determined at the centre of the prism. For prisms with H/T ratios = 3 and 4, the stress value of the specimens remained almost the same for eccentricities 0 and 1/12. But, when the eccentricity of loading was increased from 1/6 to 1/3, the stress decreases by 31.09% for the prism with H/T

ratio = 3, whereas it decreases by 25% for the prism with H/T ratio = 4.

(4) Strain—The strain value was determined at the centre of the prism. As the eccentricity was increased from 1/12 to 1/3, the strain decreases by 43.47% for the prism with H/T ratio = 3, whereas it decreases by 38.59% for the prism with H/T ratio = 4. But, the strain value for zero eccentricity was 3 times lesser than that of eccentricity of 1/12 for both the prisms with H/T ratios = 3 and 4.

The current research focuses solely on the behaviour of compressed cement-stabilized rammed Earth prism specimens. The limitation is that we are unable to generalize the results to a full-scale wall unit (commonly built rammed Earth construction). Future research should concentrate on performing a finite element analysis of any full-scale rammed Earth wall under compressive load and validate the results with experimental data.

Data Availability

The datasets generated during and/or analysed during this study are available from the authors on reasonable request.

Consent

Not Applicable.

Disclosure

ANSYS software was employed for FEM simulation.

Conflicts of Interest

The authors confirm that there are no conflicts of interest associated with this publication.

References

[1] D. Thompson, C. Osorio, and J. P. Osorio, "A review of current construction guidelines to inform the design of rammed earth houses in seismically active zones," *Journal of Building Engineering*, vol. 54, Article ID 104666, 2022.

[2] B. M. Ramesh, R. M. Vongole, Y. Naganna et al., "Valorization of incinerator bottom ash for the production of resource-efficient eco-friendly concrete: performance and toxicological characterization," *Architecture, Structures and Construction*, vol. 1, no. 1, pp. 65–78, 2021.

[3] G. Chang, C. M. Fiori, and C. Schexnayder, "Rammed earth: construction lessons from experience," *Practice Periodical on Structural Design and Construction*, vol. 18, no. 3, pp. 149–154, 2013.

[4] D. Easton and T. Easton, "Modern rammed earth construction techniques," in *Modern Earth Buildings, Woodhead Publishing Series in Energy*, M. R. Hall, R. Lindsay, and M. Krayenhoff, Eds., Woodhead Publishing, Cambridge, UK, pp. 364–384, 2012.

[5] H. Nouri and S. M. Hosseini, "Life cycle assessment of earthen materials for low-cost housing a comparison between rammed earth and fired clay bricks," *International Journal of Building Pathology and Adaptation*, 2021, ahead-of-print.

[6] R. A. Silva, D. V. Oliveira, T. Cristelo, N. Escobar, M. C. Soares, and E. Soares, "Rammed earth construction with granitic residual soils: the case study of northern Portugal," *Construction and Building Materials*, vol. 47, pp. 181–191, 2013.

[7] D. Tripura and K. Singh, "Structural behavior of rectangular cement-stabilized rammed earth column under compression," *Advances in Structural Engineering*, Springer India, New Delhi, India, pp. 2459–2469, 2015.

[8] P. A. Jaquin, *Analysis of Historic Rammed Earth Construction*, Durham University, UK, 2008, http://etheses.dur.ac.uk/2169/.

[9] Hb 195, *The Australian Earth Building Handbook*, Standards Australia International Ltd, Sydney, Australia, 2002.

[10] Nzs 4297, *Engineering Design of Earth Buildings"*, Standard, Newzeland, New zeland, 2020.

[11] Nzs 4298, *Materials and Construction for Earth Buildings*, Standard, Newzeland, New zeland, 2020.

[12] Nzs 4299, *Earth Buildings Not Requiring Specific Engineering Design*, Standard, Newzeland, New zeland, 2020.

[13] Astm E2392 05, *Standard Guide for Design of Earthen wall Building Systems*, Astm standard, PA, USA, 2005.

[14] S. Burroughs, "Soil property criteria for rammed earth stabilization," *Journal of Materials in Civil Engineering*, vol. 20, no. 3, pp. 264–273, 2008.

[15] V. Walker and P. Walker, "Structural capacity of rammed earth in compression," *Journal of Materials in Civil Engineering*, vol. 20, no. 3, pp. 230–238, 2008.

[16] M. E. Arslan, M. Yalama, and A. Yalama, "Structural behavior of rammed earth walls under lateral cyclic loading: a comparative experimental study," *Construction and Building Materials*, vol. 133, pp. 433–442, 2017.

[17] B. V. Venkatarama Reddy, V. Nanjunda Rao, and K. S. Nanjunda Rao, "Behaviour of cement stabilised rammed earth walls under concentric and eccentric gravity loading," *Earthen Dwellings and Structures: Current Status in Their Adoption*, Springer, Singapore, pp. 293–303, 2019.

[18] C. Ciancio and D. Ciancio, "Durability of cement-stabilised rammed earth: a case study in Western Australia," *Australian Journal of Civil Engineering*, vol. 14, no. 1, pp. 54–62, 2016.

[19] B. Khadka, "Rammed earth, as a sustainable and structurally safe green building: a housing solution in the era of global warming and climate change," *Asian Journal of Civil Engineering*, vol. 21, no. 1, pp. 119–136, 2020.

[20] M. Hallal, S. Sadek, and S. S. Najjar, "Evaluation of engineering characteristics of stabilized rammed-earth material sourced from natural fines-rich soil," *Journal of Materials in Civil Engineering*, vol. 30, no. 11, Article ID 04018273, 2018.

[21] S. M. S. Hussaini and V. Toufigh, "Strength and fracture behavior of rammed-earth materials," *Journal of Materials in Civil Engineering*, vol. 31, no. 10, Article ID 04019228, 2019.

[22] A. Suresh and K. B. Anand, "Strength and durability of rammed earth for walling," *Journal of Architectural Engineering*, vol. 23, no. 4, Article ID 06017004, 2017.

[23] T. T. Bui, A. Limam, and S. Maximilien, "Failure of rammed earth walls: from observations to quantifications," *Construction and Building Materials*, vol. 51, pp. 295–302, 2014.

[24] F. Ávila, E. Gallego, and R. Gallego, "Characterization of the mechanical and physical properties of unstabilized rammed earth: a review," *Construction and Building Materials*, vol. 270, Article ID 121435, 2021.

[25] H. Chazallon and C. Chazallon, "Finite element modelling of a rammed earth wall," *Construction and Building Materials*, vol. 25, no. 4, pp. 2112–2121, 2011.

[26] K. C. Shrestha, M. Aoki, and T. Aoki, "Assessment of out-of-plane behavior of rammed earth walls by pull-down tests," *International Journal of Architectural Heritage*, vol. 13, no. 2, pp. 273–287, 2019.

[27] V. Strazzeri, A. Elchalakani, and M. Elchalakani, "Micromechanics modelling of cement stabilised rammed earth," *Mechanics of Materials*, vol. 148, Article ID 103540, 2020.

[28] L. Miccoli, D. V. Oliveira, R. A. Silva, U. Schueremans, and L. Schueremans, "Static behaviour of rammed earth: experimental testing and finite element modelling," *Materials and Structures*, vol. 48, no. 10, pp. 3443–3456, 2015.

[29] Is 1905-1987, *Indian Standard Code of Practice for Structural Use of Unreinforced Masonry*, Indian Standard, Old Delhi, India, 2002.

[30] J. Narasimha Reddy, *Introduction to the Finite Element Method*, McGraw-Hill Education, New Delhi, 4th edition, 2019.

[31] O. C. Zienkiewicz, R. L. Taylor, and J. Zhu, *The Finite Element Method: Its Basis and Fundamentals*, Elsevier, Oxford, UK, 6th edition, 2005.

[32] Ansys Inc, *Ansys fluent user's guide, release 17.2*, 2016, https://www.ansys.com/.